GRAVITY CURRENTS WITH HEAT TRANSFER EFFECTS

Thesis by

Michael V. Chobotov

In Partial Fulfillment of the Requirements

for the Degree of

Doctor of Philosophy

Division of Engineering and Applied Science

California Institute of Technology

Pasadena, California

1987

(Submitted September 10, 1986)

To my Mother, Father,

and Brother

Acknowledgements

Throughout my years at Caltech, I have most enjoyed the opportunity to work with many extremely talented individuals, and I would like to express my thanks to all of them. In particular, I would like to thank my advisor, Professor Zukoski, for his guidance, enthusiasm, and support, which were essential in the completion of this work. In addition, I would like to acknowledge the countless valuable contributions made by Professor Kubota during the course of this work. Many fruitful discussions with Professors Brennen, Sabersky, and Marble also contributed to this effort, and I take this opportunity to thank them as well. I am also indebted to fellow graduate students Joe Humphrey, Tom Sobota, Howard Stone, Steve Toner, and Tom Zsak for their contributions of support and expertise. Personal support that allowed me to accomplish my ambition was provided by my family, Gail Smith, Heather and Joe Humphrey, Tom Zsak, and all of my other close friends of whom, fortunately, there are too many to thank individually here. To Professors Brennen and Sabersky I also extend a special thanks for the encouragement and guidance they gave me, especially during my undergraduate years. Finally, I would like to acknowledge the National Bureau of Standards for its financial support of this research.

Abstract

A two part experimental study of gravity currents flowing in horizontal channels is performed. The first of these examines adiabatic aqueous flows, and the second, heat transferring gaseous currents. Video photography of dyed saline current fronts flowing into a fresh-water-filled duct allows for front velocity measurements and the study of qualitative flow features such as current head structure, mixing, and layer thickness. In conjunction with previous works, a model of gravity current entrainment is presented. The effects of viscosity are examined in the transition from constant velocity flow to a decelerating, viscous dominated flow regime. This transition is shown to occur at a streamwise position that is a function only of the current layer thickness, and not of Reynolds number, as previously believed.

To examine the effects which the reduction of buoyant forces due to heat loss has on gravity current flow, heated gaseous flows in another experimental facility are studied. A smoke flow-visualization technique is developed, and together with fine gauge thermocouples, heat flux gauges, and shadowgraphy, provides for flow measurement. Front velocities, layer thicknesses, wall heat fluxes, layer velocity and temperature profiles, and qualitative flow characteristics are recorded. The thermal front, with its constant channel-ceiling-temperature boundary condition, is found to decelerate as it moves downstream, while the layer thickness is seen to increase. Layer Richardson number is found to be constant along the streamwise direction of the flow, and an empirical relation for Nusselt number versus Reynolds number is obtained. Free convection in the form of longitudinal roll cells is shown to promote the high levels of heat transfer measured. A flow modeling scheme based on experimental observations is also developed.

Table of Contents

List of Figures

Nomenclature

Symbol	Description
a	Model velocity and temperature profile scale factor.
B	Buoyancy flux; $g\,\Delta\,Q$.
b	Model current layer breadth.
C	Gravity current spreading rate constant; $V/(g\Delta Q)^{1/3}$.
C_1	Gravity current spreading rate constant; $V/(g\Delta h)^{1/2}$.
C_i	Model integral constants; i= 1 to 4.
C_5	Displacement thickness constant; $\delta_1/\sqrt{\frac{\nu x}{U_m}}$.
C_f	Skin friction coefficient; $\tau_w/\frac{1}{2}\rho u_m^2$.
C_H	Dimensionless heat transfer coefficient; Nu_x/Re_xPr.
C_p	Specific heat at constant pressure.
$\mathcal{D}$	Expression in denominator of velocity gradient equation.
$\mathcal{D}_o$	$\mathcal{D}$ evaluated for $C_f = 0$, $C_5 = 0$.
d	Channel height.
Fr	Froude number; $V/\sqrt{g\Delta h}$.
g	Gravitational acceleration.
h	Heat transfer coefficient; $q/\Delta T$.
h	Gravity current layer thickness.
h_{head}	Gravity current head thickness.
h_{nose}	Gravity current nose height.
$\hat{j}$	Unit vector in y direction.
k	Thermal conductivity.
$\dot{m}$	Gravity current mass flux.
$\mathcal{N}$	Expression in numerator of velocity gradient equation.
$\mathcal{N}_o$	$\mathcal{N}$ evaluated for $C_f = 0, C_5 = 0$.

Nu_x	Nusselt number; hx/k.
p	Pressure.
Pr	Prandtl number; ν/α.
Q	Volumetric flow per unit span of current source fluid.
Q_i	Flows relative to gravity current head; $i = 1$ to 5.
q	Heat flow per unit area.
$R(t)$	Gravity current front position as a function of time.
R_1	Characteristic length scale; $Q^2/(g\Delta Q)^{1/3}\nu$.
Ra	Rayleigh number; $\beta g d^3 \Delta T/\alpha\nu$.
Re	Reynolds number based on head thickness; Vh_{head}/ν.
Re_x	Reynolds number based on streamwise distance; Vx/ν.
Ri	Richardson number; $(\rho_a - \rho)gh/\rho U^2$.
T	Temperature.
T_f	Film temperature; $(T_{max} + T_w)/2$.
t	Time.
t_1	Characteristic time scale; $Q^2/(g\Delta Q)^{2/3}\nu$.
U	Local velocity maximum in current layer.
u	Velocity in x direction.
V	Gravity current front velocity.
v	Velocity in y direction.
w	Channel width.
w	Velocity in z direction.
X	Streamwise measurement station.
x	Streamwise coordinate, $x = 0$ at channel inlet.
x_t	Constant velocity flow / declerating flow transition point.
Y	Measurement station y value.

y	Downward coordinate, $y = 0$ at channel ceiling.
y_i	Howarth transformed y coordinate; $\int_0^y \frac{\rho}{\rho_o} dy'$.
Z	Spanwise measurement station.
z	Spanwise coordinate, $z = 0$ at center-span.
α	Thermal diffusivity.
Δ	Density difference ratio; $\Delta\rho/\rho$.
$\Delta( )$	Difference of quantity ( ) relative to initial or ambient value.
δ	Model layer total thickness.
δ_1	Displacement layer thickness.
δ_i	Model layer total thickness in transformed coordinate.
δ_{th}	Thermal boundary layer thickness.
δ_v	Boundary layer thickness.
η	Model dimensionless coordinate; y_i/δ_i .
ϑ	Temperature ratio; $(T_m - T_o)/T_o$.
μ	Current fluid viscosity.
ν	Current fluid kinematic viscosity.
ρ	Density in current layer.
ρ_a	Ambient fluid density.
τ_w	Wall shear stress.

Superscripts

$( )^*$	Non-dimensionalized quantity.
$( )'$	Small perturbation quantity.

Subscripts

$( )_{inf}$	Profile inflection-point quantity.
$( )_m$	Maximum value of quantity.

$( )_o$ Original or ambient quantity.

$( )_w$ Quantity evaluated at wall.

GRAVITY CURRENTS WITH HEAT TRANSFER EFFECTS

Thesis by

Michael V. Chobotov

Chapter 1

Introduction

1.1 General Description of Gravity Currents

Buoyant forces produced from density variations in fluids subjected to a gravitational field give rise to a variety of classes of motions. Examples of these types of flows in which the fluid motions are predominantly in the direction normal to that of the accelerational field are known as gravity currents, or density currents, and have abundant manifestations in our environment.

As meteorological phenomena, gravity currents can be seen in the form of weather fronts, whose passages are marked by changes in temperature, wind, and precipitation, and also in the form of fog banks and fluidized suspensions, such as avalanches and volcanic plumes. Submarine particulate suspensions known as turbidity currents travel along the ocean floor, leaving behind deposits and often breaking cables laid across submarine canyons. Gravity currents in the ocean are also driven by temperature and salinity differences, examples of which include salinity currents and oceanic intrusions at rivermouths.

Not all gravity currents in our surroundings are of strictly natural causes, however. Powerplant cooling water discharge, oil spillage at sea, and the movement of combustion products in burning buildings are all examples of man-made gravity currents of no less consequence than many of the naturally induced flows. The latter example is especially significant in light of the fact building fires take thousands of lives and cause billions of dollars of damage annually in just the United States alone. In such fires the two most significant dangers are the toxicity

and oxygen deficiency of the products of combustion, and these are precisely the hazards that are convected throughout the structure by buoyancy driven flows, including gravity currents.

Gravity currents of this type, in which the convecting current's temperature difference relative to the ambient fluid provides the relative density difference, are greatly influenced by heat exchange with the surroundings, and are the subject of this investigation. More specifically, such currents with geometrically two-dimensional constraints simulating flow boundaries such as hallways and rooms with length scales much greater than width will be considered.

In the next section a review of previous work in the study of gravity currents will be given, which will be followed by a section discussing the goals of this research. Experimental results are presented in Chapters 2 and 3 which pertain to both steady and unsteady characteristics of gravity currents without and with heat transfer to the surroundings, respectively. Although quite different in behavior from gravity currents with heat transfer, adiabatic currents give a good reference point for comparison purposes, allow for effective qualitative study of various flow phenomena, and serve as a general guideline for the scaling and design of heat transferring current experiments.

The development and results of analytical and empirical modeling for two-dimensional gravity currents with heat transfer and including the effects of wall shear are given in Chapter 4. A summary and conclusion appears as Chapter 5.

1.2 Background

When a fluid is discharged at the surface of a denser fluid in a horizontal channel, it forms a gravity current along the surface or ceiling of the duct, as would a denser fluid entering under a lighter ambient fluid. The basic characteristics

of this current (assuming we have a constant volumetric discharge rate and an initially uniform density profile of the current fluid) are a head at the leading edge of the flowing layer, and a quiescent interface between the two fluids behind the head, as depicted in figure 1.1. Early analytical work on the subject of gravity current propagation focused on ideal fluid models. Von Kármán (1940) deduced an expression using the irrotational Bernoulli equation for the propagation speed of a dense gravity current moving under an infinite body of light ambient fluid in terms of the current thickness and the density difference normalized by the ambient fluid's density. In a real fluid, however, viscous effects will change the velocity profile in the current, and have been observed to significantly affect the characteristics of the head and the spreading rate of the current. Furthermore, neither irrotationality nor energy conservation hold in the general case, and when gravity current flows occur in a channel, their characteristics depend on the fractional depth the current occupies of the channel.

Gravity current asymptotic flow regimes can be identified in which viscous forces dominate inertial forces in the gravity current motion or, in the other extreme, are negligible relative to inertial forces and to the buoyant driving forces of the current. For the case in which viscous effects are not important, Chen (1980) used a balance between buoyant and inertial forces for a two-dimensional gravity current, flowing in an ambient fluid reservoir of infinite extent, to determine the frontal position, R, of the current as a function of time:

$$R(t) \sim \left[g \frac{(\rho - \rho_a)}{\rho_a} Q \right]^{1/3} t \qquad (1.2.1)$$

where ρ is the current fluid density, ρ_a the ambient fluid density, Q the volumetric flow rate per unit span of the current medium, and g the acceleration due to gravity. A balance between the buoyant driving force and viscous resisting forces acting on the gravity current layer yielded an expression for downstream position

of the front versus time for the viscous dominated asymptotic case of the form:

$$R(t) \sim \left[\frac{g \frac{(\rho - \rho_a)}{\rho_a} Q^3}{\nu} \right]^{1/5} t^{4/5} \tag{1.2.2}$$

where ν is the kinematic viscosity of the current fluid, and is assumed comparable to the kinematic viscosity of the ambient fluid. From these results follow the characteristic length and time scales of:

$$R_1 = \frac{Q^2}{(g \Delta Q)^{1/3} \nu} \tag{1.2.3}$$

$$t_1 = \frac{Q^2}{(g \Delta Q)^{2/3} \nu}, \tag{1.2.4}$$

obtained by Chen from imposing matching conditions to the asymptotic regime spreading rate results, where $\Delta = \frac{(\rho - \rho_a)}{\rho_a}$.

For an extension of Chen's analysis to deduce an order of magnitude expression which considers viscous and inertial terms together in a balance with buoyant forces, consider figure 1.2. The gravity current source fluid is supplied at $x = 0$ with no x momentum and at a constant volumetric flow rate per unit span, Q. The control volume shown is of length L, and the position of the current front, x, is such that $L - x = \epsilon$ and $0 < \epsilon << L$. The thickness of the current layer is denoted by h, and μ is the viscosity of the current fluid. The net hydrostatic force in the x direction on the fluid in this volume can be written:

$$F_b = F_1 + F_2 = \rho g \frac{h^2}{2} - \rho_a g \frac{h^2}{2},$$

while the indicated boundary layer thickness, δ_v , has an associated viscous shear stress,

$$\tau_w = \mu \frac{v}{\delta_v},$$

and assuming an equivalent shear stress exists at the ambient fluid/current layer interface and also acts along the layer length x, gives a viscous resisting force of:

$$F_v = 2\mu \frac{v}{\delta_v} x .$$

The net momentum flux through the control volume is simply:

$$\rho_a v^2 h ,$$

and the time rate of change of the momentum contained within the volume is:

$$\frac{\partial}{\partial t} \left[\rho x v h + \rho_a (L - x) v h \right] \approx \rho v^2 h - \rho_a v^2 h ,$$

where the approximation that $\frac{\partial v}{\partial t} = 0$ has been made. Conservation of momentum, that the time rate of change of the momentum in the volume together with the net momentum flux through the volume is balanced by the net force on the volume, can then be formulated as:

$$\Delta g \frac{h^2}{2} = v^2 h + 2 \frac{\nu v x}{\delta_v} ,$$

which, using $Q = vh$, can be simplified to:

$$\frac{v}{(g \Delta Q)^{1/3}} = \frac{1}{\left(2 + \frac{4}{Re_x} \frac{x}{h} \frac{x}{\delta_v} \right)^{1/3}} , \qquad (1.2.5)$$

where $Re_x = \frac{vx}{\nu}$. Using for δ_v the laminar boundary layer result,

$$\frac{\delta_v}{x} = \frac{5}{\sqrt{Re_x}} ,$$

equation 1.2.5 recovers equation 1.2.1 for the inviscid asymptotic limit (x small or Re_x large), and equation 1.2.2 for the limiting case of x infinitely large or Re_x small. The two terms in the denominator of the righthand side of equation 1.2.5 represent the inertial and viscous forces, and setting their magnitudes equal

gives an expression for the downstream position, x_t, at which inertial to viscous dominated flow transition can be expected to occur:

$$\frac{x_t}{h} = \frac{25}{4} Re\,, \tag{1.2.6}$$

where $Re = \frac{vh}{\nu}$. The assumptions leading to the viscous term in the analysis, however, do not hold for $\delta_v > h/2$, which can be shown to occur for

$$\frac{x}{h} = \frac{Re}{4}\,.$$

Thus, the above analysis and the result of equation 1.2.6 is not expected to accurately represent the functional dependence of transition length on the parameters Re and h. These heuristic arguments and gravity current transition from inertially to viscous dominated flow regimes are further discussed in section 2.4.

To understand more fully the role the head of the current plays in these flows, consider the following example as examined by Wilkinson (1982). Figure 1.3 illustrates a series of cases, the first of which depicts the resulting flow after one end of a horizontal tube filled with water is suddenly removed. Benjamin (1968) showed that the intrusion of air occupies exactly one-half of the height of the tube and that the lighter fluid penetrates into the water at a constant velocity given by:

$$V = \sqrt{\frac{g\,h}{2}} \tag{1.2.7}$$

where h is the height of the cavity, and the density of the upper current fluid is taken to be small compared with that of the ambient dense fluid. When this latter assumption does not hold, the gravitational acceleration is just scaled by the density difference ratio, Δ. Benjamin demonstrated this case to be energy conserving, and Zukoski's (1966) experimental work on the motion of long bubbles in closed tubes supported this result. In the second view of figure 1.3 a

small weir which partially obstructs the critical flow of water exiting the tube produces an unsteady flow as viewed from a frame of reference moving with the front of the cavity. While this front continues at its constant velocity, Wilkinson observed an undular bore propagating upstream along the interface between the two fluids, although with a celerity less than that of the front. The liquid depth upstream of the bore is greater than the one-half duct height depth observed between the front and the bore. This increased height serves to reduce the volumetric flow rate into the less dense current layer. As blockage is increased further by the weir, the bore increases in speed and in energy dissipation, while the liquid level upstream of the bore rises until a value of about .78 of the duct height is reached. At this point the bore travels at the same velocity as the front, and hence, a steady flow regime has been reached. For even more blockage, the liquid level upstream of the bore continues to rise , with the bore overtaking the energy conserving portion of the flow, establishing a steady, energy dissipating flow regime as depicted in the final view of figure 1.3. In this regime, the front velocity, along with the upper layer volumetric flow rate and thickness, decrease as the obstruction is increased. The frontal velocity and layer thickness are functions of the density difference ratio and volumetric flow rate of the gravity current fluid (which is equal to the volumetric outflow rate of the ambient fluid) in this regime.

Early experimental work by Schmidt (1911), employing density differences induced by temperature differences in water, demonstrated the dependence on Reynolds number of the shape and degree of mixing activity of the gravity current head. Figure 1.4 shows this dependence, with view (a) representing a dense underflow with $Re = \frac{Vh}{\nu}$ (where V is the velocity of the front, h the thickness of the layer, and ν the kinematic viscosity) of less than 100, while view (f)

shows the characteristics of a front with Re of greater than 1000. In this last view, streams issuing from behind the head are a result of Kelvin-Helmholtz instabilities (Simpson 1969), and evidence the outflow of entrained fluid from the head.

In the frame of reference of the head, several volumetric fluxes can be identified, and are represented in figure 1.5. Coming into the head from the upstream direction is a flux of current fluid of the order 20% of the current source volumetric flux, as measured by Winant and Bratkovich (1977) for a current with Reynolds number based on head velocity and thickness of about 20,000 and whose density difference resulted from salinity differences in water. From the downstream direction, an influx of ambient fluid penetrates the current head, the result of the overriding of ambient fluid by the charging head. These two inflows are depicted as Q_1 and Q_2, respectively. A stagnation point near the foremost point, or nose, of the current head terminates the streamline bounding this overridden flow. Emanating from behind this stagnation point is a line separating two regions of circulation with opposing senses, which also bounds the outflow Q_3 necessitated by the the no-slip condition at the wall. Q_4 is the balance of flow required to satisfy mass conservation and was discussed above in regards to view (f) of figure 1.4. A plan view of the current front reveals clefts which are produced by the overriding of ambient fluid by the head, resulting in a gravitational instability (Simpson 1972). In addition to the three-dimensionality that this overridden flow imparts to the current head structure, this phenomenon is also responsible for a substantial portion of the current entrainment (Simpson 1982), while the interface upstream of the head is gravitationally very stable and entrains very little. This result is supported by the work of Ellison and Turner (1959), who treated the current as an entraining jet whose entrainment

varied with Richardson number, $Ri = \frac{g(\rho_a - \rho)h}{\rho_a U^2}$, where h represents the current thickness, and U the local velocity maximum in the layer. They studied the interfacial entrainment as a function of slope of the duct for a saline underflow into fresh water and found it to be negligible for small slopes. In addition, they studied the entrainment of a two-dimensional surface jet (a light fluid overriding a heavy ambient fluid with a free surface) as a function of Richardson number and found it to vanish as Ri increased to approximately 0.8. The absence of significant shear at the lower boundary of a dense underflowing gravity current, or at the upper boundary of an overflowing layer, such as in the case of a free-surface spreading current or surface jet, will affect the scenario in figure 1.5 to the extent that the region of circulation induced by the shear, the outflow Q_3, and the overridden inflow Q_2 do not exist. Although total entrainment by the head would be expected to be lower in this case, Luketina and Imberger (1986) measured head entrainments comparable to the current volumetric flux for large scale oceanographic surface currents with head Reynolds numbers as high as 10^6, although the flows studied did not have constant source volumetric flow rates or completely two-dimensional geometries. This suggests that the entrained inflow Q_5 increases its importance relative to Q_2 as the Reynolds number increases, and this is further substantiated by Simpson's (1972) conclusion that the height of the current head nose above the lower boundary decreases relative to total head height with increasing Reynolds number. This influx Q_5 is probably a result of the shear layer entrainment in the head, and both Luketina and Imberger's and Winant and Bratkovich's measurements of local gradient Richardson numbers indicate that they are too low to suppress shear instability in this region of the head, as illustrated in figure 1.5.

Another study involving the spread of gravity currents along the ceiling of

a sloping channel was performed by Georgeson (1942). The currents in this case consisted of methane flowing into an inclined hallway filled with air, and of hydrogen into air. The duct in this case was 100 ft. long with a 6 ft. height and 5 ft. width, with an upward slope of 1 in 10. Larger scales are required using gaseous media as compared to those needed for saline/water flows; approximately a factor of six is required to produce flows of the same Reynolds number, Richardson number, and density difference ratio. This is one of the few examples of gravity current experiments with density ratios Δ not small compared to one. In addition, gaseous gravity currents have much higher molecular diffusivity to momentum diffusivity ratios (or lower Schmidt numbers) than do their liquid counterparts.

Equally uncommon in the field of gravity current study is the investigation of heat transfer effects on the propagation of currents whose density differences are the result of temperature differences, such as the work of Koh (1971), who analytically examined the effect of entrainment and surface heat loss on two-dimensional free-surface warm jets. The surface heat flux studied in Koh's work was not large compared with thermal conduction to the ambient fluid, as it considered an atmospheric upper boundary to the surface jet.

1.3 Perspective and Goals of this Research

While a large body of literature exists concerning the subject of adiabatic gravity driven currents, the antithesis is true for their heat exchanging counterparts. A great majority of the experimental studies of gravity currents involved the use of different salt concentrations in water to produce the various density differences required. This technique is also amenable to flow visualization, such as through the use of dye in one of the fluid media. This method of producing density variations, however, is restricted to producing flows with density differences between

the ambient fluid and the fluid in the current of less than 15% of the ambient fluid density. Flows produced in building fires can have such density ratios on the order of 50% or higher, and have considerably higher molecular diffusion rates as compared to those in aqueous flows. In spite of these differences, this adiabatic variety of gravity current serves as a low density difference, vanishing heat transfer limiting case for the heat convecting current, and allows simple visualization of qualitative features common to both types of gravity currents. Consequently, the study of non-heat transferring density currents serves as a precursor to the heat transferring case examined in chapter 3.

This latter case, in which heat transfer from the overheated current fluid to the surroundings affects the development of the flow field, is consequently of significant interest to the author from the standpoint that this topic has not been the subject of extensive attention, as well as because of the previously mentioned importance its understanding plays in the progress of building fire research. This is especially true for the case of the heat transferring ceiling jet, as opposed to the free-surface boundary condition surface jet, and it is the former case which is most relevant to fire research. Understanding the mechanisms governing such flows can be invaluable to the formulation of practical building fire models and to the subsequent utilization of them in building fire safety codes.

As a more concrete example of a heat transferring gravity current of the type focused on in this work, consider the sequence of events portrayed in figure 1.6. In the first view, an unwanted fire in a room adjoining a long hallway of a building is represented. As this fire burns, entraining ambient air into its plume, it forms a mixed ceiling layer of hot products of combustion and air. As this layer deepens, it will begin to spill out over the door soffit and into the hallway. This flow will often be supercritical in the sense that its velocity will be greater

than the gravity wave speed at the interface between the two fluids, and hence it will be independent of downstream conditions. This high Froude number flow (greater than one), where $Fr = \frac{U}{\sqrt{\Delta g h}}$, while stable in the Rayleigh-Taylor sense, is unstable in the sense that it will undergo a hydraulic jump, as indicated in view (b). At this jump the gravity current becomes subcritical, $Fr < 1$, and also entrains significant amounts of ambient fluid. We will assume that a constant volumetric flux of the current here is a good approximation for many applications, or that the combustion rate of the source fire does not vary appreciably during the time period of interest in the evolution of the ensuing flow. A current develops along the ceiling whose thickness and velocity are set by the volumetric flow rate of the source fluid, its relative density difference, and the heat transfer rate to the surroundings. This heat flux is produced primarily by the mechanism of convection, and is absorbed principally by the ceiling. An equivalent volumetric flow rate must be extracted from the hallway, as no significant pressure rise would be supported by the structure, and in this example most of the displaced ambient fluid exits at the far end of the hallway, while some ambient fluid is entrained by the source fire. Other boundary conditions for the removal of ambient fluid, such as the case of displaced fluid exiting at the same end that the source fluid is introduced, can be examined through a Galilean transformation provided viscous effects can be neglected. In view (d) the current head has reached the hallway end and a reflected interfacial wave returns. Moving upstream, the wave can be observed to flood the inlet hydraulic jump in views (e) and (f), with the entire layer continuing to deepen with the continued addition of source fluid.

The speed with which these products of combustion move through the structure clearly is an important factor as far as occupant safety is concerned, as are the characteristics of heat transport and the possibility of flashover occurrences.

Since these characteristics, including the current spreading rate, can be greatly affected by flow boundary conditions such as the presence of ceiling cross-beams and superposed ambient flows, examination of these effects, in addition to the basic flow features, is undertaken in this work. Hence, the understanding of the interdependence of the heat transfer mechanism with the fluid dynamics of the heat transferring gravity current, together with the development of quantitative modelling of the flow, is the primary goal of this work, and will be pursued with an emphasis on the experimental approach. Study of the adiabatic current will promote qualitative understanding of current flow characteristics and environmental interactions, and aid in the quantitative study of the relative effects of viscous, buoyant, and inertial forces in the flow of gravity currents in general.

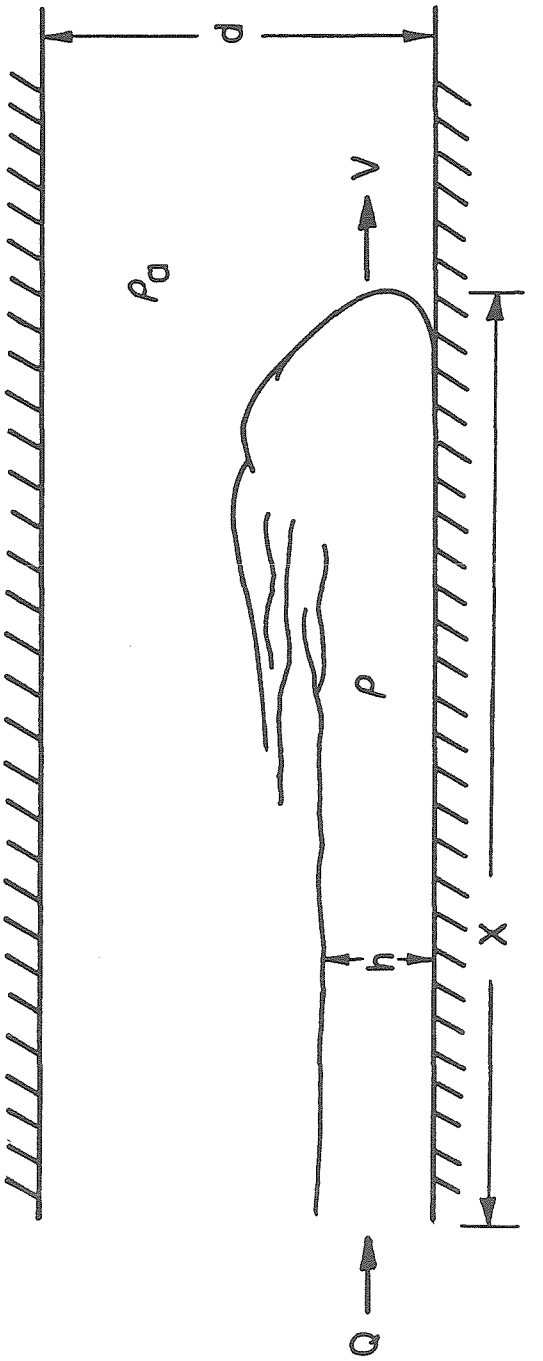

Figure 1.1 Gravity current geometry.

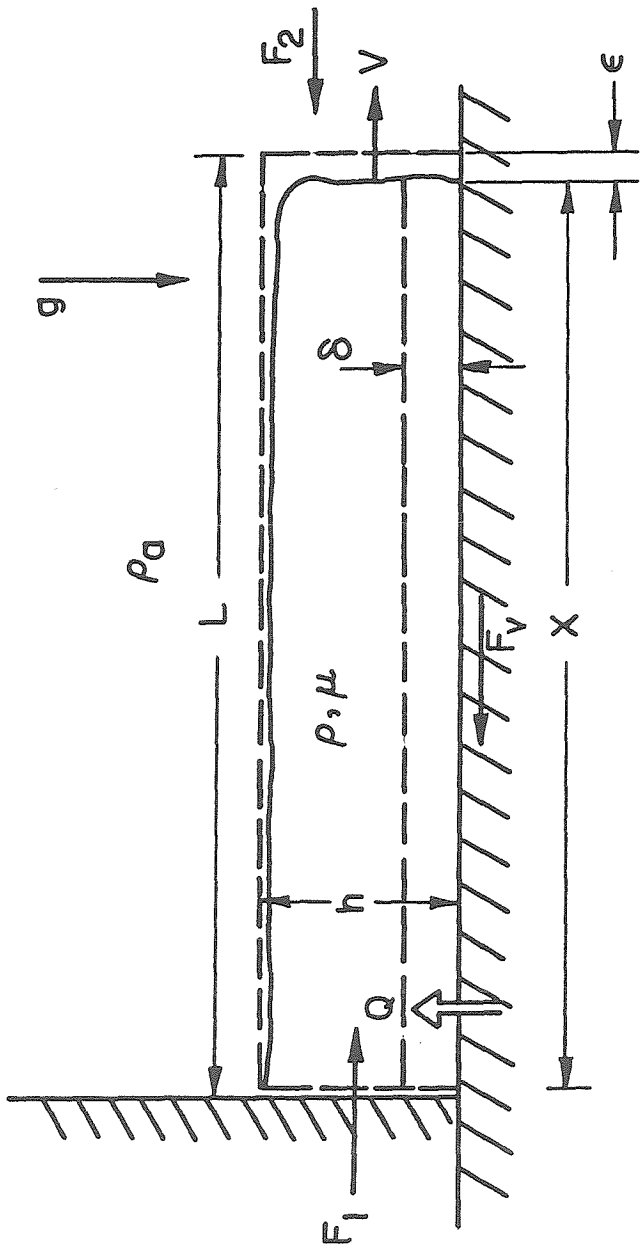

Figure 1.2 Two-dimensional gravity current model features.

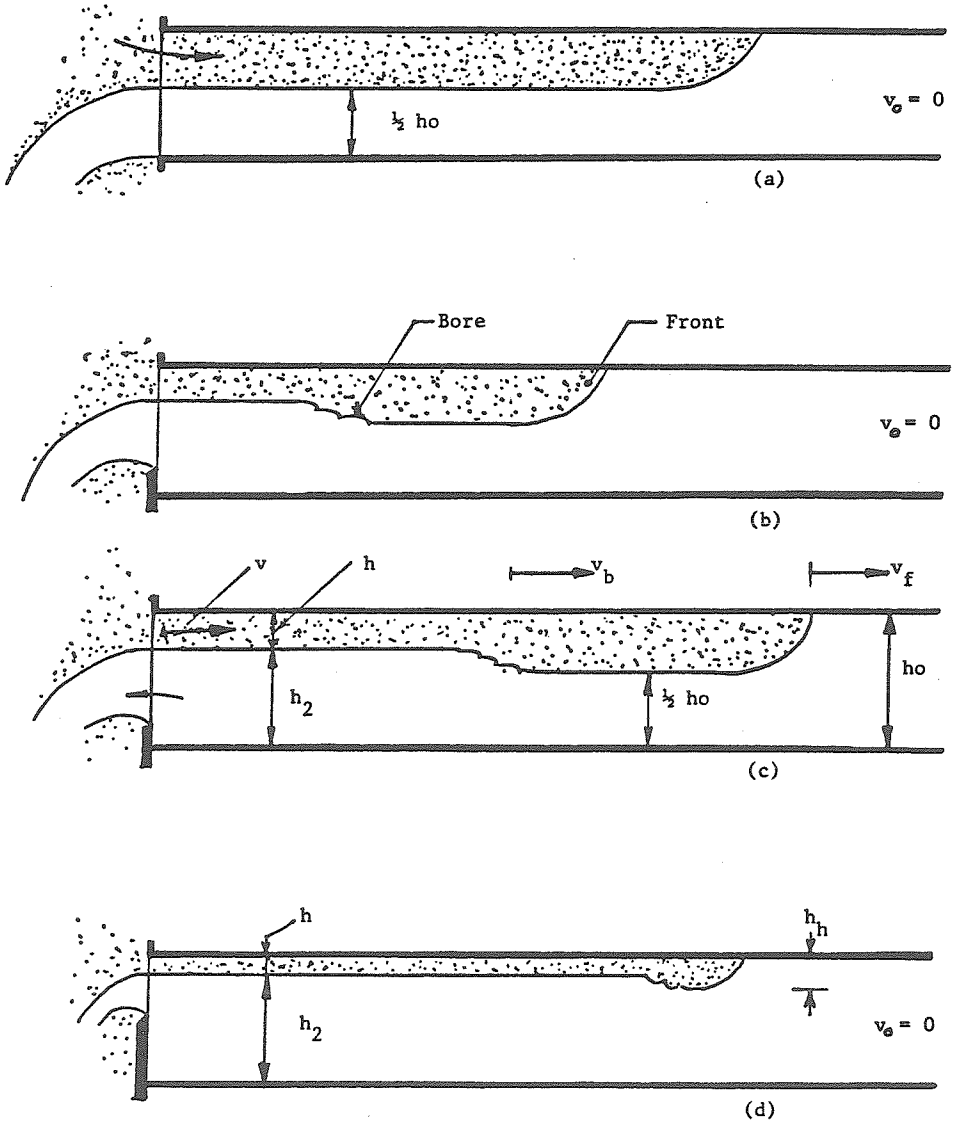

Figure 1.3 Gravity current flow regimes: (a) Constant energy; (b) +(c) Unsteady; and (d) Steady flow regime.

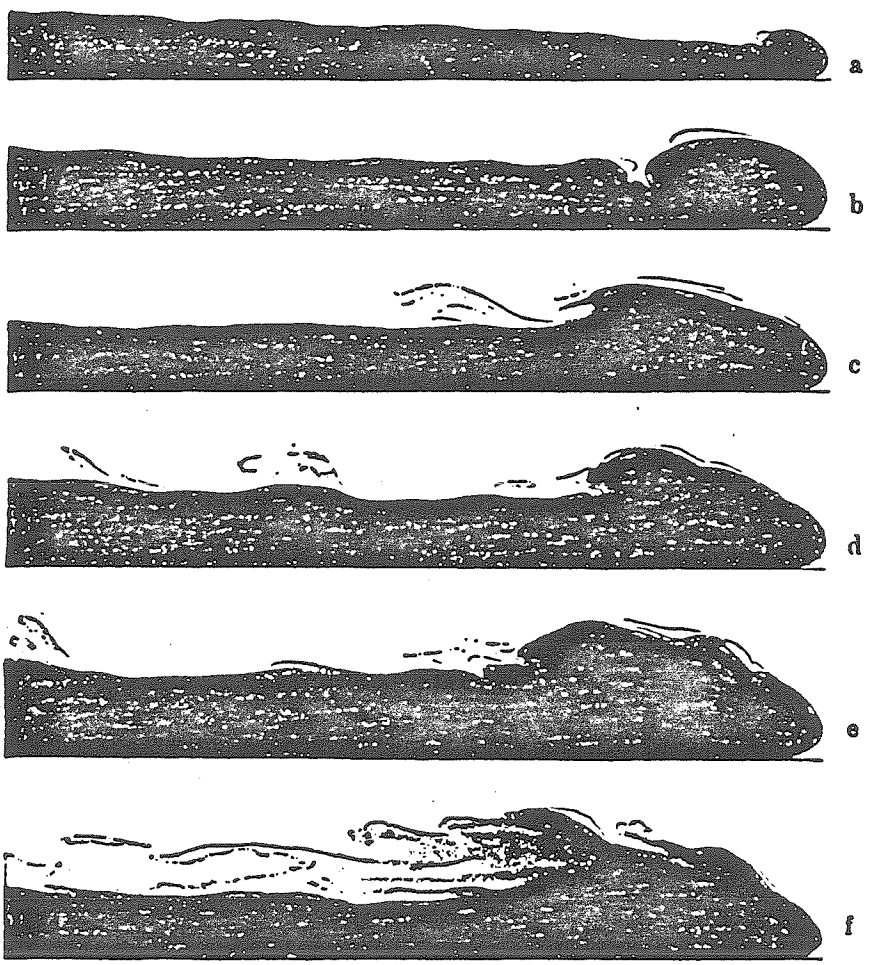

Figure 1.4 Variation in gravity current head structure with increase in Reynolds number, from Schmidt (1911).

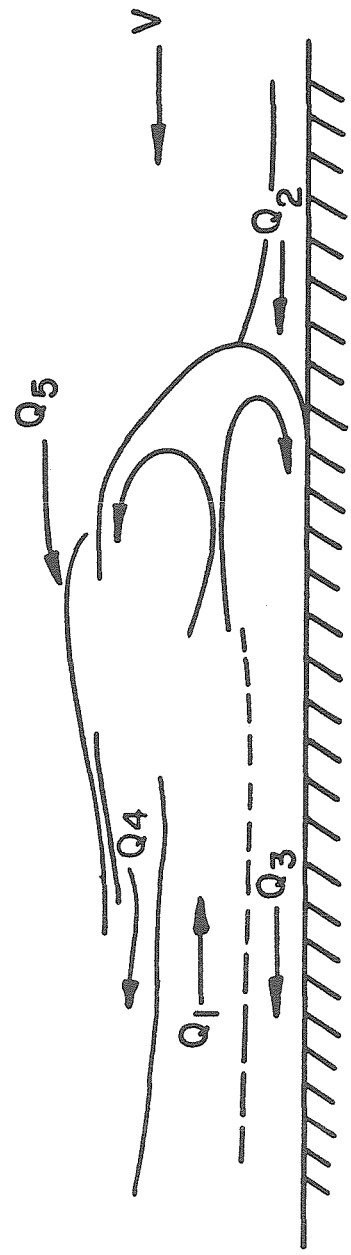

Figure 1.5 Flow field in gravity current head frame of reference.

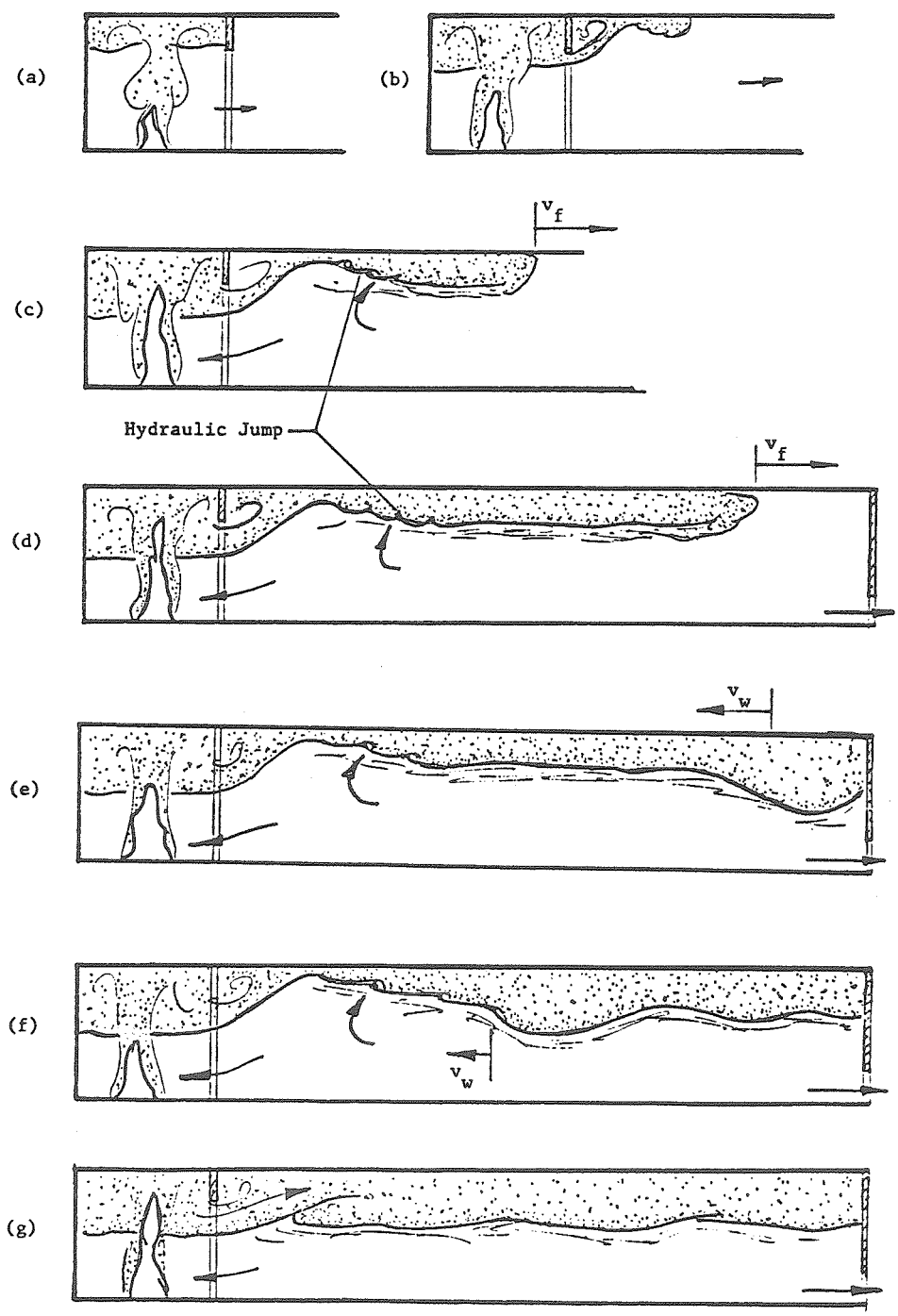

Figure 1.6 Thermal gravity current in hallway of burning building.

Chapter 2

Experimental Study of Adiabatic Gravity Currents

2.1 General Comments

In order to more completely understand the effects heat transfer has on the fluid mechanics of non-adiabatic gravity currents, an experimental study of both quantitative and qualitative nature concerning adiabatic currents is first in order. As mentioned earlier, that although a great deal of previous work has examined the many flow characteristics of non-heat transferring gravity currents, additional investigation of these flows in this work will provide first-hand insight into the behavior of gravity currents in general, and will promote the design and development of the heat transferring current study documented in the next chapter. In addition, there are issues concerning such flows that are not currently fully resolved, such as the subject of gravity current entrainment, and also the matter of qualitative characteristics of gravity current interactions with various flow boundary conditions. These two issues are very pertinent to the major goal of this work, as discussed in section 1.3, and are also amenable to effective study in the simpler adiabatic current case. In light of this, experiments performed with non-heat transferring currents will cover a variety of topics, with the hope that the results, when examined in the context of previous works, will contribute to the formulation of a consistent, unified model applicable to heat transferring currents as well. As mentioned previously, gravity currents of two-dimensional configuration are the focus of this work and this geometry will thus be the assumed one throughout the subsequent text.

As in many earlier experimental investigations of gravity currents, a liquid

medium is chosen here as the working fluid due to the smaller scales required, as compared to those needed in gaseous experiments, in order to achieve the desired range of flow conditions- from viscous dominated cases to inertially dominated flows. Reynolds numbers above 1000 based on current head thickness are required to achieve "fully developed" gravity current flow, the case in which the current head has developed the complete circulation and mixing structure discussed in section 1.2. In addition, flows in burning buildings, although in gaseous media, are of scales sufficiently large to represent Reynolds numbers in the thousands and higher. Consequently, such Reynolds numbers must be obtainable in both the adiabatic and heat-transferring phases of experimentation.

At this point, defining "typical" conditions in such full-scale flows as the building-fire-induced gravity flows, whose understanding is relevant to the goals of this research, is of benefit, and figure 1.5 is thus recalled. While local temperatures in a fire in a room of a structure, as shown in fugure 1.5(a), can exceed 1100 degrees Kelvin, the bulk temperature of the combustion products mixed with entrained ambient air will be much lower. Consider the case of such a fire liberating heat at the rate of 100 kilowatts, in which the plume entrains surrounding air such that the mass flux in the plume at a height 3 meters above the floor is approximately 2 kg/sec, consistent with fire plume entrainment measurements of Cetegen(1982). Assuming homogeneity of the constituents of the plume at this point (approximately the height of the door soffit) implies a bulk overheat of about 50 degrees Centigrade of this buoyant fluid source. Further assume the dimensions of the adjoining hallway to be 2 meters in width, 3 meters in height, and a length of 40 meters. Calculating the volumetric flow rate per unit span, Q, of this source fluid:

$$Q = \frac{\dot{m}_p}{\rho \mathrm{w}},$$

where $\dot{m}_p$ is the mass flux of the source fluid, ρ is its density, and w the hallway width, gives $Q = 1.0\,\mathrm{m}^2/\mathrm{sec}$. This in turn gives a Reynolds number,

$$Re = \frac{u\,h}{\nu} \doteq \frac{u\,\frac{Q}{u}}{\nu} \doteq \frac{Q}{\nu},$$

of about 5×10^4 for this full scale example.

In terms of the reference length and time scales for gravity current propagation given in equations 1.2.1 and 1.2.2, this flow rate and density difference yields:

$$R_1 = 4.4 \times 10^4 \text{ meters},$$

$$t_1 = 3.6 \times 10^4 \text{ seconds}.$$

From log-log x-t plots of two-dimensional gravity current fronts, Chen inferred values for the position and times of transition from inertially to viscous dominated current propagation of approximately,

$$\begin{aligned} x_t &= .1R_1\,, \\ t_t &= .1t_1\,. \end{aligned} \tag{2.1.1}$$

Hence, our flow example is confined to the purely inertially dominated flow regime, since the hallway length of 40 meters is much smaller than $.1R_1$ (4400 meters), assuming, for now, that these results have some bearing on the heat-transferring current behavior. The implied velocity in the inertially dominated regime of approximately:

$$V = \frac{.1R_1}{.1\,t_1},$$

gives a current head velocity of about 1.2 m/sec and a layer thickness of about .8 m, not differentiating at this level of approximation between the current head velocity and the current layer velocity maximum. The corresponding aspect ratio of the current layer cross section is about 3:1 and the layer occupies about one

quarter of the total hallway height. Although it is not suggested here that these adiabatic gravity current scaling laws accurately describe the heat-transferring example current, their results are used to determine the orders of magnitude of the characteristic features of the experimental models used in both the adiabatic and heat-transferrring cases.

2.2 Experimental Apparatus Description

In order to examine the basic characteristics of adiabatic gravity currents as described in the previous section, a long rectangular duct with a six-inch square cross section and 8 foot length, supported by a steel brace structure, was used as the experimental apparatus. Half-inch thick lucite was used for construction of all sides of the duct, and both lucite and transparent flexible tubing were used for the necessary plumbing to allow visual monitoring of the working fluids. In addition, since the gravity current was to occupy a small fraction of the total volume of the enclosure, the current fluid was chosen to carry the dissolved salt and dye required to produce the necessary density differences and visibility relative to the ambient fluid. Food-grade salt and Kriegrocine blue dye served these purposes well. Fresh water acted as the ambient fluid, while the specific gravity of the salt water source fluid varied over the range 1.006 to 1.150.

Figure 2.1 shows a schematic of this apparatus with the tank in its horizontal orientation. Provision for the removal of ambient fluid displaced by the current is made at both the inlet and downstream ends of the tank, and these drains may be open or shut individually, allowing for different flow conditions of the ambient fluid to be examined. The denser current fluid is supplied from below the inlet-end floor to help establish a consistent starting condition for the current, free from the influence streamwise momentum of the injected fluid would exert. An expanded section of inlet tubing and a wide entrance region to the duct floor were

used, together with a perforated plate and plastic wool-like material, to break up the entrance jet at the inlet section of the tank, and thereby minimize vertical disturbances to the starting region of the flow. Upstream of the inlet section of the channel is a constant pressure-drop, variable-area flow meter, or rotameter, whose calibration curve for fresh water can be seen in figure 2.2. Volumetric flow rates of fluids through the flow meter with specific gravities other than 1.0 can be calculated using the experimentally verified correction factor:

$$\frac{Q_{fluid}}{Q_{water}} = \sqrt{\frac{\rho_{water}}{\rho_{fluid}}} \sqrt{\frac{\rho_{float} - \rho_{fluid}}{\rho_{float} - \rho_{water}}},$$

where ρ_{float} refers to the flow meter indicator float's density. Flow meters of this type are typically accurate over a range spanning one order of magnitude, which consequently allowed flow rates ranging from as low as 30 and as high as 300 cm^3/sec to be used in this apparatus. Current fluid was supplied to the flow meter from a container of 40-gallon capacity, situated 10 feet above the meter in order to provide sufficient hydrostatic head to overcome the pressure drop of the supply circuit. This also ensured that changes in the liquid level in the supply reservoir did not significantly affect the total head, and hence the flow rate, of the current fluid during the progress of a run. The resulting pressurization of the tank demanded sturdy construction and effective sealing of all joints and fittings of the apparatus, a condition much easier reached in theory than in practice.

A tank of approximately 50-gallon capacity located at ground level contained the current solution during its mixing by a 1/3 horsepower centrifugal pump prior to the execution of a run. In addition to recirculating the saline solution to expedite the salt's dissolving, the pump provided the means to transfer the mixed solution to the upper supply container via tubing accessed by blocking the recirculation loop and opening of the appropriate gate valve.

A tape measure was secured to the forward edge of the tank floor to mark the current front's progress, and transparent rules were mounted vertically at various locations on the tank face to record current head and layer thicknesses. Fluorescent lighting fixtures at the rear face of the channel enhanced the contrast of the fluid media, facilitating photography of the current by video camera, the principal data recording device of this phase of experimentation. This camera, together with a monitor and video cassette recorder capable of injecting running time data into the video signal, was mounted on a cart free to traverse in the streamwise direction. Mounted on this cart also was a strobe light, flashing at 30 cycles per second (the framing rate of the VHS format video cassette recorder system), in order to illuminate the tape measure and allow a video image to be produced free from blurring that would have otherwise resulted from the rapid panning of the video camera that was necessary to keep abreast of the travelling current head.

Located above the channel and inclined 45° downward were two 4-foot by 9-inch mirrors end to end, which allowed observation and photography of the plan view of the gravity current as it flowed along the channel floor. A white, opaque background under the floor provided a contrasting backdrop for viewing the current from above. The channel's horizontal inclination could be easily adjusted to create a sloping duct, although quantitative results of experiments performed using non-horizontal configurations will not be discussed here.

2.3 Experimental Procedure

The experiments performed on adiabatic gravity currents with the horizontal liquid tank apparatus described in the previous section can be classified into two categories, namely those of quantitative measurements and qualitative observations. The purpose of the quantitative measurements was to demonstrate the

dependence of current front propagation rates on the relative density difference, Δ, and the source volumetric flow rate per unit span, Q. In addition, a simple entrainment measurement technique was used to quantify the mixing between the gravity current fluid and the ambient fresh water as the current flowed. Qualitative experiments focused primarily on revealing the characteristics of the current head and layer as functions of the flow parameters Δ and Q, and also on the influence various flow boundary conditions had on the fluid flow of the current.

Each of the quantitative experiments carried out can be characterized by the two parameters, Δ and Q. Since for all cases examined the fraction of the duct height occupied by the current was small, the influence this relative thickness had on flow behavior was assumed to be small, although this relationship was investigated. The range of density ratios available was determined by the technique used to achieve the density difference, i.e., the dissolving of salt into water. For concentrations of salt yielding specific gravities above 1.10, considerable time and mixing was required for complete dissolution of the salt, hence levels significantly greater than this were not used frequently for the specific gravity of the current fluid, although complete saturation would not occur until a specific gravity of about 1.19 were reached at room temperature (25° C).

At concentrations yielding 1.10 specific gravity, the absolute viscosity of the saline solution increases by approximately 30% as compared to fresh water, and hence the kinematic viscosity, $\nu = \frac{\mu}{\rho}$, increases by about 20%. In most instances, this change can be neglected in terms of its effect on length scale, time scale, and Reynolds number calculations, particularly for cases with lower specific gravities. Thus, the median density difference ratio of .05, together with the flow rate of 190 cm^3/sec, corresponding to the half-scale reading of the chosen flow meter, prescribes an inertial-viscous transition length scale, $.1R_1$, of about

2 meters, roughly the chosen length of the duct. Hence, by varying Δ or Q from this nominal condition, flows more viscous or more inertially dominated in the buoyant force balance sense can be examined, with both extremes being reasonably well represented. Transition lengths as long as 6 meters (much greater than the duct length and thus indicating a purely buoyancy-inertial influenced flow field), and as short as 30 centimeters (suggesting a primarily viscous-buoyant force balance flow) are within the scope of the experimental parameter matrix. The maximum values of the parameters allow a Reynolds number of about 3000 based on current head properties.

Upon the selection of the parameters Δ and Q for a particular experiment, salt and dye were added accordingly, and the mixture transferred to the elevated reservoir, while the duct was filled completely with fresh water. Specific gravity measurements were made while the fluid was mixed in the larger reservoir with the use of hydrometers, having resolutions as fine as .0005. The source fluid was then fed into the inlet section of the duct at a relatively slow rate to inhibit the occurrence of mixing at the interface between the dense source fluid being supplied and the ambient fluid. When this interface in the inlet section just reached the opening in the channel floor above the inlet section, a gate valve at the inlet to the rotameter was abruptly opened further until the float in the meter indicated the desired flow rate. The video cassette camera then followed the current front downstream. Since the focal distance used for the camera was typically of the same order as that of the spanwise dimension of the current layer (6 inches), considerable parallax error in determining the current front postion relative to the tape measure located at the bottom of the duct face could be introduced unless care was taken to maintain the current head in the downstream-side half of the field of vision of the camera. An analogous precaution was necessary for

the vertical direction, concerning the measurement of layer and head thicknesses relative to the rules mounted vertically on the face of the duct. Playback of the video with the recorder in still-frame mode allowed position of the front versus elapsed time to be recorded at regular real-time intervals, since running-time data was recorded on video-tape concurrently with the gravity current image. The majority of the experimental work and data reduction involving these saline flows was performed in conjunction with Young (1984). A total of approximately 50 runs were performed during the course of the adiabatic current experimentation.

While all of the above quantitative measurements employed the use of the video camera following alongside of the current front, a series of measurements were performed with the camera located at a fixed downstream position. This allowed for the examination of local current layer thickness time dependence.

Another quantitative measurement performed using this apparatus consisted of the determination of the extent of inter-fluid mixing between the current and ambient fluid by comparison of the resulting volume of dyed fluid in the duct following a run to the known source fluid volume supplied during the run. More specifically, the progress of the current front was timed from its starting condition of spilling out through the entrance slot at the inlet, to its arrival at the end wall of the duct. When the current reached the end wall, the supply of source fluid was promptly halted and the elapsed time noted. The product of this time interval with the measured flow rate during the run gave the volume of dyed source fluid supplied into the channel. After the wavy motions of the interface resulting from the current's collision with the end wall decayed to the point that a quiescent dyed layer of fluid resided at the duct bottom (typically after about one minute), the height of this layer was measured, giving the total volume of dyed fluid in the channel. Diffusion at the interface of dye and salt did not

create difficulties with this procedure as changes in the interface thickness due to diffusion were negligible over time scales of many minutes in this gravitationally stabilized configuration. Since a very low concentration of dye was required to render the saline solution essentially opaque, and considerably more dye than this nominal amount was used, practically all of the ambient fluid mixed by the current should have appeared as part of the tranquil dyed layer resulting from the mixing experiment as described above. The fact that although mixing did occur, the resulting layer's color exhibited almost no gradation or variation in value supports this assertion.

In the realm of qualitative experiments, many different studies were performed. The variation of the flow parameters during the quantitative front propagation studies produced Reynolds numbers based on head thicknesses and velocities covering the range of about 100 to 3000. This allowed the gravity current head characteristics' dependence on Reynolds number to be observed, as well as the Reynolds number dependence of the shape of the layer (in particular, the interface inclination) upstream of the head to be assessed.

Also during the course of these runs, the interaction of the gravity current with its boundaries was observed. Examination of the reflection of the current upon its arrival at the end wall of the duct and of its behavior upon encountering a transversely oriented, square cross-sectioned obstacle was also performed with the aid of the video camera. In the latter case, a brass block of 3/4-inch height, spanning the width of the duct along the floor at a downstream position of about 60 inches, was used as the obstacle encountered by the current. Video monitoring of the current's negotiation of the obstacle was performed while panning alongside the current head and, in subsequent runs, by fixing of the camera postion at the block location. The duration of the video monitoring was of sufficient length to

permit observation of the end wall reflection's interaction with the flow at the barrier location.

Another series of experiments was performed with the intention of illustrating qualitative features of the gravity current frontal region. The set of inclined mirrors situated on top of the channel was used to photograph the plan view of the current front, with the aim of uncovering three-dimensionality of the current head. The procedure for this experiment was virtually identical to that for the side view spreading rate measurement runs, with the exceptions that the video camera was mounted some 8-10 inches higher on its cart for viewing of the mirror reflection, and the tape measure at the lower forward edge of the channel was turned face-up to allow visibilty from above.

One other study of current head dynamics involved observation of the intrusion of a dense gravity current into a duct containing less dense fluid and a thin layer of dense fluid residing at its floor. This thin layer consisted of fluid with the same density as the current fluid, with a depth much less than the ensuing gravity current head thickness. Video monitoring of the current as it flowed over this thin bottom layer recorded the qualitative character of the current head in this flow configuration.

2.4 Experimental Results

In this section, the quantitative results of the adiabatic gravity current experiments are presented and discussed, and are followed by a presentation and assessment of the qualitative investigation results.

2.4.1 Inertial-Viscous Transition

As described in section 1.2, transition from inertial-buoyant to viscous-buoyant dominated gravity current flow is accompanied by a change in the frontal

spreading rate of the two-dimensional current. In figure 2.3, an x-t diagram for a current front propagating in the aqueous-media horizontal channel is presented. This particular current had a density ratio of $\Delta = .10$ and a volumetric flow rate of current fluid per unit span of $Q = 10.3\,\mathrm{cm}^2/\mathrm{sec}$. In terms of the transition length discussed in section 2.1, these parameters give $.1R_1 = 110\,\mathrm{cm}$, and this value is indicated on the x-scale of the figure. The plotted experimental points begin to diverge from the straight line drawn through the lower points of the plot at x values near this transition value, indicating a deceleration of the current front due to the increasing significance of viscous shear forces with increase in downstream position of the front relative to the buoyant driving forces. Extrapolation of this straight line to the t-axis yields an effective time offset of 2.75 seconds, which is subtracted from real time to correct for the start-up transient condition in determining elapsed time of front propagation. A log-log plot of downstream position versus elapsed time can thus be produced and is displayed in figure 2.4. In this plot, the points below the value $.1R_1$ lie on a line of slope 1.00, exhibiting the constant frontal velocity as predicted by the buoyant-inertial force balance model. The decreasing slope of the curve beyond the transition region appears to approach the buoyant-viscous slope value of .8 with reasonably good agreement. While this experimental case demonstrates both of the asymptotic flow regimes of gravity current spread, figure 2.5 represents the x-t diagram for a current front with an expected transition at a downstream position greater than the channel length. This entirely buoyant-inertial flow displays a constant frontal velocity throughout, with the exception of the deceleration apparent over the final 20-25 cm (or 5 to 7 times the current head thickness) of the duct, which is attributable to the proximity of the end wall of the channel. This end wall effect was observed in all of the test cases, for all values of current Reynolds number and transition

length examined. The linear relationship between downstream position and time for the current front at positions upstream of the transition region was found to be consistent from run to run; the average value of the logarithmic slope over eleven runs was .99, with a standard deviation of .01.

The transition point from inertial to viscous-buoyant dominated gravity current flow, however, was not as consistent in terms of its relationship to the value of $.1R_1$. Table 2.1 shows the observed transition position versus current head Reynolds number for nine different cases covering a range of Reynolds numbers from 660 to 2700.

TABLE 2.1

Inertial-Viscous Transition, x_t, vs. Re, h

$Run\,\#$	$x_t\,(cm)$	x_t/R_1	Re	$h\,(cm)$	x_t/h
11	120	.4	660	.9	130
16	60	.2	810	.9	70
5	120	.2	1020	1.4	90
23	240	.15	1000	1.9	130
13	100	.1	1370	1.0	100
15	160	.1	1880	1.4	110
1	160	.1	2280	1.5	110
2	190	.1	2300	1.4	140
14	165	.06	2700	1.6	100

From these results, the dependence on Reynolds number of the inertial-viscous transition point defined as approximately $.1R_1$ by Chen (1980) can be inferred. Although this transition location is not sharply defined, as can be seen in figure 2.4, the transition position's value of the multiplicative constant of R_1

seems to display an inverse dependence on Reynolds number. From the definition of R_1 and the assumption that $Q \sim V\,h$ and $V \sim (g\,\Delta\,Q)^{1/3}$, we can write:

$$R_1 = \frac{Q^2}{(g\Delta Q)^{1/3}\nu_s} \sim \frac{Q^2}{V\,\nu_s} \sim h\,Re. \tag{2.4.1}$$

Thus, Chen's result of $x_t = .1R_1$, equation 2.1.1, shows the same dependence of x_t on h and Re as the model result of equation 1.2.6, which did not account for the presence of the current head in real flows. The result also made use of the assumption $Q = vh$, which is not accurate for currents in which the boundary layer occupies a significant fraction of the total current thickness, h. When the constant multiplying R_1 in the transition length scale expression is taken to be roughly inversely proportional to Re, the transition length is then approximately proportional to the layer thickness, h. The ratio of transition length to layer thickness is given in the rightmost column of table 2.1, and to the limited accuracy of 1 significant figure of the transition length, is a constant close to 100:

$$\frac{x_t}{h} \approx 100\,. \tag{2.4.2}$$

An analogy can be drawn between this gravity current transition length dependence on the characteristic flow dimension, h, and the entrance flow in a pipe, which becomes fully developed Poiseuille flow at about, coincidentally, 100 pipe diameters downstream.

2.4.2 Spreading Rate Constant

Since the functional dependence on time of the gravity current spreading rate has been determined for both inertially and viscous dominated flows, attention is now given to the dependence on flow parameters of the current front velocity. In the so-called inertial regime, or constant velocity spreading region, the frontal velocity must depend on the density ratio, Δ, flow rate per unit span, Q, and

the gravitational acceleration, g. These parameters produce a velocity in the following combination:

$$V = C\,(g\,\Delta\,Q)^{1/3}. \tag{2.4.3}$$

Although Benjamin (1968) presented results of frontal spreading rates versus the velocity scale:

$$V = C_1\,(g\,\Delta\,h)^{1/2}, \tag{2.4.4}$$

where h is the layer thickness, unless non-miscible fluids are used or local concentration profile measurements are made, scaling relative to h is not as accurate as is the use of Q. This is because typically Q is an experimentally measured quantity, and the measurement of h is not a simple matter, as it can be found to vary both with time and downstream position in a gravity current flow of constant Q (see the discussion given below). Furthermore, the measured value of h from flow visualization techniques must be correlated to vertical concentration profile measurements before it may be interpreted in terms of current layer thickness.

The constant of proportionality, C, between the gravity current frontal spreading velocity, V, and the cube root of buoyancy flux, $(g\,\Delta\,Q)^{1/3}$, was obtained from fifteen different entirely inertially dominated flows and is plotted against Reynolds number based on head thickness in figure 2.6. This plot reveals a weak correlation of C to Re, and indicates a variation in C from about .75 to .85 for Reynolds number change from roughly 1000 to 3000. This Reynolds number dependence of C suggests that even in the inertially dominated flow regime, viscous boundary layer effects may affect the magnitude of the spreading rate, if not its time dependence.

An investigation performed by Almquist (1973) employed fresh water gravity currents overflowing a saline ambient fluid. This free-surface configuration was devoid of a floor or ceiling boundary layer, and should therefore more closely

resemble the inviscid case examined by Benjamin, who obtained the result:

$$V = \sqrt{2\,g\,\Delta\,h}\,, \tag{2.4.5}$$

for the immiscible, inviscid gravity current spreading rate. This expression pertains to the frontal velocity of a gravity current in the steady flow regime, as described in section 1.2, in which the current fluid occupies a negligibly small fraction of the total channel height. In terms of the parameters Δ and Q, this expression for the front velocity becomes: $V = \sqrt{2\,g\,\Delta\,\frac{Q}{V}}$, and yields:

$$V = 2^{1/3}\,(g\,\Delta\,Q)^{1/3}. \tag{2.4.6}$$

For current head Reynolds numbers of about 400, Almquist's data imply a value of .9 for C, while for $Re = 800$, a value of 1.2 is obtained, very near the value 1.26 as given in equation 2.4.6. A Reynolds number dependence in this case could be attributed to viscous effects of the shear layer at the interface beteween the overriding current layer and the ambient fluid, and possibly to sidewall effects of the channel, as well.

Comparison of the present results to previous experiments performed using underflowing gravity currents reveals reasonable agreement in magnitude and Reynolds number dependence. Figure 2.7 shows the present results, including values of C calculated over the constant velocity flow region of flows in which inertial-viscous transition occured, plotted together with data from previous investigations. Data for low values of Reynolds number are limited, as such flows are almost entirely viscous dominated and exhibit very short constant velocity flow regimes. For values of Re as high as 100,000, Wilkinson (1970) found the constant C to be about 1.05. Although not a great deal of data for C in terms of the quantity $(g\,\Delta\,Q)^{1/3}$ are available for underflows in constant velocity inertial flow, the collective data show a tendency of C toward a limiting value

near 1.1. In terms of the velocity scale $\sqrt{g\,\Delta\,h}$, Keulegan (1958) saw a similar behavior with respect to Re, with the constant of proportionality approaching about 1.1. Possible influences on the variations in the constant C among various investigations, and on experimental scatter such as that exhibited in figure 2.6, include sidewall boundary layer effects due to the finite aspect ratio of the spanwise cross-section of the gravity current layer, channel blockage effects of the gravity current layer, and mixing effects at the current head. The sidewall boundary layer effect is thought to be small in the present experiments, owing to the relatively high layer cross-section aspect ratios used of 7 to 17. Keulegan, however, examined current front flows with aspect ratios of order one and found a strong dependence of current front velocity on this parameter.

The effect that the fractional height of the duct the gravity current occupies, h/d, where d is the channel height, has on the constant C can be considered by examination of figure 2.8. While no distinct correlation can be seen in this figure, together with figure 2.6 it suggests that we examine plots of C versus Re for fixed h/d, and C versus h/d for fixed (nearly) Re. These relationships are depicted in figures 2.9 and 2.10, respectively. In figure 2.9, a tendency for C to increase with Re is seen for fixed h/d, while an increase in C is apparent with increasing h/d in figure 2.10. The former result is in agreement with the previous observation that viscous retarding forces serve to reduce C and become less significant with increasing Reynolds number. The Reynolds number effect on mixing and the subsequent effect on C is not considered here. Hence, the latter result, C increasing with h/d for constant Re, when contrasted to Benjamin's analytical result that the constant $C_1 = \frac{V}{\sqrt{g\,\Delta\,h}}$ decreases with increase in h/d (and Re, since Δ was fixed), appears in disagreement, since C is related to C_1 in the manner $C = {C_1}^{2/3}$ for the case of inviscid, immiscible approximation. In light of the

discussion in section 1.2 concerning the relative flows in the current head frame of reference, it is clear that $Q = V\,h$ is not a good approximation for real flows, particularly for high Reynolds numbers such as those in the flows represented in figure 2.10. Thus the transformation from comparison of C versus h/d to the comparison of C_1 versus h/d is not a simple one. In addition, a rather limited range of values for h/d is examined in figure 2.10 so that a definitive conclusion about the relationship examined cannot be made. A further complication is the apparent dependence on viscous transition length of a gravity current flow on h as seen in the previous result, equation 2.4.2. For larger h (since in the experiment d was fixed by the apparatus), a more inertially dominated flow could have existed (assuming constant Reynolds number), with the correspondingly higher frontal velocity giving a higher value for the constant C, in spite of the blockage effect as examined by Benjamin.

This inviscid h/d effect was calculated by Benjamin in terms of C_1, and can be expressed in the following form:

$$C_1 = \sqrt{\frac{(d-h)(2d-h)}{(d+h)\,d}}. \tag{2.4.7}$$

For a flow with a value h/d of .1, close to the values used in this investigation, this relation implies a reduction in the value of C_1 from 1.414, for the infinitely deep ambient fluid case, to 1.247. The value of ${C_1}^{2/3}$ for this example is 1.16.

The effect that the underestimation of Q by the product $V\,h$ has on the transformation from C_1 to C can be examined as follows. From Winant and Bratkovich's (1977) experiment, a value for α in the expression $Q = \alpha V\,h$ can be inferred to be about 1.2, for a value of Reynolds number of 2×10^4. Using this relation, we can compute C from C_1:

$$C = \frac{V}{(g\,\Delta\,Q)^{1/3}} = \frac{V}{(g\,\Delta\,1.2\,V\,h)^{1/3}} = \frac{V^{2/3}}{(g\,\Delta\,1.2\,h)^{1/3}},$$

$$C^{3/2} = \frac{V}{(g\,\Delta\,1.2\,h)^{1/2}} = \frac{.9\,V}{\sqrt{g\,\Delta\,h}} = .9\,C_1,$$

or,

$$C = .93\,{C_1}^{2/3}. \tag{2.4.8}$$

This effect serves to reduce the idealized value of C=1.26, from equation 2.4.6, to C=1.17, closer to the values reported in figure 2.7. This effect should be more apparent for higher Re, as α is essentially 1 for non-fully developed low Re flows. Combining this effect with the h/d effect discussed above, a value for C for the 10% blockage case at high Re can be found to be $C = 1.08$, very close to the asymptotic limit apparent in figure 2.7.

2.4.3 Ambient Fluid Layer Effects

The position of the displaced ambient fluid exit in the channel is not believed to be of significant importance at the low values of h/d used in the present experiments. Comparison of the frontal velocities and layer thickness of two distinct cases, with identical flow rates and density differences but with different ambient fluid exit conditions, supports this hypothesis. One run of $Q = 7.6\,\mathrm{cm}^2/\mathrm{sec}$ and $\Delta = .0065$, with the exit orifice at the inlet end of the channel so as to create a cross-flow condition of the ambient fluid and current layer, had values of V and h of 2.69 cm/sec and 1.85 cm, respectively. The same parameters used with the exit located at the downstream end yielded a front velocity of 2.73 cm/sec and a thickness of 1.80 cm. The latter coflowing case exhibited a small increase in V and decrease in h, and an increase in C to .75 from .74 as compared to the cross-flow condition case. These differences are small and of comparable size to the experimental accuracy.

Accurate measurements of current layer thickness were particularly difficult to perform when interfacial waves were present. The results of the current mixing

experiments indicated that roughly 10% of the source flow Q mixes with the ambient fluid during gravity current flow with head Reynolds number of the order 1000. The limited accuracy of the technique used for entrainment measurement described in the previous section was primarily due to the uncertainty in the interface position following the settling down of the wavy current fluid layer.

2.4.4 Viscous Effects

While the previous discussion centered primarily on the quantitative behavior of inertially dominated gravity currents, measurements were also made of current layer thicknesses upstream of the current head as a function of time at fixed downstream positions to examine the viscous effects on the flowing current layer, particularly for viscous dominated gravity currents. Figure 2.11 shows measurements of this type taken at a position near the inertial-viscous transition point. The current head arrived at the measuring station at a real time of 34 1/3 seconds, while extrapolation of the data to this point on the horizontal axis yields a nominal thickness of the current layer of roughly 12mm. These points prescribe a time dependence of the data approximately of the form $t^{.45}$, close to the time dependence of the growth of the laminar viscous boundary layer, of $t^{.5}$. In the current head frame of reference a boundary layer can be modeled to originate from the downstream tip of the head, developing with upstream position as shown in figure 2.12. The expression for the laminar boundary layer displacement thickness:

$$\frac{\delta_1}{x} = \frac{1.72}{\sqrt{Re_x}}, \tag{2.4.9}$$

can be transformed temporally, using the relationship $V\,\triangle t = x$ to yield:

$$\delta_1 = 1.72\sqrt{\nu\,\triangle t}. \tag{2.4.10}$$

The data from figure 2.11, when a square root time dependence is used, give the

growth in thickness of the layer to be approximately of the form:

$$h(t) - h_n = 1.65\sqrt{\nu\,\triangle t}\,, \tag{2.4.11}$$

where h_n is the nominal thickness of the layer, in this case 12mm. Data points at times in excess of 94 seconds in figure 2.11 were not used in the calculation of this relationship since the current front had reached the wall at that time. Thus, the magnitude as well as the time dependence of the current layer growth was seen to agree well with boundary layer theory.

The relatively large fraction of the current layer thickness the displacement thickness occupied for flows of low Reynolds number based on streamwise distance, x, suggests a simple model to account for the growing displacement layer's effect on the net source fluid volumetric flow rate at the current front. This effect would serve to reduce the effective Q of the front, and thus increase the value of C for the flow. Consider the displacement layer illustrated in figure 2.12 to originate at both the leading edge of the front, as in the sketch, and at x=0, or the entrance edge of the channel floor. The volume of this layer can be expressed in the form:

$$\mathcal{V} = 2\int_0^{x/2} \frac{1.72\,x}{\sqrt{Re_x}} w\,dx, \tag{2.4.12}$$

where w is the width of the channel. Integrating, and letting:

$$\frac{1}{w}\frac{d\mathcal{V}}{dt} = Q_v,$$

where Q_v is the volumetric flow per unit span into the displacement layer, we get:

$$Q_v = \frac{3.44\,x^{1/2}}{2^{3/2}\left(\frac{V}{\nu}\right)^{1/2}}\frac{dx}{dt}. \tag{2.4.13}$$

Now use $\frac{dx}{dt} = V$, and the approximation that $Q = V\,h$ to get:

$$\frac{Q_v}{Q} = \frac{1.22}{\sqrt{Re_x}}\left(\frac{x}{h}\right). \tag{2.4.14}$$

Using a net flow into the front of $Q_n = Q - Q_v$, we can recalculate the value of C (calling it C_n) for a particular test run in which $Re_x = 50{,}000$ at $x = 1\,\mathrm{m}$, $h = 2\,\mathrm{cm}$, $Q = 17.2\,\mathrm{cm}^2/\mathrm{sec}$, $\Delta = .015$, $V = 5\,\mathrm{cm/sec}$, and $C = .80$:

$$\frac{Q_v}{Q} = .27, \quad Q_n = 12.6\,\mathrm{cm/sec}, \quad \text{and} \quad C_n = .88\,.$$

This effect clearly is more significant at lower Reynolds numbers, a characteristic consistent with the greater differences seen for lower Reynolds numbers in figure 2.7 between the measured values of C and the idealized result, as compared to those for higher Reynolds numbers.

2.4.5 Qualitative Flow Features

Qualitative observations of gravity current flows revealed several interesting characteristics. In terms of the current shape and mixing activity, a strong dependence on Reynolds number was observed. The leading edge of the current took on a wedge-like nature for low Re (in the range 100-200), with no visible mixing or turbulent activity. Upstream of the front, the layer exhibited increasing thickness, since flows of such low Re were primarily viscous dominated, with the boundary layer along the channel bottom occupying a significant portion of the layer thickness throughout the streamwise extent of the current. For higher Re, the current head height grew in relation to the layer thickness, reaching a limit of roughly twice the layer thickness for head Reynolds numbers exceeding 1000. Turbulent mixing activity increased accordingly, while the upstream inclination of the interface was reduced as Re was increased. For current flows in the inertial regime, no perceptible variation in layer thickness with downstream position was noted.

Upon the gravity currents approach to the end wall, its frontal velocity was observed to decrease slightly, beginning at a distance from the wall of roughly five

times the current head thickness. Upon reaching the wall, the current reflected a wave that propagated back upstream along the interface, while the current front itself turned upward, climbing several head heights up the end wall and falling back down. Upon this second impact, another wave was created which also moved upstream. These waves had amplitudes typically on the order of one-quarter the current layer thickness at the time of end wall encounter (if the source fluid supply was continued after reflection occurred, the layer deepended uniformly). An interesting feature of the reflected waves was that they displayed no mixing or turbulent activity whatsoever while traveling along the interface.

The encounter by a gravity current of an obstacle of height comparable to the current thickness produced another interesting sequence of events. Several runs were performed with various values of the parameters Q and Δ, while a transversely oriented obstacle was located about three-quarters of the distance along the channel floor. The current was able to scale the block in its path, sending a small reflection upstream while producing a breaking crest as seen in figure 2.13. On the downstream side of the obstacle, a hydraulic jump formed, producing an increasingly thick layer downstream until a subcritical condition was reached. This occurred approximately 10-15 layer thicknesses downstream of the obstacle. A new current head continued downstream with a speed roughly two-thirds that of the original front. The reflected waves produced by this new gravity current front striking the channel end wall inundated the hydraulic jump. This led to a continually deepening layer with no dissipative mixing or turbulent activity, just as in the case after reflection of the unobstructed flow. The mixing of the current in the jump at the obstacle, and the reduction in current front speed downstream of the obstacle, indicated that transversely oriented obstacles can be effective in impeding the spread of gravity currents such as those found

in hallways of burning buildings.

The series of experiments directed at illustrating the gravity current frontal region characteristics also proved informative. Video recordings of the plan view of the leading edge of a current revealed a lobe and cleft structure as reported by Simpson (1972). The mean lobe size was roughly one-half the head height for flows with head Reynolds numbers of about 1000. This agrees well with Simpson's empirical relation for the ratio of lobe size to head height of:

$$\frac{\overline{b}}{h_{head}} = 7.4\, Re^{-.39\pm.02}.$$

As was stated earlier, gravity current head entrainment is significantly influenced by the ingress of ambient fluid into the head region. The overriding of ambient fluid at the floor by a dense undercurrent produces a gravitational instability in the head, leading to substantial mixing activity in high Reynolds number flows. Simpson (1972) was able to visualize this overridden fluid by means of fluorescent dye in the ambient fluid with slit-light illumination in the vertical streamwise plane. In these experiments, visual observations were made of the current head features with this instability suppressed. The intrusion of a gravity current underflow into a channel containing a dense lower layer of depth less than a quarter of the current layer depth produced a flow with no turbulent region at the current front, but rather a current head with a smooth interface between it and the ambient fluid. For high enough Reynolds numbers, evidence of Kelvin-Helmholtz instabilites at the top of the head can be seen. Quantitative determination of the nominal dense layer depth required for this phenomenon to occur was not performed, but it is hypothesized that layers shallower than the current head nose height that would exist for a flow without the dense layer present would not inhibit the unstable overriding of ambient fluid by the current

front. This nose height has been measured by Simpson as a function of Re to be:

$$\frac{h_{nose}}{h_{head}} = .61\, Re^{-.23\pm.01},$$

where h_{head} is the current head height. These results support the conclusion that the unstable overriding of ambient fluid is the principal mechanism for interfluid mixing in low Reynolds number(1000) gravity currents.

Thus, we have examined the basic features of adiabatic gravity current flows, including their dependence on the flow parameters, Δ and Q. Although the shape and spreading rate of the flows were observed to vary with Reynolds number, the streamwise position of transition from the constant velocity flow regime to a decelerating, viscous dominated flow was seen to depend only on the thickness, h, of the current. The next chapter will consider the mechanism of heat transfer as a principal factor in another type of gravity current flow, in which the buoyant driving forces are thermally induced and convective heat exchange occurs between the current fluids and their boundaries.

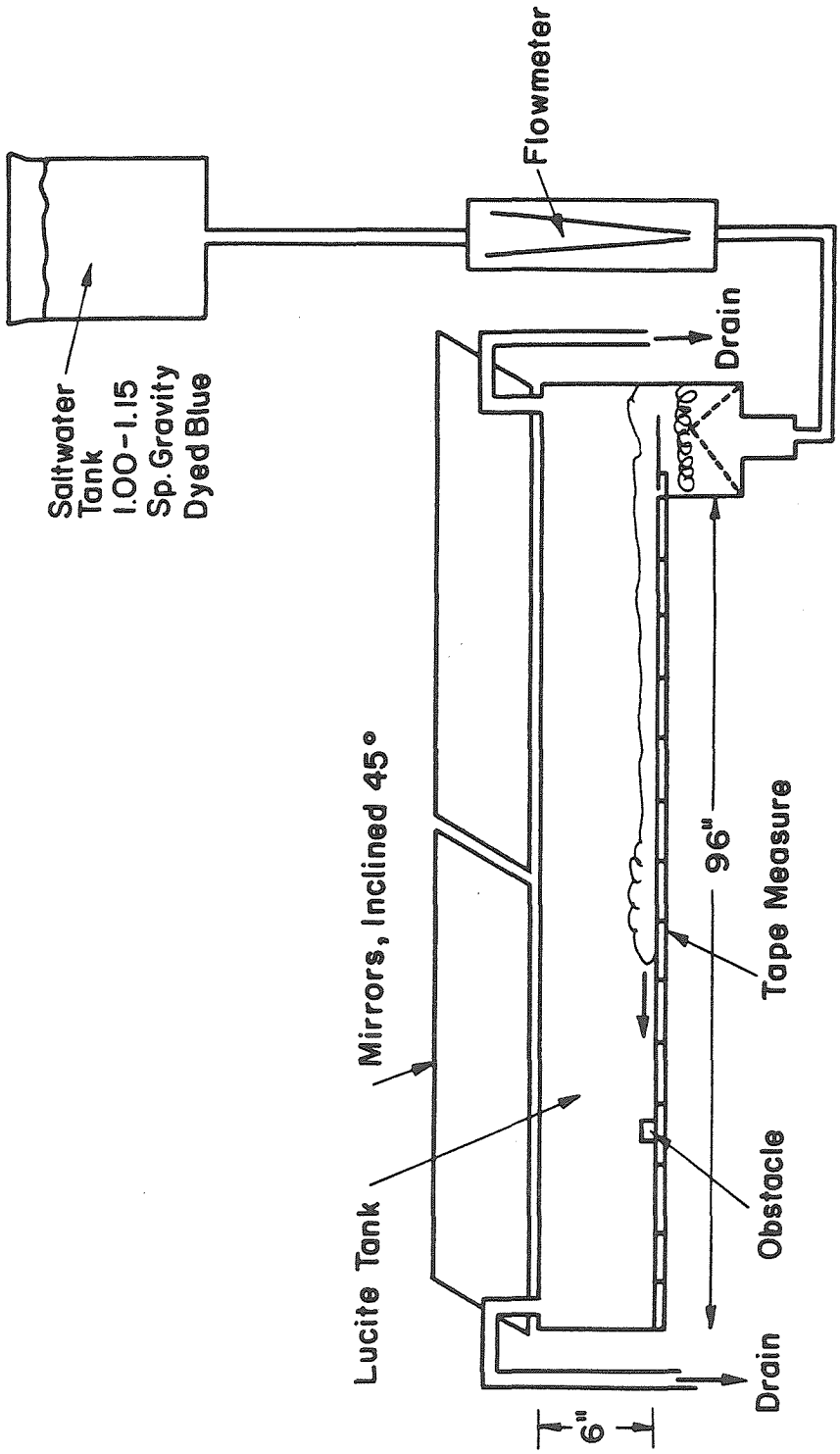

Figure 2.1 Schematic of salt water gravity current experimental apparatus.

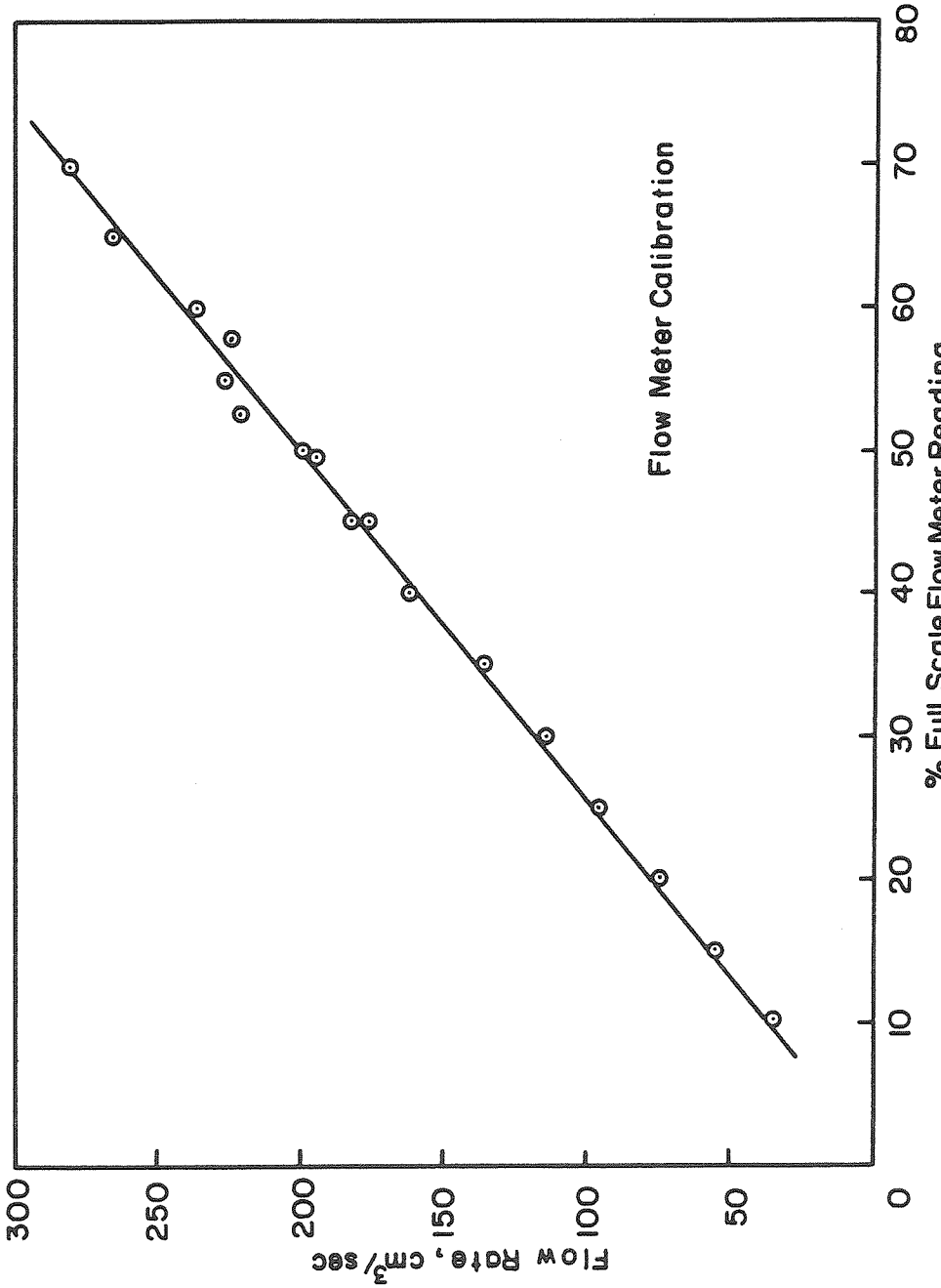

Figure 2.2 Rotameter calibration curve, flow rate versus % full scale reading.

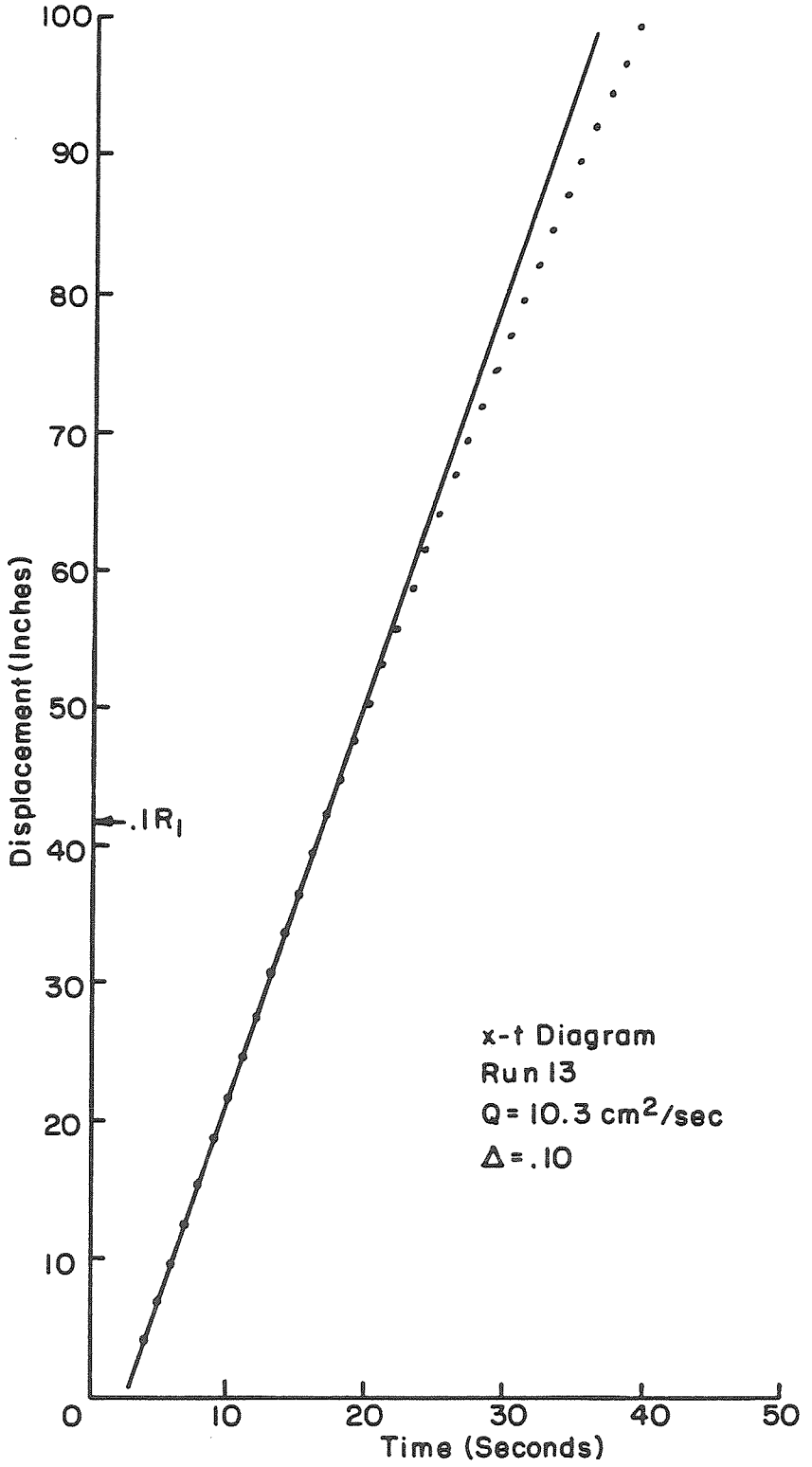

Figure 2.3 Gravity current front position versus time for flow with Δ=.10 and $Q = 10.3\,\mathrm{cm}^2/\mathrm{sec}$.

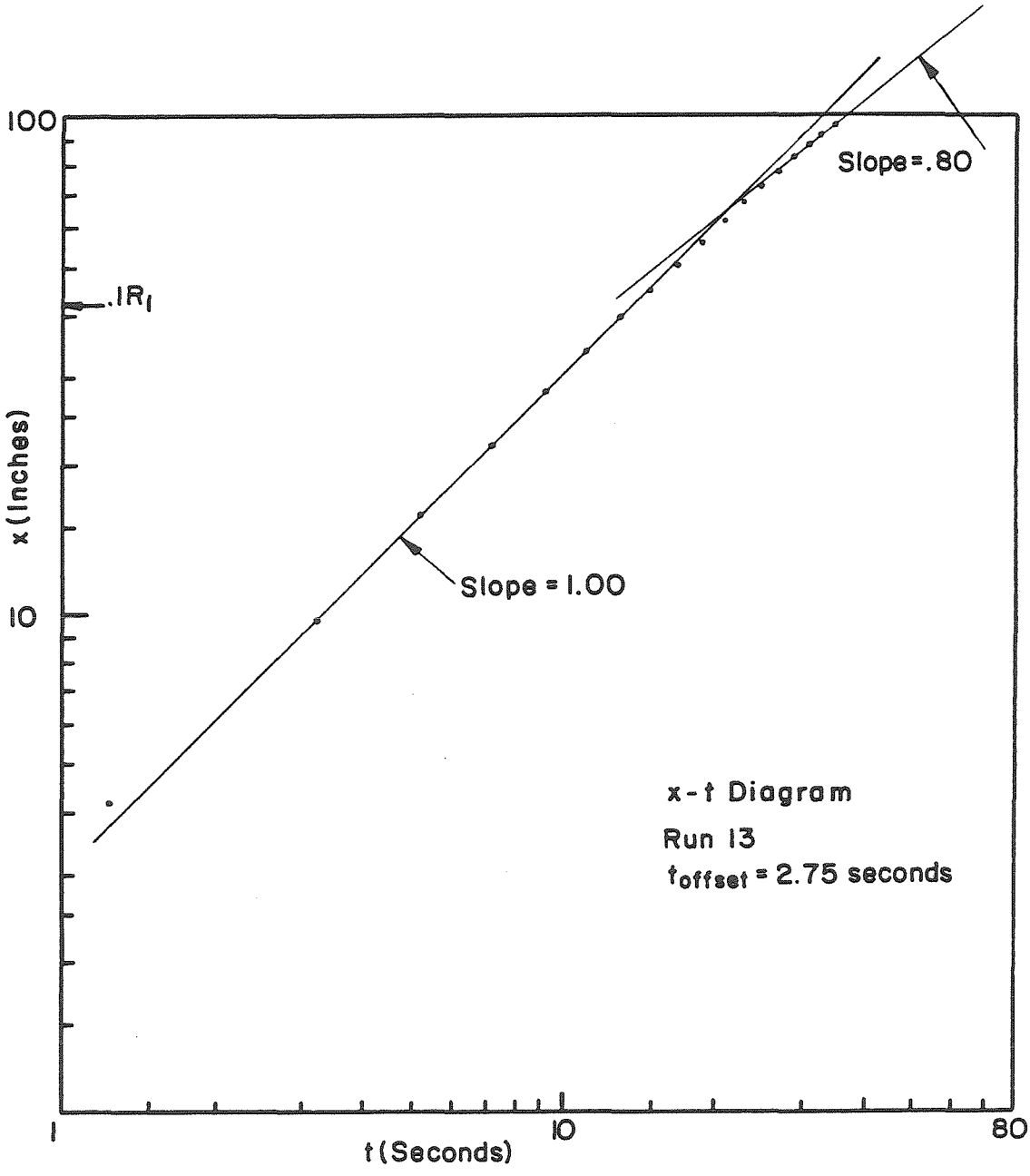

Figure 2.4 Gravity current front position versus time with time offset correction, Δ=.10 and $Q = 10.3\,\mathrm{cm}^2/\mathrm{sec}$.

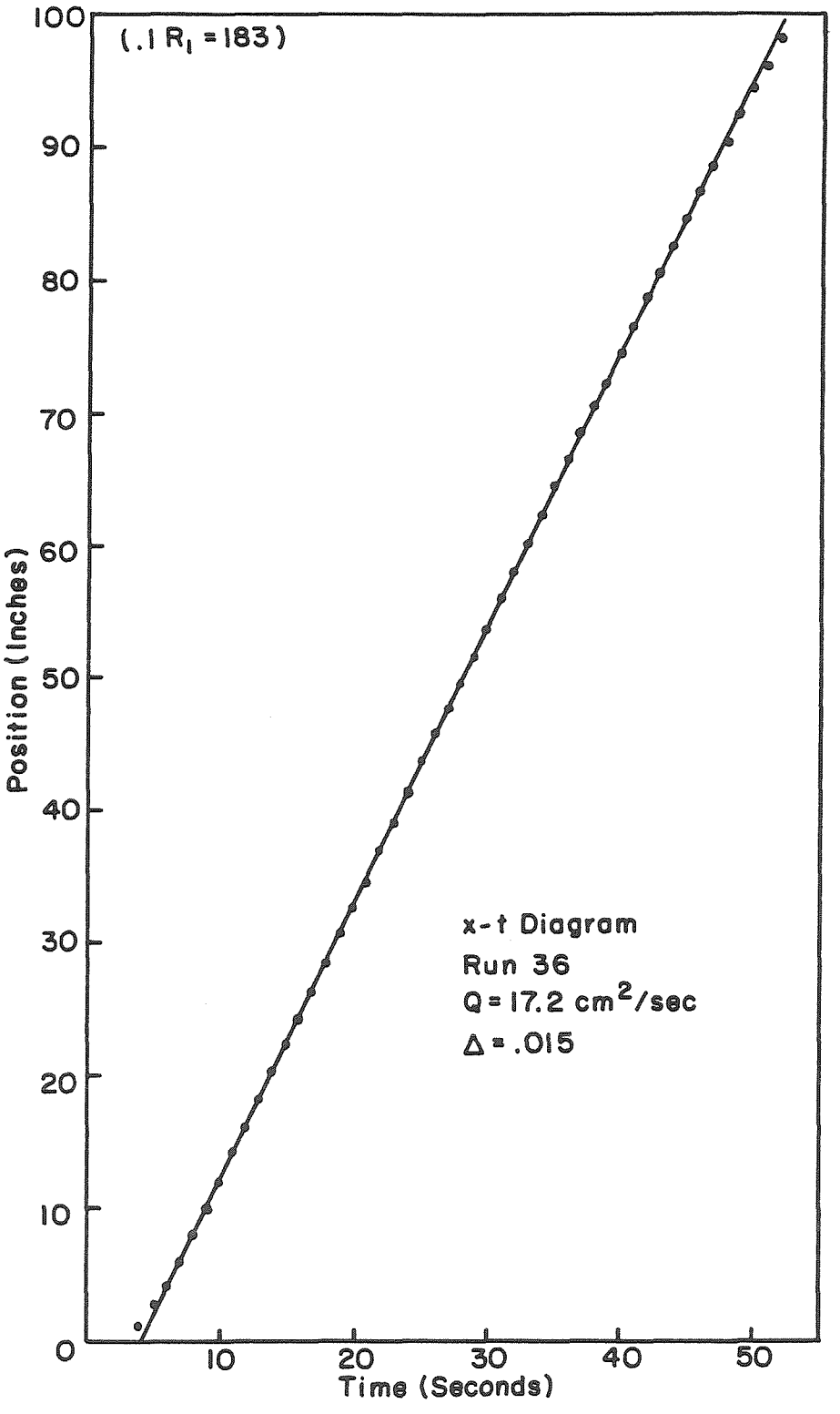

Figure 2.5 Gravity current front position versus time for flow with Δ=.015 and $Q = 17.2\,\mathrm{cm}^2/\mathrm{sec}$.

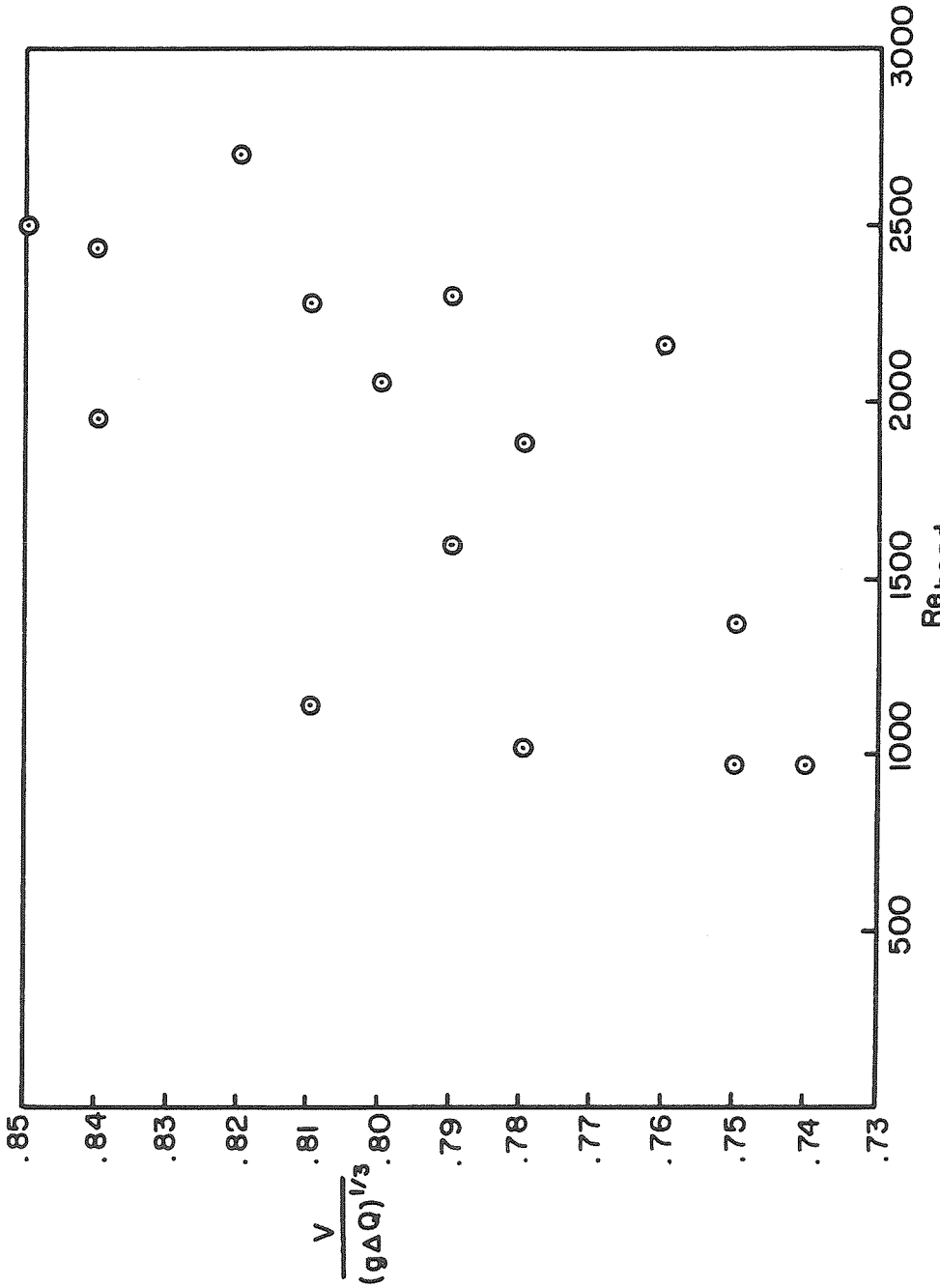

Figure 2.6 The variation of $C = \frac{V}{(g\Delta Q)^{1/3}}$ as a function of Reynolds number, $Re = \frac{Vh}{\nu}$.

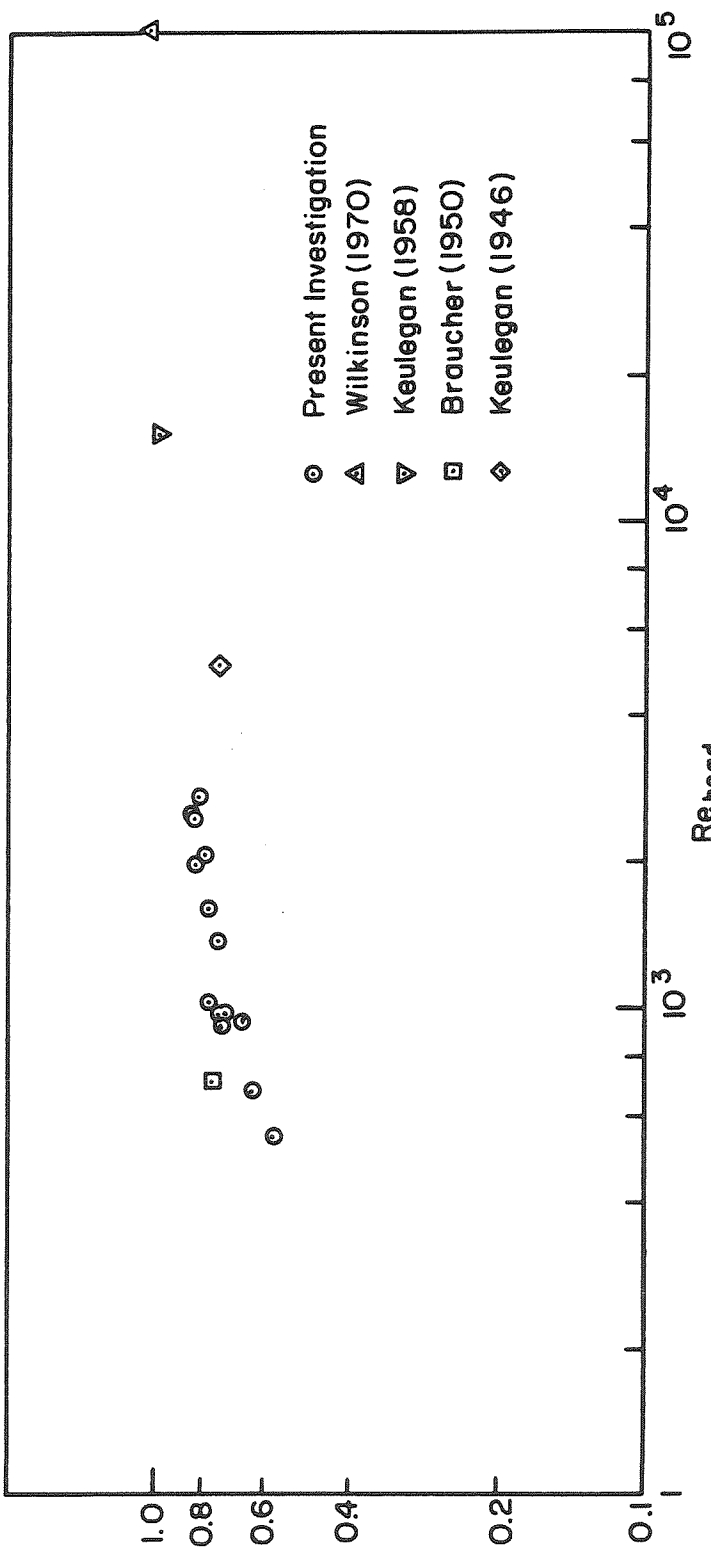

Figure 2.7 The variation of $C = \frac{V}{(g\Delta Q)^{1/3}}$ as a function of Reynolds number, $Re = \frac{Vh}{\nu}$, including data from previous investigations.

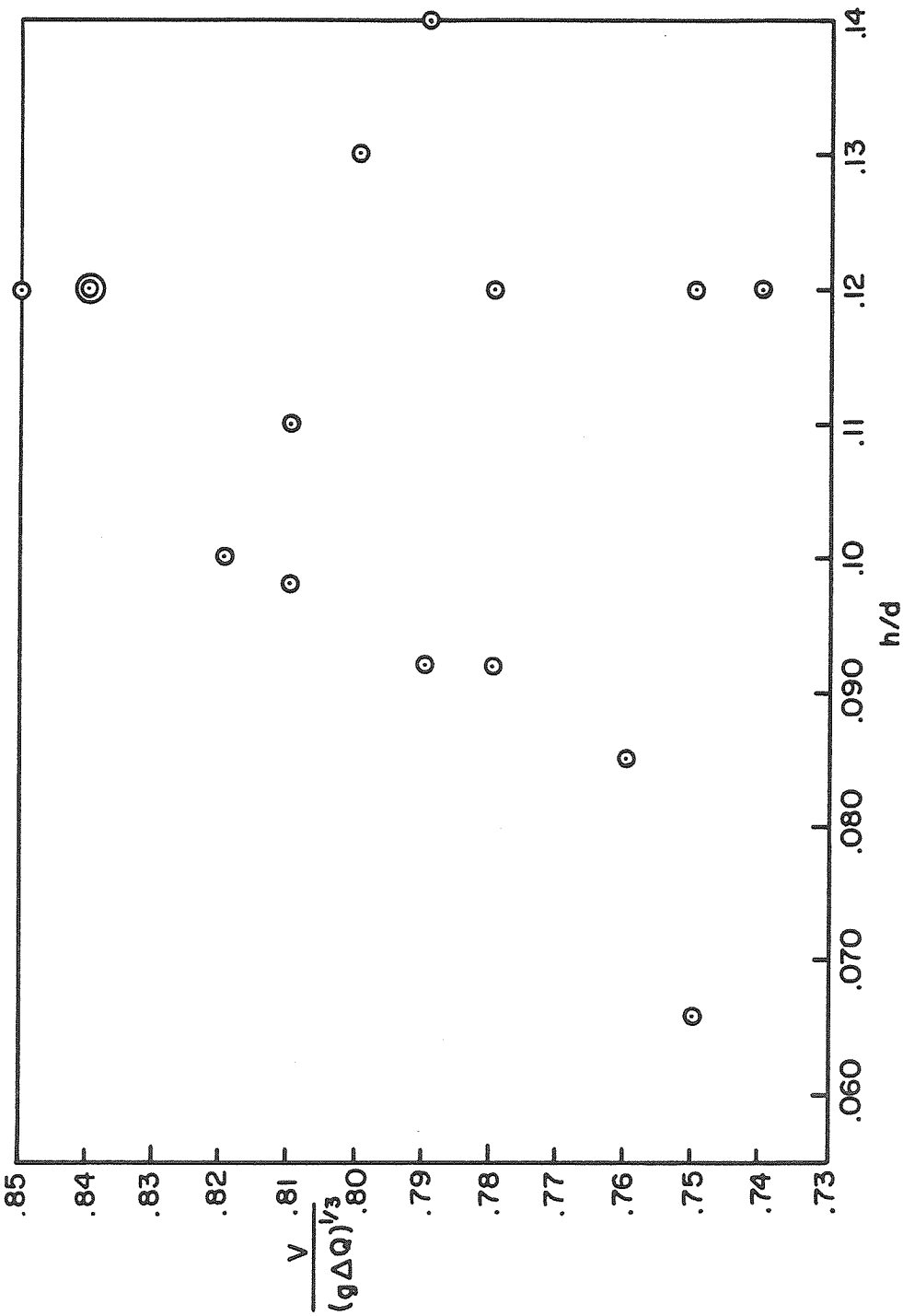

Figure 2.8 The variation of $C = \frac{V}{(g\Delta Q)^{1/3}}$ as a function of $\frac{h}{d}$, the fraction of the duct height occupied by the current layer.

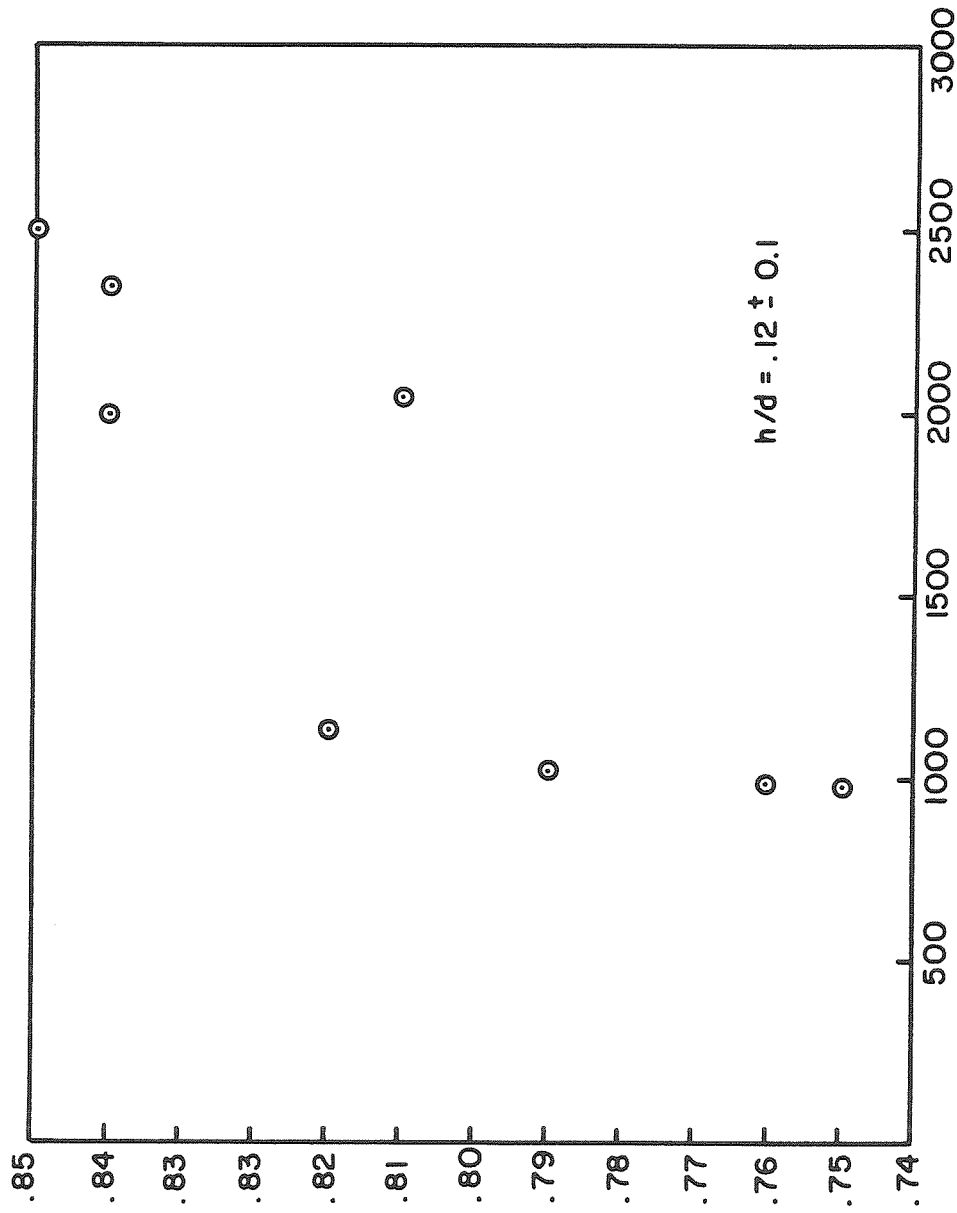

Figure 2.9 The variation of $C = \frac{V}{(g\Delta Q)^{1/3}}$ as a function of Reynolds number, $Re = \frac{Vh}{\nu}$, for fixed $\frac{h}{d}$.

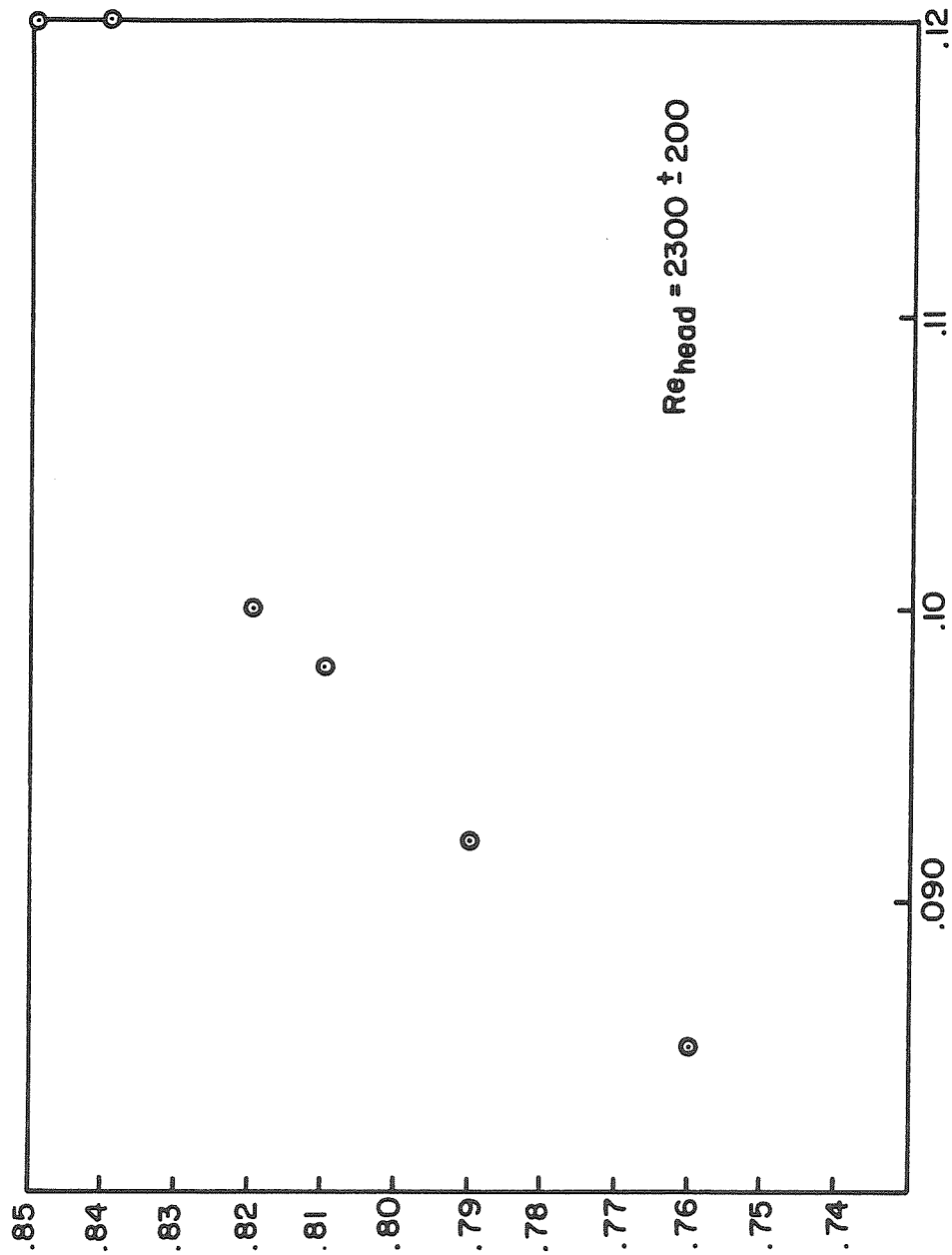

Figure 2.10 The variation of $C = \frac{V}{(g\Delta Q)^{1/5}}$ as a function of $\frac{h}{d}$ for fixed Reynolds number, $Re = \frac{Vh}{\nu}$, of about 2300.

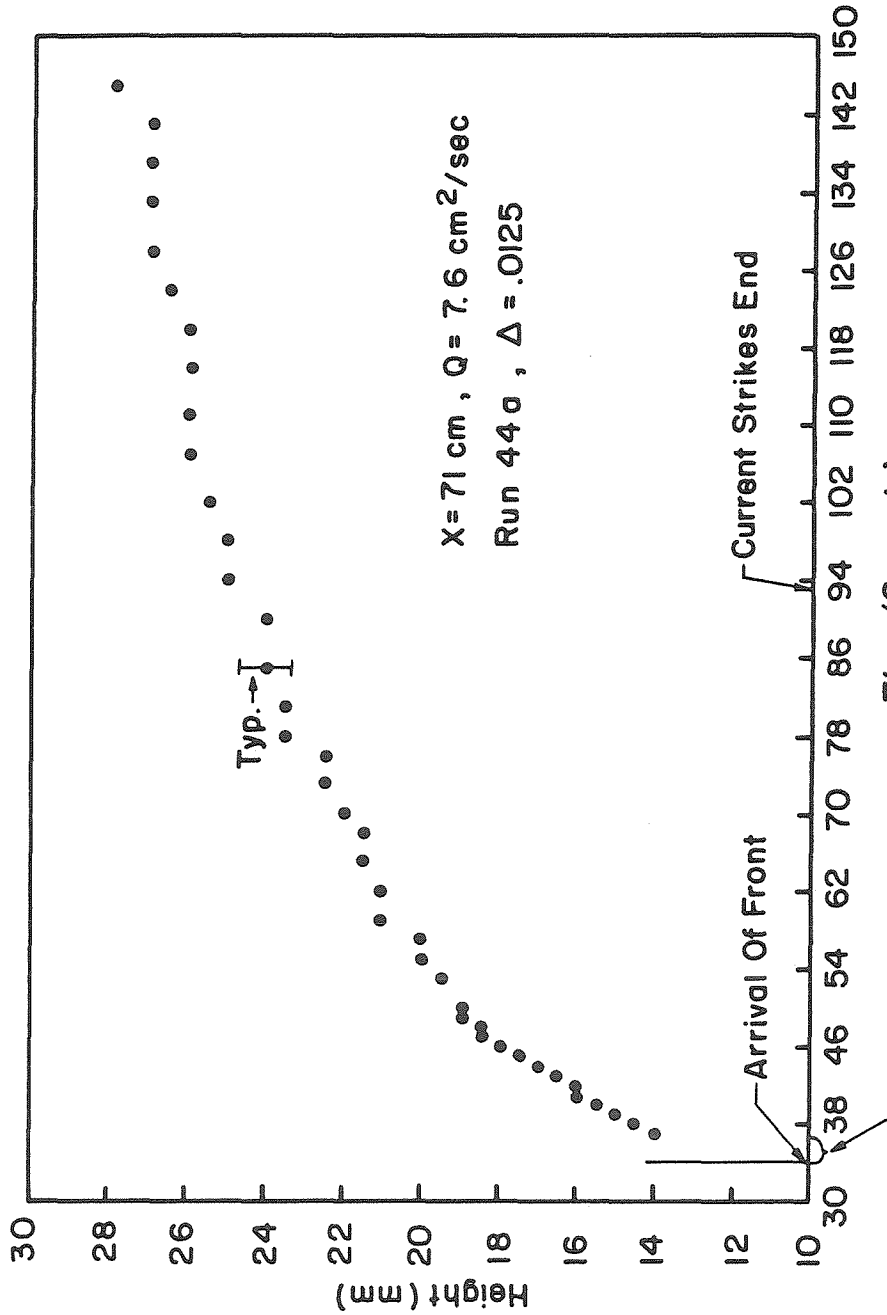

Figure 2.11 Current layer thickness as a function of time at fixed streamwise position $x = 71$ cm, for flow with $\Delta = .0125$ and $Q = 7.6\,\mathrm{cm}^2/\mathrm{sec}$.

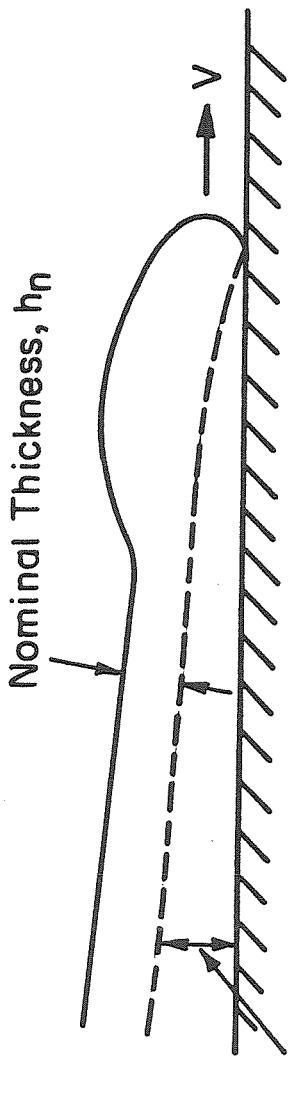

Figure 2.12 Viscous current layer model diagram.

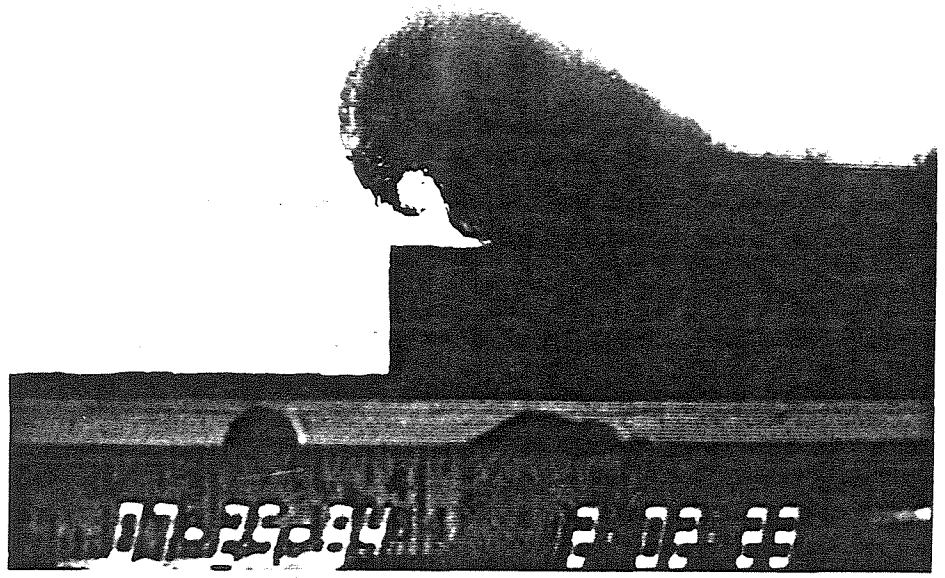

(a)

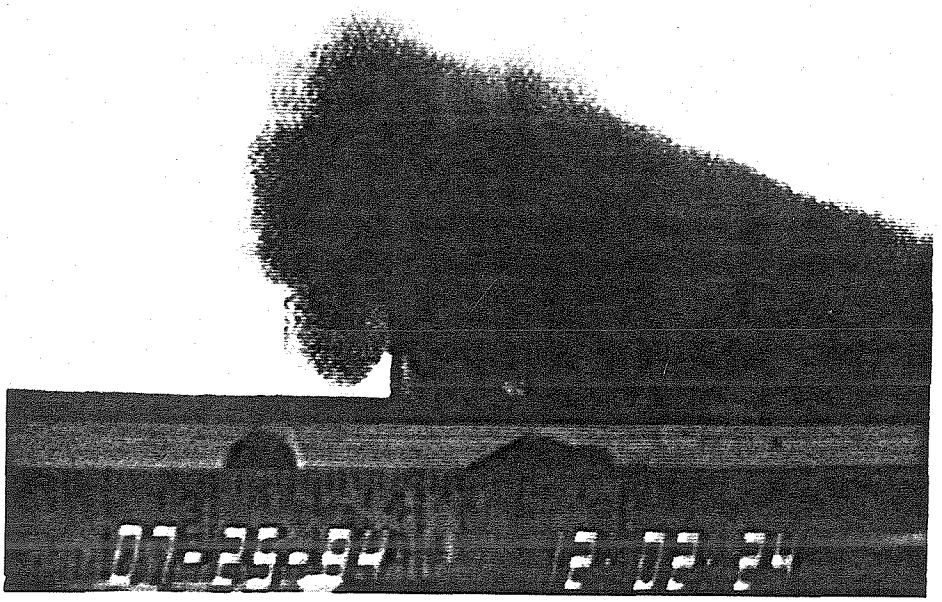

(b)

Figure 2.13 The encounter of a transversely oriented obstacle by a gravity current. Image (b) taken 1 second after (a).

Chapter 3

Experimental Study of Gravity Currents Affected by Heat Transfer

3.1 General Comments

This chapter is concerned with the quantitative investigation of gravity current flows influenced by convective heat transfer to their surroundings. These effects are most pronounced when they occur in a fluid flow in which the specific volume and density of the constituents vary strongly with temperature. The relative magnitudes of diffusion of momentum, heat, and species of the laboratory flows used in this study should resemble those of applications of greatest relevance to this work, such as gravity current flows in building hallways which were discussed in section 1.3. Consequently, the media chosen for this segment of experimental study are in the gaseous state, namely air, nitrogen, and helium. This choice requires the scale of the apparatus to be several times that used in the saltwater/water experiments, as previously mentioned.

In flows such as the building fire example, the unsteady, transient flow field is often of primary significance. The development of the hot, toxic current affects occupant safety long before a deep layer configuration is reached, since the deep layer would result only after the current has traversed the entire hallway. In terms of the heat transfer mechanism at the hallway ceiling, the wall temperature can be considered to be effectively constant because the surface temperature will not rise significantly in comparison to the overheat of the local free-stream gas during this transient phase. Thus, the reduction in local wall heat transfer due to ceiling temperature rise will not be considered important here, and hence a

ceiling of sufficiently high thermal conductivity and heat capacity to maintain such a constant wall temperature is used in the course of the heat transferring current experiments.

The antithesis of this asymptotic condition of maximum heat transfer is the case for which the time scales of interest are large in comparison to the time required for the ceiling to reach a temperature close to that of the current free stream. This limit is essentially the adiabatic case studied in chapter 2. An adiabatic case will also be examined in this section which will allow examination of the effects on the flow of the lower Prandtl and Schmidt numbers of the gaseous flows as compared to those of the liquid flows used earlier. In addition, this adiabatic case will involve non-thermally induced density difference ratios much larger than those achievable in the saline current flows. These same large density ratios are used in the heat transferring flows, and are limited in magnitude only by the ability of the facility's component materials to withstand the overheat of the current fluid needed to produce the high values of Δ. In practice, this allows for Δ to be as high as about 0.5.

Thus, heat transfer effects on the unsteady properties of two-dimensional gravity currents flowing in a channel are examined in this chapter, with particular attention given to the effects on current front propagation speed and layer geometry. A detailed description of the apparatus constructed for this phase of experimentation appears in the following section.

3.2 Experimental Apparatus Description

The experiments involving gaseous gravity currents are carried out in a horizontal duct 7.3 meters in length with a .5 meter square cross-section. A wood floor supports tempered glass side walls of 3/16-inch thickness, and is carried by cross

members of an angle-iron structure supporting the entire duct. This structure also supports the .5 inch thick aluminum ceiling of the channel from cross members located about .6 meters above the channel floor. The ceiling supports can be adjusted to level the ceiling, as can the legs of the support structure. Leveling of the ceiling was accomplished to within a tolerance of 1/20 of a degree of slope. The inlet end of the channel has a rectangular opening through which the heated gas flow is supplied, with the remaining area below the inlet blocked. The normally open downstream end of the duct can be partially closed to allow for reflection of the buoyant layer. The downstream end of the duct serves as the displaced ambient fluid exit for all of the experiments performed in this facility. Figure 3.1 illustrates the important features of the apparatus.

The buoyant gravity current fluid is generated by passing high pressure gas (nitrogen,helium, or air) from a large cylinder through a choked nozzle flow meter and into an upright enclosure of $2' \times 2' \times 5'$ dimensions containing three nickel-chromium perforated-band heating elements enclosed in a shroud. Each heating element is supplied by a 240 volt variac and can dissipate 2.3 kilowatts. The choked nozzle flow meter consists of a brass block with inlet and outlet fittings on its ends, and contains a contraction nozzle insert which accelerates the flow sufficiently to produced a choked condition at its throat. Several different nozzles can be used to provide for a wide range of flow rates, but typically a nozzle of 44 to 1 area contraction ratio is used. A pressure port upstream of the throat permits total pressure measurement by a 0-250 psia pressure transducer, while a port downstream of the throat is used to verify that a sufficient pressure ratio across the contraction exists to support sonic flow in the throat. This sonic condition allows for a flow rate through the flow meter independent of downstream conditions, and requires for mass flux measurement that only one

pressure be monitored during the course of a run.

In addition to the heating elements, the hot gas supply contains fiberglass board insulation of 2-inch thickness on its interior walls, and stainless steel wool sandwiched between two screens three inches apart which divide the enclosure approximately in half. A small blower and an insulated duct joining these two halves of the enclosure allows for recirculation of the gas between the lower section, which contains the heaters, and the upper section. This recirculation facilitates the warm up of the hot gas supply prior to the performance of an experiment. The upper section of the hot gas supply has provision for varying the exit slot height up to a value of about 15 cm, and the exit has a vertically sliding door with a micro-switch which is triggered upon admittance of the gravity current into the duct by the opening of the door. This switch is connected to an interface board in a microcomputer used to monitor the experiment. The door is constructed from 1/2-inch thick wood, which effectively insulates the ambient air in the channel from the heated gas in the supply prior to the door's opening. Thermocouples are mounted at various locations inside the hot gas supply to aid in monitoring its function, particularly during its warming-up period.

Thermocouples are also employed throughout the duct for ceiling surface and gravity current temperature measurement. The ceiling has twelve streamwise instrument stations which are located at two foot intervals, beginning one foot downstream of the channel inlet, at which aluminum plugs carrying instrumentation can be inserted. These stations are referred to as X=1 through X=12, with X=1 being the position closest to the inlet end of the channel. Three spanwise ports are available every other streamwise position, beginning with the first, with the centerline location denoted by Z=0, while the stations 12.5 cm away on each spanwise side of the center station are specified by Z=1 and by Z=-1.

Chromel-alumel thermocouples of 12.7 micron diameter, and consequently of fast time response, can be positioned along the duct to measure the progress of the head of the current down the duct. With a frequency response of roughly 100 Hz, these fine-gauge thermocouples allow resolution of the current frontal position to within .5 cm for a frontal velocity of .5 m/sec. For support, these very fragile fine-gauge thermocouple junctions are spot welded across leads protruding from stainless-steel sheathed 1/16 inch O.D. thermocouples. A rake of six such thermocouples can determine the temperature profile at a particular location in the duct as the current progresses. The distance below the ceiling that a probe is located is referred to as the probe's Y position, and is measured in centimeters. The rake allows for thermocouples to be located at Y positions covering the range .5 cm to 15 cm. On the surface of the aluminum plugs are mounted thin-foil thermocouples to verify the isothermal wall condition of the ceiling. Amplification of the fine-gauge and thin-foil chromel-alumel thermocouple outputs required construction of amplifiers employing AD 595CD thermocouple amplifiers with cold junction compensation. These amplifiers also have light emitting diodes that switch on when an open circuit at the input of an amplifier occurs, since the fine-gauge thermocouples break frequently and are barely visible to the naked eye. Repair of these junctions requires use of a microscope and micrometer positioners for spot welding.

Also cemented to the surface of these plugs are heat flux gauges comprised of 40 pairs of chromel-alumel junctions across a .006 inch substrate covering an area of about 1cm x 1.5cm. Numerous pairs of junctions are required to increase the sensitivity of the heat flux gauges, although this is at the expense of spatial resolution. The low sensitivity of each junction pair is a result of the small thickness of the substrate, across which the thermocouples are mounted,

necessary to ensure low heat capacity of the gauge and a correspondingly high frequency response. The 1/e rise-time response of these gauges is about .060 sec, while amplifiers of gain up to 10,000 located above the gauges were designed and constructed to amplify their relatively low outputs to appropriate levels for analog to digital conversion, which in this case requires voltages in the 0 to 10 volt range. The close proximity of the amplifiers to the gauges serves to reduce line noise pick-up between the gauges and their amplifier inputs, as the gauges are located at relatively large distances (10 to 30 feet) from the analog to digital converter. These amplifiers consist of an AD 524B instumentation amp providing gain of 1000, with an OP 27C op-amp producing another factor of 10 gain (which can be switched to 2.5 for higher level heat flux measurements, such as those encountered at the upstream end of the ceiling), and a low-pass filter. A schematic of the high-gain amplifier circuitry appears in appendix A, and figure 3.2 gives two views of a typical instrument-bearing plug.

Typically, outputs from some of the twelve thermocouple amplifiers, six high-gain heat flux gauge amplifiers, and the pressure transducer monitoring the choked nozzle flow meter are converted to digital signals via a sixteen channel 40 kHz Tecmar S-100 A/D converter with 12 bit resolution, sampling up to 1000 two-byte words per second per channel. This data acquisition system consists of a timer/counter and controller card installed into a Zenith Z-120 S-100 microcomputer, which is connected to an external board containing the A/D module, buffers, and multiplexers. This remote location of the converter allows for reduced analog signal line length from the instrumentation amplifiers, thus reducing system noise. Data storage and reduction is also accomplished with the use of the Zenith Z-120 microcomputer.

The low flow velocities, ranging from 0 to about .5 m/sec, together with the

large transient temperature gradients and the unsteady nature of the flow field, make conventional velocity measurement techniques impractical. Consequently, a smoke pulse velocity probe was developed to determine velocity profiles in the flow. This smoke pulse probe is illustrated in figure 3.3, and consists of a series of six .003 inch diameter tungsten wires 16 cm in length extending down from the ceiling, with .5 cm horizontal spacing between them. The wires and their support rod pass through insulators in their aluminum plug base, thus comprising six separate electrical current paths. A current pulse of about 2 amps over a 20 millisecond duration is switched through each paraffin-coated wire in successive intervals, causing the wires to boil off a paraffin smoke plume. These convecting smoke plumes are photographed by a 35 mm camera. Velocity profiles are inferred from the paths the plumes traverse over known time intervals. Six wires are required since only one plume is produced per wax-coated wire, and several plumes are required in succession to visualize unsteady features of the flow as it passes by. This wax coating is accomplished by passing the wires through molten paraffin. Timing and control of the smoke pulse probe operation and photography are handled with the use of an Intel 8085 microprocessor interfaced with an 8254 programmable timer/counter whose layout can be seen in appendix B, which also includes the assembler language control program. A schematic of this technique is given in figure 3.4.

Another smoke pulse wire probe is used for generating horizontal plumes in the spanwise direction in the current boundary layer. It consists of a 16 cm long, .003-inch diameter tungsten wire held parallel to the ceiling, which can be positioned at distances as great as 10 cm below the ceiling. Photography of the plumes generated from this probe is performed to study the boundary layer structure of the current.

Shadowgraph images of the flow are also photographed using this microprocessor system. A frame supporting stretched vellum paper is mounted approximately 8 feet from the side-wall glass, while an arc lamp located over 40 feet from the channel test section provides the effectively parallel light required for generation of the shadowgraph. This light source projects its beam along a path parallel to the channel length, and the beam is reflected through a 90° angle by a large mirror located behind the channel at the test section position. The image projected on the vellum screen is photographed by a timer controlled camera located about 6 feet behind the screen.

3.3 Experimental Procedure

In order to compute the parameters Δ and Q defining each particular experimental run, the current fluid temperature at the exit of the hot gas supply was measured, and the mass flux issuing from the supply was also measured. Consequently, two of the sixteen available data acquisition channels were dedicated to the amplified output of the thermocouple located at the exit slot, and to the flow meter's pressure transducer output. The ambient temperature in the duct was recorded by all of the downstream thermocouples prior to the arrival of the current front at their respective locations. Depending on the duration of the time period of interest for a particular run, the sampling rate of the analog to digital converter was adjusted via a software delay loop in the assembler language code controlling the converter, as a total of 256 kilobytes of data were collected for each run, with one data word representing two bytes. Even for the longest data sampling periods (about one minute), this permitted adequate sampling rates of the instruments monitoring the run. This method was chosen since, although 35 different runs with many different sampling times were performed, all of the data were consequently organized in easily manageable sets of four 64 kilobyte

data blocks.

A nominal condition for which the greatest number of measurements were made was defined using the maximum allowable temperature difference of 250° C between the current source fluid and ambient air temperatures as dictated by the materials used in construction of the facility, and a mass flow rate of 9.3 gram/second of the source fluid, a median value in terms of the range obtainable. These conditions correspond to a value Δ of .46, and a value Q of about $300\,cm^2/sec$, or $.030\,m^2/sec$.

In addition to the pressure measurement upstream of the flow meter nozzle contraction, accurate source fluid mass flux determination also required that the heat input to the hot gas supply was such that thermal equilibrium of the supply existed, i.e., the heat input balanced the enthalpy flux at the exit of the supply together with the heat lost to the surroundings by the hot gas supply. This ensured that the mass flow rate at the hot gas supply exit was equal to that measured by the flow meter at its cold inlet. The heat lost to the surroundings by the supply at a given temperature was determined by measurement of the heat input necessary to maintain the supply at the given constant temperature under conditions of no flow and with its exit blocked off. Input heating rates were determined from voltage input levels to the heating elements of known resistance. Being of nickel-chromium construction, the heating elements' resistances were essentially independent of temperature. An input heating of 3.3 kilowatts was required for the nominal case 2.2 kw enthalpy flux of the hot gas supply discharge.

The high heat capacity of the hot gas supply necessitated a long warm-up period prior to the performance of an experiment. To expedite this procedure and to achieve more uniformity of temperature within the supply, the recirculation fan was operated until the uppermost interior thermocouple of the supply

indicated a temperature about 10° C above the temperature required for the subsequent run. When this condition was reached, the fan was switched off and the temperature allowed to fall to the required level, as the settings of the variacs were simultaneously reduced from their warm-up levels of about 75% (of 240 volts a.c.) to the levels consistent with the enthalpy flux of the ensuing run's flow into the channel. This was about 70% for the nominal case of 250° C channel inlet temperature difference and 9.3 gram/second mass discharge rate. This case required about one hour for the warm-up procedure. During this period, the heat flux gauge amplifiers were allowed to equilibrate and their outputs were zeroed by use of trim potentiometers.

After preparation for an experiment as described above, the microcomputer executed the data acquisition program which monitored the I/O port connected to the channel door micro-switch, and called the assembler subroutine activating the A/D converter upon the door's opening. A ball valve in the high pressure gas supply line was opened together with the door to initiate the flow. Data was stored in the RAM of the computer and written to floppy disk following the completion of the run.

In order for gravity current layer local mass flux calculations to be made at various downstream X locations, local temperature and velocity profile measurements were made. Since it was observed that for all flows tested, local temperature measurements displayed very small increases with time once the current head passed the local measuring station, temperature profile data from the thermocouple rake was averaged over several seconds. These profiles were then used to determine the local density profiles, which together with velocity profiles inferred from smoke pulse photographs, determined the local mass flux profiles, which were integrated across the layer to give local mass fluxes. The

gravity current layer thickness was defined from local temperature profiles as the Y-axis intercept value of the line of minimum slope tangent to the profile in the shear-layer portion of the profile.

From experiment, it was determined that the transversely convecting smoke plumes, generated by the pulse wire probe used for velocity profile measurements, experienced free convection in the vertical direction. This buoyant convective velocity was measured to be approximatetly 5 cm/sec in a room temperature air environment. Stroboscopic photography of the plumes generated from the probe in a horizontal orientation and encased in a glass sided box was used for this purpose. It is believed that the temperature of the smoke was sufficiently high to warrant use of this approximate value of free convection velocity (which was shown to be fairly constant) throughout the temperature profile, and stroboscopic photography of plumes generated in the current layer supported this assumption. Measurements from the smoke plume photographs taken during the course of a run gave values of downstream smoke displacement versus Y position. The relationship between the observed plume shape, $x(y)$, and the actual velocity profile, $u(y)$, can be expressed in the form:

$$x(y) = \int_0^{\triangle t} u\left(y + (t - \triangle t)v_c\right) dt\,,$$

where v_c is the free convection velocity of the smoke, and $\triangle t$ is the plume convection time. For cases where $|v_c|$ is small compared to $|u|$ this correction may be neglected.

This time of flight of the smoke plume, $\triangle t$, required for velocity determination, consisted of three parts. The first was comprised of the difference between the wire current pulse duration and the delay between wire current pulse inception and smoke plume generation. This delay was measured by reducing the

length of the current pulse until no plume was created, and was found to be about 8 milliseconds. The current pulse duration was 20 msec. The second part of the total flight time consisted of a variable delay which commenced immediately after the end of the current pulse. This delay was created by a machine language software countdown loop of the 8085 microprocessor system controlling the smoke pulse photography. The third component of the flight time interval was the inherent time lag between the switching on of the 35 mm camera and flash generation. This was measured to be 210 msec by use of a photodetector and oscilloscope. Since this last component was relatively long, for shorter times of flight triggering of the camera was sometimes initiated before switching on of the wire current pulse.

An overall heat balance for the gravity current/channel ceiling system was performed for the nominal case conditions which considered input enthalpy flux, local current enthalpy flux, and heat transfer to the surroundings. For determination of local enthalpy fluxes of the layer, the local Y-distributions of enthalpy flux at two different X positions were measured in a manner analogous to that used for local mass flux profile measurements. The profiles were again integrated across the layer thickness to obtain the value of layer enthalpy flux at given downstream positions.

For the investigation of heat transfer effects on the spreading rate and layer thickness of thermally induced gravity current flow, many different runs with initial current overheats ranging from 17° C to 250° C and initial mass fluxes of 3 gm/sec to 10 gm/sec, were performed. These parameters allowed for head thickness Reynolds numbers of up to about 5000 and Reynolds numbers based on downstream position of up to 10^5 to be examined. Although the inertial-viscous transition characteristics observed for the adiabatic current case are at

best roughly applicable to heat transferring currents, the nominal conditions represent a value of $.1R_1$ of about 6 meters, or nearly the length of the channel. The inlet Reynolds number based on head thickness for the nominal case, using the film temperature, $T_f = \frac{T_{max}+T_{wall}}{2}$, for the evaluation of kinematic viscosity (and all other fluid properties), was about 4000. Fractional heights of the channel occupied by the current layer were between .1 and .2 .

Several runs using the same initial values of overheat and mass flux were performed as a check on the reproducibility of conditions achievable by the facility. Since there were more possible measuring stations than instruments and data acquisition channels available, the complete mapping of a given flow field required many runs to be performed with the same parameter values but with different instrument configurations. Consequently, reproducibilty was very important, and for runs with the same initial conditions, at least one redundant measurement between successive iterations was performed as a continuing check on the similarity of conditions for each of the trials.

In addition to the thermally induced gravity current quantitative study described above, measurements were also made of the current front spreading rates for gaseous mixture flows with density differences induced by the molecular weight differences of their constituent species. A mixture of helium and nitrogen was used as the source fluid for such flows, with a concentration of 50% by volume of helium at room temperature producing a value Δ equivalent to that of the heated flow case. The value for the gas constant γ in the expression for sonic flow mass flux, $\dot{m}$, through the flow meter of throat area A:

$$\dot{m} = \frac{P_t}{\sqrt{R\,T_t}} A\sqrt{\gamma}\left(1+\frac{\gamma-1}{2}\right)^{\frac{\gamma+1}{2-2\gamma}} \tag{3.3.1}$$

where P_t is the total pressure upstream of the throat, T_t the total tempera-

ture, and R the universal gas constant, was calculated for the mixture using the following expression:

$$\gamma_{mix} = \gamma_{air} \left(\frac{1 + \left(\frac{K_{He}}{1-K_{He}}\right)\left(\frac{C_{P_{He}}}{C_{P_{air}}}\right)}{1 + \left(\frac{K_{He}}{1-K_{He}}\right)\left(\frac{\gamma_{air}}{\gamma_{He}}\right)\left(\frac{C_{P_{He}}}{C_{P_{air}}}\right)} \right) \tag{3.3.2}$$

where K denotes mass fraction and C_P specific heat of the indicated component species. The upstream pressure, P_t, required to produce a mass flux through the flow meter of the 50% helium mixture equal to that of the nomimal case was 250 psia (200 psia was used for the nominal case). Other densities and flow rates for the current source fluid in this adiabatic case were also used, in all cases reproducing parameters of runs performed in the heat transferring set of experiments. This allowed for comparison of similar flows in which the major difference between them lay in the heat transferring versus adiabatic flow condition, although the presence of helium in the mixture altered its kinematic viscosity and molecular diffusion rate as compared to the values for the heated nitrogen. The bulk kinematic viscosity at room temperature of the 50% helium mixture was calculated, using the empirical relation 3.3.3 for the absolute viscosity of a mixture, from Wilke (1950), to be about 3×10^{-5} m^2/sec, or essentially equal to the value of ν for nitrogen at the nominal condition inlet film temperature of 425° K.

$$\mu_{mix} = \sum_{i=1}^{N} \frac{X_i \mu_i}{\sum_{j=1}^{N} X_j \phi_{ij}} \tag{3.3.3}$$

where

$$\phi_{ij} = \frac{1}{\sqrt{8}} \left(1 + \frac{M_i}{M_j}\right)^{-1/2} \left[1 + \left(\frac{\mu_i}{\mu_j}\right)^{1/2} \left(\frac{M_j}{M_i}\right)^{1/4}\right]^2$$

and X_i is the mole fraction of the i^{th} species, and M_i the molal mass. Hence, the head Reynolds number of this adiabatic flow was comparable to that of the nominal case heat transferring flow.

The procedure for producing these adiabatic gaseous flows included supplying a small amount of overheat to the mixture, which allowed detection of the current front arrival by the downstream thermocouples. This overheat was typically of the order 20° C, which was sufficient for detection of the current front even at locations far downstream, and was low enough to not significantly affect the density of the gas mixture in comparison to the intrinsic density difference of the mixture.

To create the desired mixture composition in the gas supply, a predetermined volume of helium was rapidly injected through a valved port, located on top of the supply, onto the supply of known volume. Displaced gas exited the container through vents at the bottom of the supply. By rapidly injecting the helium (approximately 15 ft^3 through a one-inch diameter tube over a period of about 20 seconds) and running the recirculation fan, thorough mixing of the helium with the air in the supply resulted. After this mixed condition was reached, the gas was introduced into the channel, displaced from the supply by the input of an equivalent mixture of gas through the flow meter and into the gas supply's lower inlet. A gas sample was withdrawn from the exit of the supply during the course of each run by use of an evacuated small gas cylinder connected to a short length of 1/16-inch I.D. brass tube. The tube was moved into the exit slot at the commencement of a run and the bottle valve subsequently opened to capture the flow sample. The composition of the gas sample was later measured by gas chromatography. Four such adiabatic experiments were performed.

Several qualitative experiments were performed on the heat transferring currents, and involved flow visualization through smoke plume generation and shadowgraphy. An attempt at detecting the gravity current reflection from an obstacle blocking the top half of the channel exit through the use of thermocou-

ples located near the channel end was also performed. By generating paraffin smoke plumes from the length of tungsten wire supported horizontally at various distances below the ceiling in an orientation transverse to the flow, natural convective phenomena within the heat transferring current boundary layer were visualized. This experiment was also performed with the adiabatic gaseous flows for comparison purposes. Control of this procedure was also accomplished using the microprocessor/pulse wire probe circuitry. Photographs were taken of the plume after waiting various delay periods following smoke generation to allow the plume time to conform to the local flow field in the boundary layer. Sequences of shadowgraph photos at a fixed streamwise location were taken for observation of the head structure and layer properties of the passing thermal gravity current.

3.4 Experimental Results

In the following section, the results of the experiments performed in the gaseous gravity current facility are presented and examined. The discussion will direct most of its attention to the nominal condition heat transferring flow, with the examination of other flows serving to illustrate the dependence of the basic features demonstrated by the nominal case on flow parameters Q and Δ. Where possible, comparison between the heat transfer case and the adiabatic flows investigated in chapter 2 is performed, and in addition, the relevance of the heat transfer case results to the building fire example is discussed.

3.4.1 Thermal Gravity Current Spreading Rate

As discussed in section 3.3, many runs were necessary to completely study a particular flow field, and hence, reproducibility of conditions by the facility was important. This was achieved to the extent that for the ten nominal condition runs, the source fluid temperature always fell into the range $T = 263°\text{C} \pm 4°\text{C}$,

while the total pressure measured at the flow meter was consistent to within ±1%. Typical outputs versus time from the various thermocouples stationed along the streamwise direction of the channel can be seen in figure 3.5. The uppermost trace represents the time history of the heated nitrogen supply's output temperature. Since the thermocouple employed for this measurement was not of the fine-gauge type used downstream, its relatively slow (about 2 seconds) time constant did not allow the following of the high-frequency temperature fluctuations of the source fluid by the thermocouple, which were measured to be about ±10% of the source fluid overheat by use of a fine-gauge thermocouple. Uniformity of temperature of the supply's output gas proved to be a challenging state to achieve. The pervasive temperature fluctuation frequencies in the range 10-20 Hz, as seen from the traces, were far lower than the Helmholtz resonator frequency of the supply, calculated at approximately 500-700 Hz, and were attributed to temperature inhomogeneities of the supply whose effects on the hot gas temperature could not fully be eliminated through mixing by the recirculation fan. Since the mean temperature at the source varied little with time, and considerable averaging was performed in the data reduction, these fluctuation levels were considered acceptable. For the nominal case flow depicted in figure 3.5, the arrival times of the front at various X locations can be deduced by the abrupt signal increases displayed by the thermocouples located 2.5 cm below the ceiling at the X positions. This figure also reveals the rapid cooling of the layer with its downstream progress, a characteristic further examined in the section discussing heat transfer of the current.

After compiling all of the arrival time data for the nominal case, the mean values of arrival times were plotted with downstream position, and appear as figure 3.6. The straight line of slope 1.0 drawn on the plot illustrates the buoyant-

inertial spreading rate behavior for adiabatic flows, and clearly shows the continually decelerating character of the heat transferring flow. From this x-t data, current frontal velocity as a function of downstream position was calculated, and appears in figure 3.7. This plot shows an asymptotic dependence of V on x, for increasing x, of the form:

$$V \sim x^{-.4}. \tag{3.4.1}$$

In comparison to the results of Schwarz and Cosart (1960) for two-dimensional wall jets, which show velocity dependence on x of the form:

$$V \sim x^{-.5} \text{ (laminar)}$$

$$V \sim x^{-.55} \text{ (turbulent)}, \tag{3.4.2}$$

we see that the gravity current front decreases its velocity with increasing x to a lesser extent. This result can be interpreted by the fact that the thermal gravity current, in addition to its initial momentum flux, convects with it its driving force mechanism of density difference, while the momentum driven wall jet opposes streamwise viscous resisting forces only at the expense of its initial momentum flux. The adiabatic gravity current flow, which completely preserved its density difference while propagating downstream, was seen to decelerate even less than the thermal current, with its frontal velocity dependence on x of the form:

$$V \sim \text{constant},$$

for the inertial-buoyant limiting case, and:

$$V \sim x^{-.25}, \tag{3.4.3}$$

for the viscous-buoyant regime.

This effect that the loss of buoyancy with downstream progress of a flow has on spreading rate can also be seen in the results presented in figure 3.8. In this figure, the results of arrival time versus position, x, from several runs representing the same buoyancy flux, $B = g\,\Delta\,Q$, but which used two different combinations of Δ and Q to obtain the value of B, are plotted. A value of B one-third that of the nominal case was used, but with one case employing the parameters $\Delta = .23$ and $Q = .020\,\mathrm{m}^2/\mathrm{sec}$, and the other, $\Delta = .46$ and $Q = .010\,\mathrm{m}^2/\mathrm{sec}$. As can be seen from the plot, the case with greater initial overheat (higher Δ) proceeded downstream with a front velocity greater than the lower overheat (and higher initial momentum flux) case. Thus, the parameter $B = g\,\Delta\,Q$ does not in itself define the flow field for heat transferring gravity currents, as it does for the adiabatic case, since the buoyancy flux lost through heat transfer strongly depends on the relative contribution overheat makes to this flux as compared to that made by the source flow mass flux.

One other series of experiments performed which dealt with gravity current spreading rates involved the helium-air source fluid adiabatic flows. Runs using this mixture were performed which had the same values of Δ and Q as runs previously performed in the heat transferring current study. The downstream progress of the current front as a function of time for two of the adiabatic gaseous flows, each with different values of Δ and Q, are plotted in figure 3.9. In addition, two heated nitrogen cases are plotted, matching the parameters of the adiabatic cases for comparison purposes. The x-t curves for the flows with $\Delta = .10$ and $Q = .018\,\mathrm{m}^2/\mathrm{sec}$ are similar, with the adiabatic flow exhibiting less deceleration with progress downstream than does the thermal gravity current. This adiabatic flow, however, was not completely free from the effects of heat transfer, as the overheat of 20°C supplied at the source, for thermocouple detec-

tion purposes, contributed a non-negligible fraction of the total density difference of the source fluid. As a result, the helium mixture did lose buoyancy as it progressed downstrean and did not propagate with a nearly constant velocity, as was observed for adiabatic flows in the saltwater current apparatus. The cases with higher Δ and Q in figure 3.9 do illustrate the effect of heat transfer well, since the helium mixture flow's buoyancy was increased less than 10% by the tracer overheat, as compared to almost 50% in the previous example. This adiabatic flow did demonstrate some decrease in velocity beginning approximately 2.5 meters downstream, but this characteristic was consistent with the inertial-viscous transition phenomenon examined in section 2.4.1. This transition point was calculated using the previous results to be about 3 meters for the adiabatic flow of $\Delta = .46$, $Q = .030\,\mathrm{m}^2/\mathrm{sec}$, and head Reynolds number of roughly 4000. In both sets of flows in figure 3.9, the adiabatic and thermal currents initially propagated with similar velocities, but the spreading rate of the heat transferring current decreased more significantly with downstream progress than its adiabatic counterpart.

In terms of the building fire gravity current example, heat transfer has the desirable effect of reducing the spreading rate and overheat of the current. The effect of deepening the layer that heat transfer has, discussed in section 3.4.3, however, may hinder to a greater extent the movement of the occupants through the building due to the opacity of the smoke in the gravity current layer.

3.4.2 Local Layer Velocity Characteristics

In addition to the study of thermal gravity current front velocities, velocity measurements in the flowing layer upstream of the current head were also made and examined. Although the flow field of interest in this investigation is unsteady in nature, over the time period required for the current front to reach the channel

end many flow properties were observed to be essentially steady. This was true for the local layer velocity profile measured by the smoke pulse technique once the current head had passed the particular measuring station. Although a slight thickenning of the profile in the Y dimension was observed with time, no change in the velocity profile maximum was measureable, at least not one of greater than the approximately ±5% resolution of the smoke plume velocity measurement technique.

While previous velocity profile measurements in adiabatic aqueous gravity current layers found profile maximums as high as 1.5 times the front velocity, in the thermal current flows with continually decelerating fronts no such characteristic was observed. Instead, to within the experimental accuracy of the measurements, the current front's velocity as it passed a particular X location was roughly equal to the quasi-steady local layer velocity profile maximum. For shorter downstream distances, a slightly greater profile maximum velocity as compared to current front velocity was observed, although the differences never exceeded about 10% of the front velocity.

A sequence of six smoke plume photographs illustrating the passage of the current head and layer at measuring station X=3 for a heat transferring flow with $\Delta = .36$ and $Q = .025\,m^2/sec$ appears in figure 3.10. In the photographs can be seen the wire support at the left, and the thermocouple rake in the background. The generation of the first plume, which was photographed 230 msec after creation, occurred 2.5 seconds after initiation of the current flow, a time delay of about .5 seconds less than the previously measured front arrival time of this flow at X=3. The time interval between successive generations of smoke plumes was .90 seconds. The image of the first plume, in the first photograph, shows the displacement of the ambient fluid immediately in the

path of the current head by the head. In the second photograph, the contortion of the second smoke plume by the arrival of the head can be seen, as in the case for the third image, as well. A portion of the previously generated plume appears at the right. The fourth plume shows much less distortion, indicating that the current head has essentially passed, while the final two views show the relatively quiescent nature of the flow field upstream of the head. In the final image of the sequence, a rough outline of the quasi-steady local layer velocity profile can be seen.

Sequences such as that presented in figure 3.10, taken using longer initial delay times, demonstrated the quasi-steady nature of the local profile. Such photographs taken in the adiabatic nominal condition flow revealed profiles whose velocity maxima occurred at greater Y values than those for the heat transferring nominal case flow profiles. This difference is clearly illustrated by the smoke plume photographs presented in figure 3.11, taken in adiabatic and heat transferring flows with similar values of the parameters Δ and Q, at X=3. Although the thermal flow's initial value of Δ is greater than that of the adiabatic flow's, at the x position observed in the photographs the local density difference ratios of the two flows are similar. Comparison of velocity maximum Y values and minimum slope intercept layer thicknesses for profiles at different X locations for the nominal case thermal flow revealed a self-similar character of the current layer velocity profile.

3.4.3 Temperature Profiles and Layer Thickness

For computation of the layer minimum slope thicknesses as described in section 3.3, data from the thermocouple rake located at various downstream positions were averaged and plotted, with the result for the nominal case thermal current at X=3 plotted in figure 3.12. In this figure, the local layer overheat is

normalized by the initial source fluid overheat. This plot implies a layer thickness of 7 cm, and this result is plotted, along with thicknesses evaluated at other downstream positions, in figure 3.13. Calculation of the Froude number at the hot gas supply exit for the nominal case flows used in determining these layer thicknesses gave values below or near 1, assuring that a subcritical inlet condition to the channel existed, and precluding the existence of a hydraulic jump in the channel. Extrapolation of the points in figure 3.13 to x=0 also indicates that the exit slot height of 6 cm used for the nominal case flow was sufficiently large to allow for a subcritical flow into the channel. An interesting feature of this figure is the increase in h with x indicated, distinctly opposite to the trend exhibited by the viscous adiabatic flows examined in chapter 2. This thickenning of the layer as it slows down, in spite of its volumetric contraction due to heat loss, was observed for all overheats and flow rates examined.

Just as in the case for the velocity profiles, self-similarity of the temperature profiles was observed. Figure 3.14 shows the dimensionless temperature profiles at X=3 and X=7 for the nominal case flow, in which the local overheat has been normalized by the maximum overheat in the layer, and the dimension y by the local layer thickness, h. In addition, profiles from cases with $\Delta = .23$, $Q = .020\,\mathrm{m}^2/\mathrm{sec}$ and $\Delta = .46$, $Q = .010\,\mathrm{m}^2/\mathrm{sec}$ are plotted in the figure, and also collapse to nearly the same universal profile curve.

In light of this self similarity and the relatively low growth rate of the layer thickness with x, it is observed that the thermal boundary layer, δ_{th}, defined as the y value of the temperature profile maximum, increases with x at a rate less than the $x^{.5}$ dependence of flat plate laminar boundary layer growth. A similar observation of the velocity boundary layer, δ_v, is made, indicating that the heat transferring character of the current suppresses boundary layer growth.

3.4.4 Mass and Enthalpy Flux

Following the procedure outlined in section 3.4, layer mass fluxes at positions X=3 and X=7 were determined. Figure 3.15 shows the variation of the local mass flow rate in the buoyant layer as a function of downstream position, under steady state conditions (or far upstream of the current head) for the nominal case thermal flow. The inlet mass flux indicated in the figure is determined from the pressure measurement at the choked nozzle flow meter. The small difference between the mass fluxes at the two downstream locations is consistent with the previous observations of negligible entrainment by adiabatic currents, since this difference is about 5%, or on the order of the experimental accuracy of the measurements. There does appear to be a significant increase (about 30%) in the layer mass flux from the inlet condition to the first measurement 1.5 meters downstream. Since an entraining hydraulic jump did not exist near the inlet, this difference can be partially attributed to the error introduced in the layer flux measurements due to the presence of the channel sidewall boundary layers. Using expression 2.4.7 for the laminar displacement thickness, the estimated contraction of the spanwise flow dimension due to viscous sidewall effects at 1.5 meters downstream is of order 10% of the span, thus giving a correspondingly higher value for layer mass flux since the full .5 meter width of the channel was used in its calculation. In addition, the uncertainty associated with the hot gas supply's output mass flux is about 10%. The possibility also exists for some entrainment to occur at the entrance of the channel from start-up transients of the gravity current flow.

Figure 3.16 depicts the comparison of two layer enthalpy flux measurement techniques. As in the case for the mass flux calculations of the previous figure, essentially steady state conditions existed during measurements of the properties

used in these enthalpy flux calculations for the nominal case. Two dimensionality is also once again assumed. The solid line in the figure represents the local layer enthalpy flux as a function of downstream position in the duct as determined from a heat balance involving the input enthalpy flux and the heat transferred to the channel ceiling. The input enthalpy flux is determined from the input mass flux and input temperature difference as measured at the exit of the hot gas supply, and is approximately 2200 watts for the nominal case. Integrating the ceiling surface heat flux data from the inlet of the duct to a specific x and subtracting the result from the input enthalpy gives the enthalpy flux of the layer at that x location. Five such calculations are indicated on the figure by solid circles, with a solid line joining them. Seven centimeters of each sidewall were added to the .5 meter span in determining the surface area used in the heat flux integral calculations as a rough correction for sidewall heat transfer. Below this line are circles denoting the values of the local enthalpy flux of the gravity current layer as determined by integrating the enthalpy profiles produced from the measured velocity and temperature profiles. This figure demonstrates reasonable agreement between the layer enthalpy flux integral results and the flux as dictated by the surface heat transfer integrals. The enthalpy flux integral results are somewhat lower, however, but the uncertainties in the extrapolated ceiling heat flux values at values of x less than the value for the first measuring station are sufficiently high that the ceiling heat flux integral evaluated up to that point may be in error by as much as 200 watts, offsetting the enthaply flux curve by up to this much for all values of x. A more accurate validation of the heat balance measurements can be seen in the change in layer enthalpy flux between the two indicated measurements as compared to the change indicated by the curve representing the surface heat flux integral results. Since the ceiling heat

flux over the range x=1.5 meters to x=4 meters is known more accurately than near the inlet end of the channel, a lower uncertainty in the surface heat flux integral results, and correspondingly better agreement between the flux value changes obtained from the two methods is seen.

3.4.5 Layer Richardson Number

An overall measure of the relative importances of buoyancy and inertial forces in a flow can be expressed in terms of a Richardson number, Ri, defined in the following analysis. Expressing the Navier Stokes equations,

$$\rho\left(\frac{\partial \mathbf{u}}{\partial t} + (\mathbf{u}\cdot\nabla\mathbf{u})\right) = -\nabla p + \mu\nabla^2\mathbf{u} + \rho\mathbf{g}\,, \tag{3.4.4}$$

about a point of hydrostatic equilibrium, using $p = p_0 + p'$, $\rho = \rho_0 + \rho'$, and $\nabla p_0 = \rho_0\mathbf{g}$, we get:

$$(\rho_0 + \rho')\frac{D\mathbf{u}}{Dt} = -\nabla p' + \mu\nabla^2\mathbf{u} + \rho'\mathbf{g}\,. \tag{3.4.5}$$

Non-dimensionalizing equation 3.4.5, using a characteristic velocity of the flow U, and length scale L, we obtain:

$$\frac{D\mathbf{u}^*}{Dt^*} = \frac{-\nabla p'}{\rho_0 U^2} + \frac{\mu\nabla^2\mathbf{u}^*}{\rho_0 UL} - \frac{L\rho' g\hat{\mathbf{j}}}{\rho_0 U^2}\,, \tag{3.4.6}$$

where the Boussinesq approximation of neglecting the effect the variation in density, ρ', has in the inertial terms as compared to its effect in the buoyant term, has been made. Rewriting the equation in terms of dimensionless coefficients:

$$\frac{D\mathbf{u}^*}{Dt^*} = -\nabla p'^* + \frac{1}{Re}\nabla^2\mathbf{u}^* - Ri\hat{\mathbf{j}}\,, \tag{3.4.7}$$

we see that the buoyant term in the equation is significant for values of Ri not small compared to 1, where

$$Ri = \frac{L\rho' g}{\rho_0 U^2} = \frac{\frac{\Delta\rho}{\rho_0} gh}{U^2} = \frac{\Delta gh}{U^2}\,, \tag{3.4.8}$$

in terms of the current layer thickness, h, and parameter Δ, where U is taken to be the local velocity profile maximum. A positive value of Ri is associated with stable density stratification, i.e., the density gradient in the same direction as the accelerational field. The term:

$$\frac{\rho'}{\rho_0} g = \Delta g \,,$$

is often referred to as the reduced gravitational acceleration, g'. Investigations of interfacial stability in stratified flows have demonstrated that small disturbances of any wave number are stable for values of $Ri > 1/4$ (for linear density and velocity profiles). Thus, the overall Richardson number is both a measure of the relative significance of buoyant and inertial forces, and of stability. Using the local gravity current layer quasi-steady value of h and the velocity profile maximum, U, to compute Ri, the value of Ri as a function of downstream position, x, can be examined from the data from the nominal case thermal flows, and is presented in figure 3.17. This figure shows that the value of Ri is essentially constant over x, assuming a value between .9 and 1. Flows with inlet conditions giving Froude number less than 1, $Fr \sim \frac{1}{\sqrt{Ri}}$, adjusted to values of $Ri \approx 1$ before the first x position at which measurements were made, and flows with parameters other than those of the nominal case also exhibited Richardson numbers of the magnitude seen for this nominal case example.

It is of interest to note that the value of Ri remains high for increasing x in spite of the considerable heat loss by the current as it propagates downstream, indicating that buoyant forces continue to be significant in thermal gravity current flows even after the local layer overheat has diminished to a small fraction of its value upstream.

For the adiabatic flows examined in Chapter 2, the inviscid theory gives:

$$C_1 = \frac{V}{\sqrt{g\Delta h}} \approx \frac{U}{\sqrt{g\Delta h}} \approx \frac{1}{\sqrt{Ri}}, \tag{3.4.9}$$

assuming the front velocity is equal to the layer velocity, and thus:

$$Ri \approx \frac{1}{{C_1}^2}, \tag{3.4.10}$$

which is of order one for the values of C_1 obtained by the theory for various values of h/d. Thus, gravity currents in general are significantly influenced by local buoyant forces, and maintain a value of Richardson number of about one regardless as to whether they lose buoyancy with downstream propagation or conserve buoyancy as the adiabatic flows do.

3.4.6 Gravity Current Heat Transfer

The convective heat transfer to the ceiling of the channel by the thermal gravity current played a dominant role in the definition of the current's flow field, as seen in the significantly different spreading rate and layer thickness results in sections 3.4.1 and 3.4.3 as compared to those for the adiabatic gravity current. The choice of the high thermal capacity aluminum channel ceiling did in fact produce the desired constant wall temperature boundary condition, as demonstrated by the constant room temperature readings of the surface mounted thin foil thermocouples during thermal current experiments. The calculated surface temperature increase based on heat flux measurements was of order .1° C, less than the resolution of the thermocouple measurements.

As is the convention for forced convection flat plate heat transfer study, the heat transfer data are presented in terms of Nusselt number, $Nu = \frac{\mathrm{h}\,x}{k}$, versus Reynolds number, $Re = \frac{U\,x}{\nu}$. Here h is the heat transfer coefficient defined by $q = \mathrm{h}\,(T_\infty - T_w)$, where q is the heat flow per unit area, and k the thermal

conductivity of the fluid. T_∞ is taken to be the local maximum current layer temperature and T_w the ceiling temperature, while the fluid properties k and ν are evaluated at the film temperature, $T_f = \frac{T_\infty + T_w}{2}$. The relationships between Nu_x and Re_x for conventional convective flat plate heat transfer are of the form:

$$Nu_x = .33 Pr^{2/3} {Re_x}^{1/2} \text{ (laminar)}, \tag{3.4.11}$$

$$Nu_x = .037 Pr^{2/3} {Re_x}^{4/5} \text{ (turbulent)}, \tag{3.4.12}$$

where $Pr = \nu/\alpha$, and α is the thermal diffusivity. The transition from laminar to turbulent flow normally occurs at roughly $Re_x = 3 \times 10^5$, and although the values of Re_x in the thermal current flows did not exceed 10^5, the gravitational instability of the thermal boundary layer at the ceiling was seen to promote turbulent transition for much lower values of Re_x than 3×10^5 through its effect on the heat transfer mechanism, as discussed further in this section.

Typical results of ceiling heat transfer measurements during the flow of a heat transferring gravity current can be seen in figure 3.18. The arrival times of the current front at the X stations monitored, inferred from the traces in the figure, correspond closely to those deduced from the free-stream thermocouple outputs recorded simultaneously, although typically a small delay of about .1 seconds was observed between detection of current front X station arrival by the heat flux gauges and front arrival detection by the thermocouples located 2.5 cm below the ceiling. This time difference can be explained by the fact that the nose of the current protruded several centimeters ahead of the downstream-most contact point of the current with the channel ceiling.

Also evident in figure 3.18 are fluctuations of the heat flux values as large as about 50% of the mean heat flux levels. These fluctuations are relatively greater than those seen in the temperature measurements when compared to mean values, and since the area resolution of the heat flux gauges was about 1 cm x

1.5 cm, the phenomenon responsible for these fluctuations had a characteristic length scale of at least 1-2 cm. Since the thermocouples in the rake were spaced 1.5 cm apart in the Y dimension, beginning at Y=1 cm, and revealed no strong correlation between adjacent temperature measurements, the mechanism creating the heat flux fluctuations was confined within the layer at Y values of less than about 2 cm, the typical scale of the thermal boundary layer for the nominal case flow.

In an extension of the Rayleigh-Bénard problem of convective cellular motion, induced by an unstable density gradient resulting from the heating of a fluid from below, to include cross flow, Davis and Choi (1977) observed longitudinal roll structures appearing in the fluid adjacent to the heated wall, with length scales in the dimensions orthogonal to the cross flow direction comparable to the thermal boundary layer thickness. This process is believed to be the cause of the large heat flux variations measured in the thermal gravity current flows. This mechanism is discussed below, and was further investigated using flow visualization techniques as described in the next section.

For the nominal condition thermal flow, the heat transfer, velocity, and temperature measurements throughout the flow were used to examine Nu_x as a function of Re_x, with the results given in figure 3.19. In this plot can be seen two notable features: first, that the slope of the line indicated by the points is about 1.0, and secondly, that the magnitude of the Nusselt number is three to five times higher than that predicted by the turbulent convection result of equation 3.4.12.

The stronger Re_x dependence of Nu_x demonstrated by the thermal gravity current as compared to the laminar heat transfer theoretical dependence of $Re_x^{.5}$, clearly indicates that the thermal boundary layer instability dictates turbulent heat transport even for values of Re_x much less than the constant free-stream

velocity flat plate transition value of $Re_x = 3 \times 10^5$. The overriding of gravitationally unstable ambient fluid discussed in section 2.4.5 is also believed to contribute to this early transition to turbulence. The linear dependence of Nu_x on Re_x shows that the heat transfer coefficient h depends only on local quantities, particularly velocity V, and not on downstream position, x. This is consistent with the previous finding that the local boundary layer thicknesses, δ_{th} and δ_v, varied little with downstream position. It is interesting to note that just as the dimensionless heat transfer coefficient, C_H, where

$$C_H = \frac{Nu_x}{Re_x Pr},$$

is independent of Re_x for thermal gravity current flow, Schwarz and Cosart found the friction coefficient, C_f, for turbulent wall jets to also be independent of Re_x.

The result that the values of Nu_x were some three to five times higher than those expected for turbulent flat plate heat transfer for comparable values of Re_x can also be explained in terms of the longitudinal roll convection cells. By convecting away the gravitationally unstable cooled gas at the ceiling surface and transporting to the ceiling hotter gas from distances below the ceiling comparable to the thermal boundary layer thickness, these convection rolls augment heat transfer in much the same way as boiling heat transfer is promoted by vigorous nucleation activity. Davis and Choi used a Couette flow with constant wall heat flux to examine the effect these rolls had on convective heat transfer and found that the combined free and forced convection increased Nusselt numbers by over 300% as compared to those of purely forced convection flows, an increase equivalent to that found in the gravity current flows with constant wall temperature examined here.

Just as the critical Rayleigh numbers exist for the onset of cellular motion in the Rayleigh-Bénard problem, Davis and Choi found critical values of Ra

(although for constant wall heat flux) to exist for the onset of longitudinal roll convection as functions of ξ, the downstream position normalized by the product of d and the Peclet number, $Pe = d\bar{u}/\alpha$, where $\bar{u}$ is the mean velocity in the layer. For our case of constant wall temperature, the Rayleigh number can be defined as: $Ra = \beta g d^3 \triangle T/\alpha\nu$, where β is the coefficient of volumetric expansion, d the fluid layer thickness, α the thermal diffusivity, and $\triangle T$ the temperature difference across the fluid layer. Applying their results in terms of the gravity current parameters, we find that almost the entire length of the duct is downstream of the expected onset location of the longitudinal rolls, even for flows with low values of Δ, although their results were obtained from a flow field much different in nature than that of gravity current flow. Figure 3.20 shows the results of Nu_x versus Re_x measurements for flows with parameters different than those of the nominal case, plotted together with the nominal case results. These results show that even for significantly lower overheats, at small values of x, heat transfer augmentation nonetheless occurs. Results from runs even with the lowest values of Δ examined, $\Delta = .05$, are in agreement with the nominal case results. This case represents values of Ra of about 1000, or 1/20 those of the nominal case flow (it is of interest to note that Ra is found to remain essentially constant along x for a given run). These results can be summarized by an empirical relation describing Nusselt number as a function of Reynolds number for thermal gravity current heat transfer:

$$Nu_x = .013 Re_x \,. \tag{3.4.13}$$

Although the Prandtl number for the experiments performed was a constant value of about .7, a dependence of Nu_x on Pr may be similar to that of the laminar and turbulent convection results of $Pr^{2/3}$ dependence. Davis and Choi found no significant dependence on longitudinal roll onset on Prandtl number.

3.4.7 Qualitative Characteristics

In addition to their use in the flow visualization technique for layer velocity measurement, smoke plumes were employed for visualization of the longitudinal convection cells in the thermal boundary layer of the heat transferring gravity current. Figure 3.21 shows a typical plume photographed 100 msec after generation, at a Y value of 1 cm, for a flow with $\Delta = .36$ and $Q = .016\,\mathrm{m}^2/\mathrm{sec}$. At this X=3 position the thermal boundary layer thickness, δ_{th}, was about 2 cm. The undulations of the plume indicate the presence of the roll structures, and reveal a typical wavelength, λ, or spacing between counter-rotating roll pairs, of about 3 cm. Davis and Choi found this spacing to be typically:

$$\delta_{th} < \lambda < 3\delta_{th}\,,$$

essentially consistent with the present results. Figure 3.22 depicts the basic features of these longitudinal rolls, showing a transverse cross section of this natural convection phenomenon. As a verification that these perturbations of the plume are thermally induced, a similar photograph was taken in an adiabatic flow with roughly the same parameters Δ and Q, and appears in figure 3.23. In this view of the plume, no coherent undulations appear, indicating that these roll structures do not occur in the gravitationally stable boundary layer of the adiabatic flows. The observation that the rolls were not evenly spaced across the span, as Davis and Choi saw them to be, can be attributed to the three dimensionality induced by the overridden ambient fluid and sidewall effects, in addition to the transverse instability these rolls were observed by Davis and Choi to undergo at values of Ra of about 2×10^5. For values of Ra of about 2.7×10^5, they observed a fully turbulent film resulting from this instability. Although the local value of Ra for the case represented in figure 3.21 was about 2×10^4, below the transverse instability inception value, it is possible that the instability of the

overridden fluid promotes transverse instability inception at lower values of Ra. The lowest values of Ra examined, about 1000, were sufficiently high to induce the convective-roll mechanism and associated high values of Nusselt number.

The difference in velocity boundary layer thicknesses between thermal and adiabatic flows with similar parameters, observed in section 3.4.2, can also be attributed to this cellular convective mechanism. The transport of high momentum fluid to the wall, and low momentum fluid away from it, by this convective phenomenon in the thermal flow, serves to compress the velocity profile shape and leave a thinner, higher gradient boundary layer near the wall as compared to that of the adiabatic flow.

One final set of qualitative observations involved shadowgraph visualization of the thermal current structure as it passed a given downstream location. A typical sequence of shadowgraph images depicting the structures of the nominal case thermal flow current head and upstream layer as they passed downstream position X=2, appears as figure 3.24. The markers in the lower left of the photographs were 12 cm and 22 cm below the ceiling, and the time interval between successive photographs was about 1/3 second. The first two images in the figure show evidence of the lobe and cleft structure seen in the adiabatic current fronts, while the final two views reveal the smoothly stratified character of the current layer upstream of the head, and a characteristic layer thickness one half that of the leading head. The perturbations evident in the ambient fluid ahead of the front are a result of the low overheat of the ambient fluid adjacent to the hot gas supply/channel door acquired during warm-up prior to the performance of the run. The general structure of the thermal currents was observed through shadowgraphy to be similar to that of the adiabatic gaseous and liquid flows.

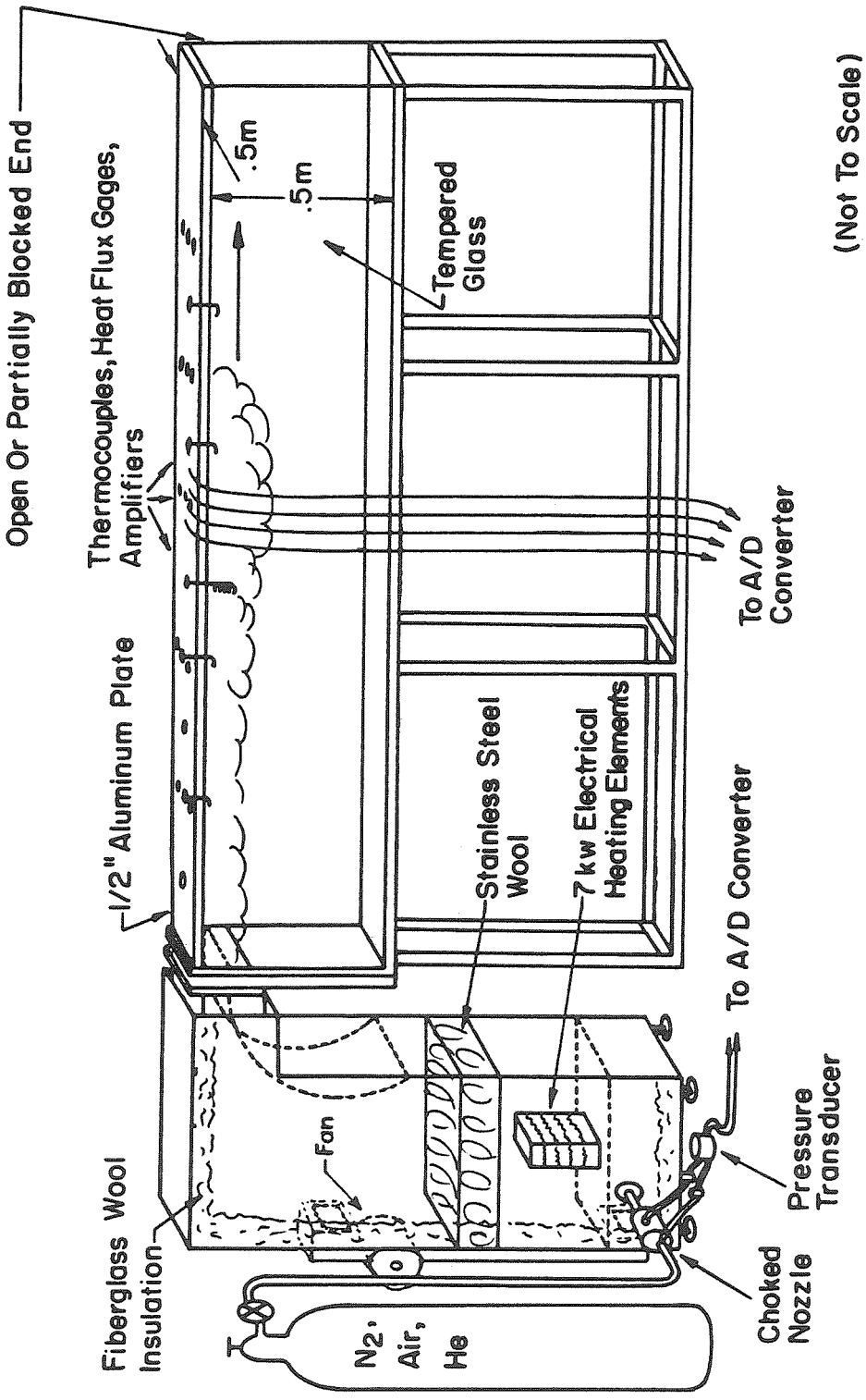

Figure 3.1 Schematic of gaseous gravity current experimental apparatus.

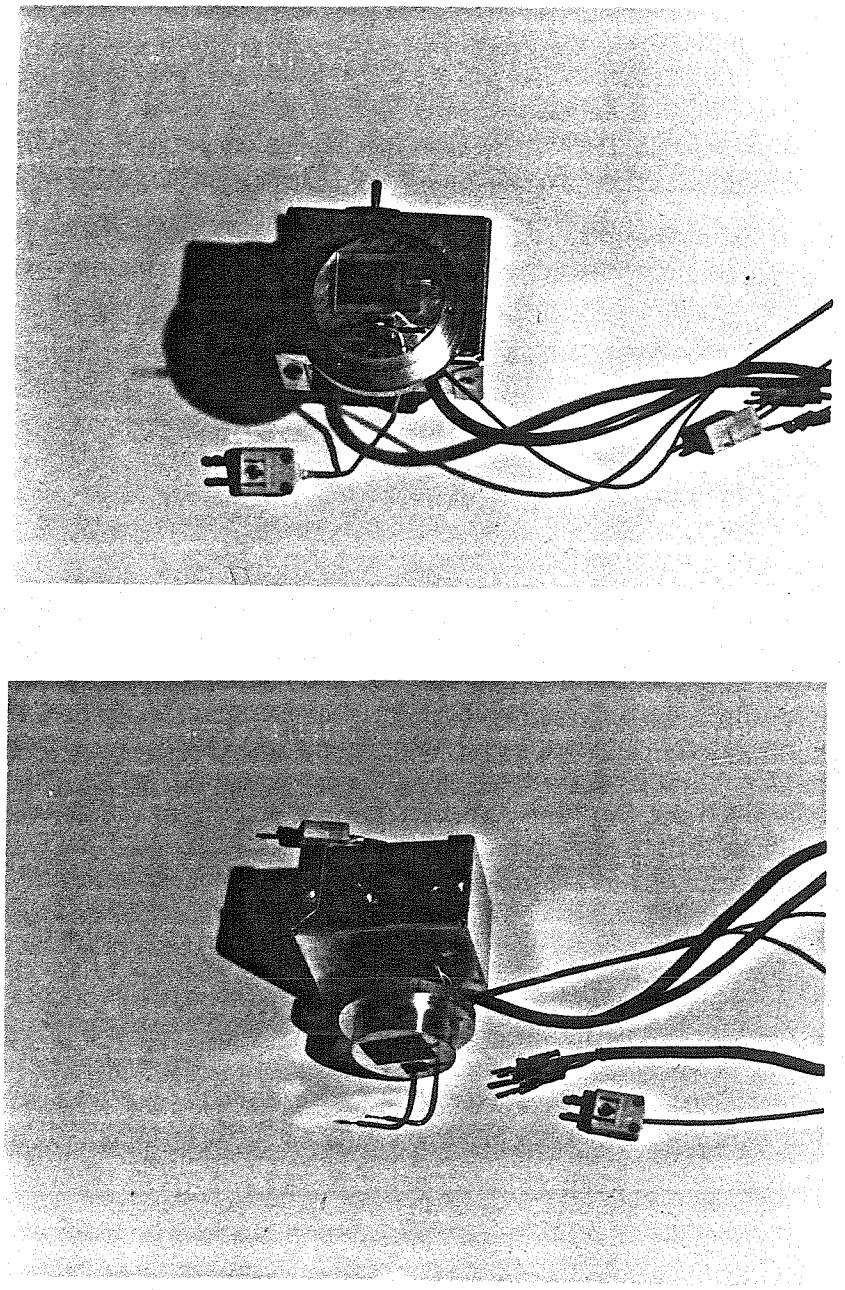

Figure 3.2 Photographs of typical instrument-bearing plug.

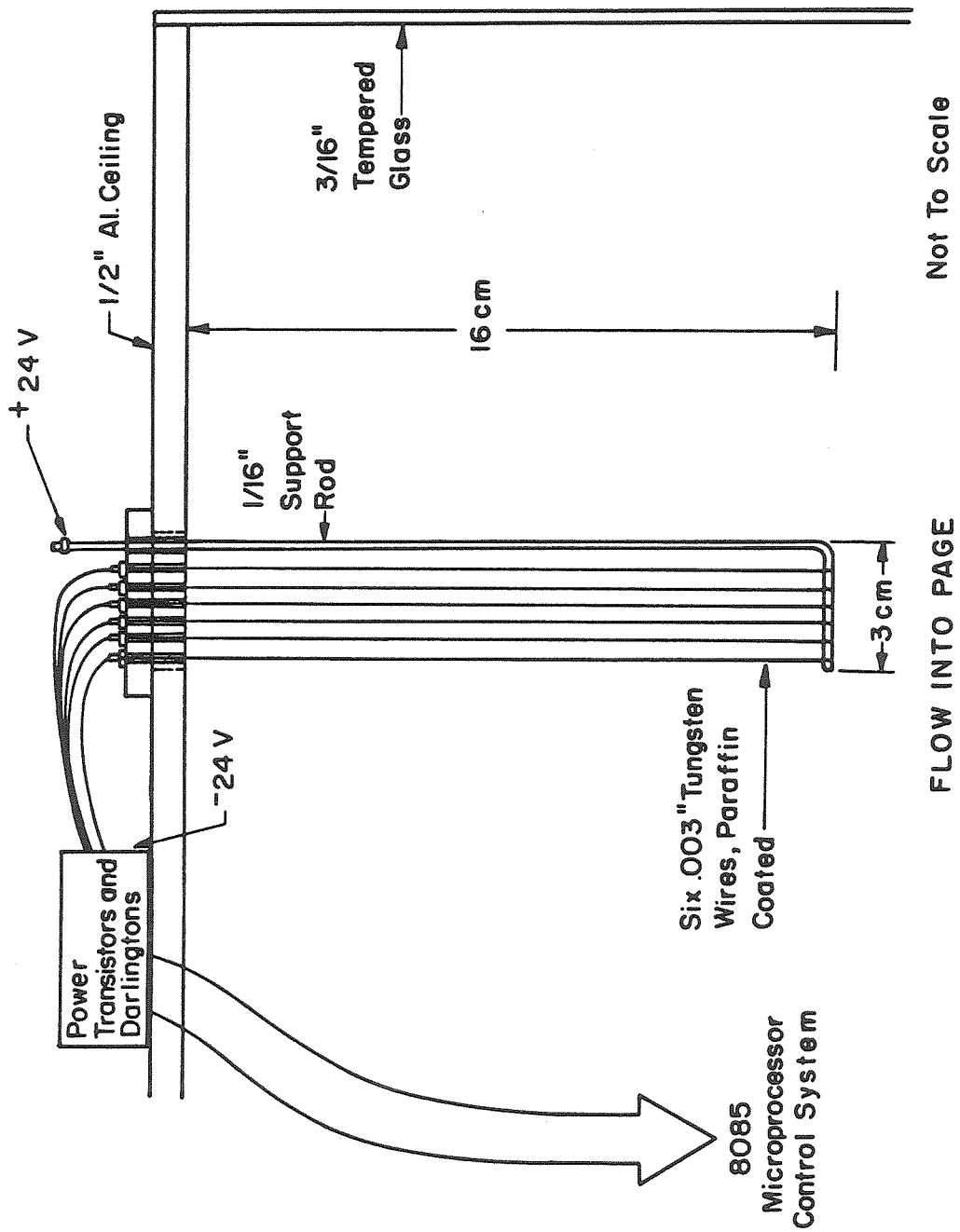

Figure 3.3 Schematic of smoke pulse probe.

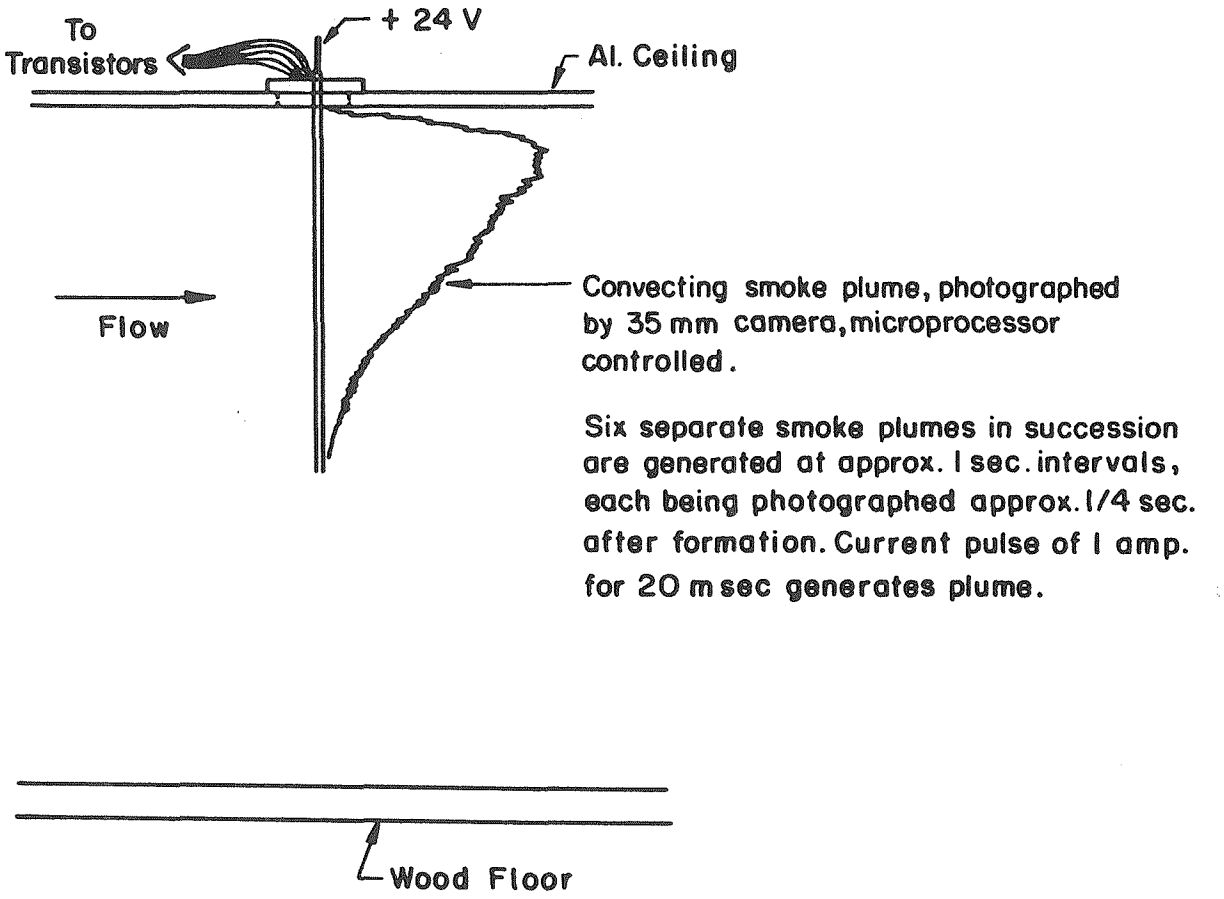

Figure 3.4 Schematic of smoke pulse velocity measurement technique.

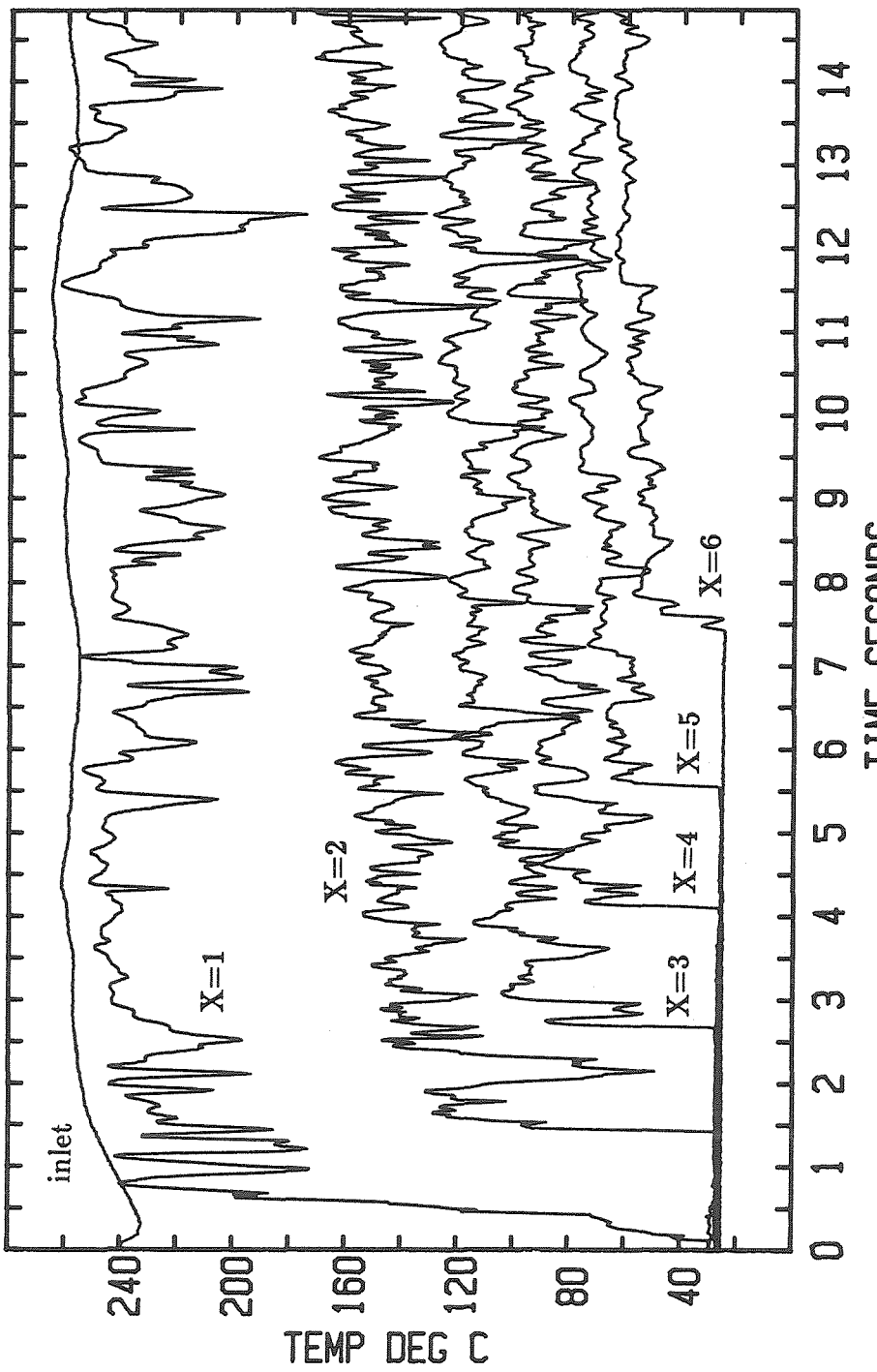

Figure 3.5 Temperature versus time measurements for a nominal condition thermal current, $\Delta = .46$, $Q = .030\,m^2/sec$.

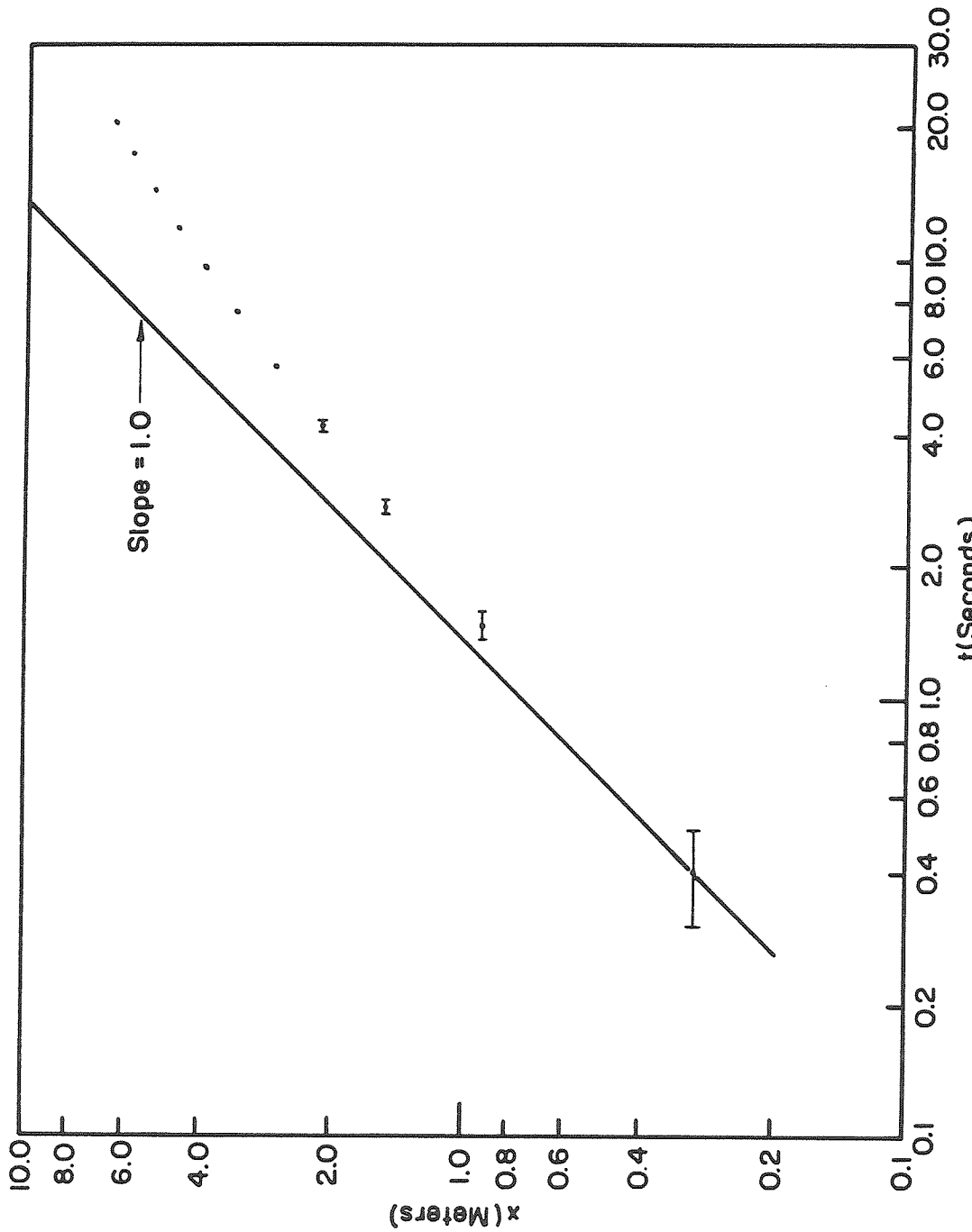

Figure 3.6 Thermal current front position versus time for nominal condition flow, $\Delta = .46$, $Q = .030\,m^2/sec$.

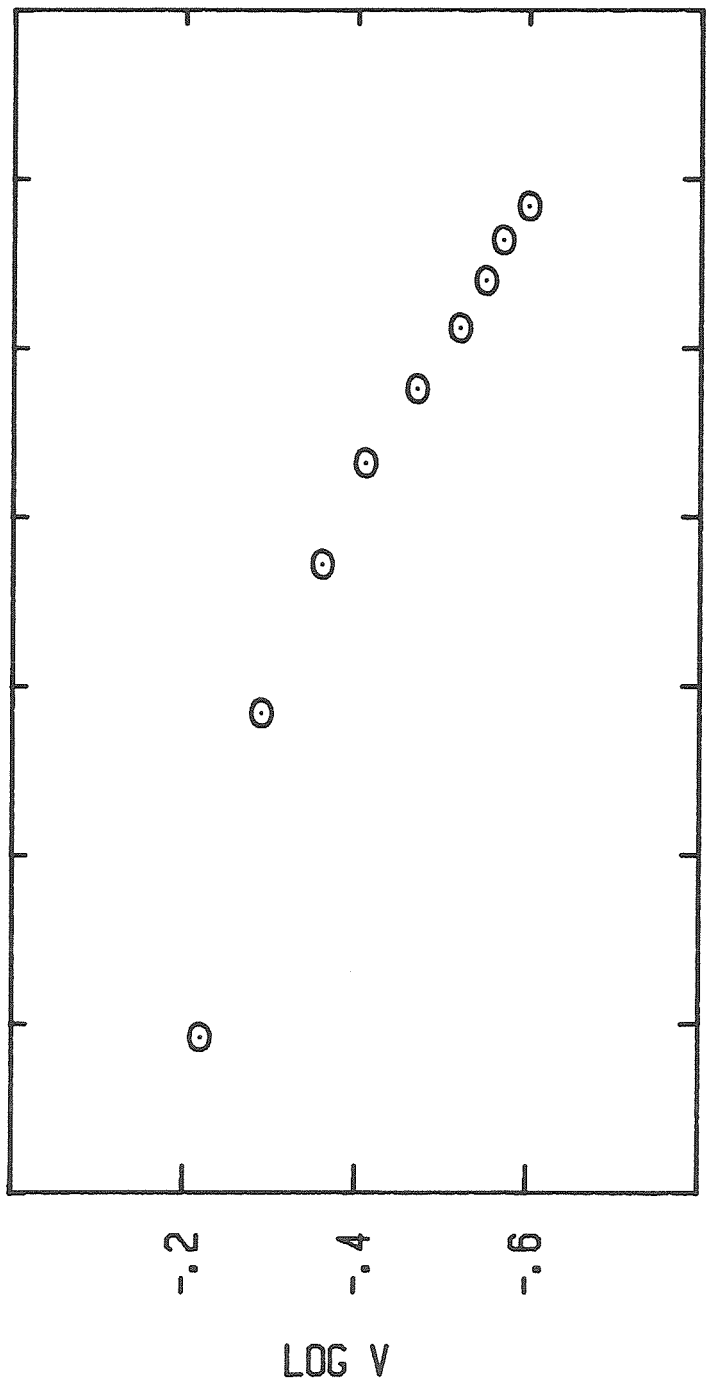

Figure 3.7 Log V versus log t, where V is the thermal current front velocity, for nominal condition flow, $\Delta = .46$, $Q = .030\,m^2/sec$.

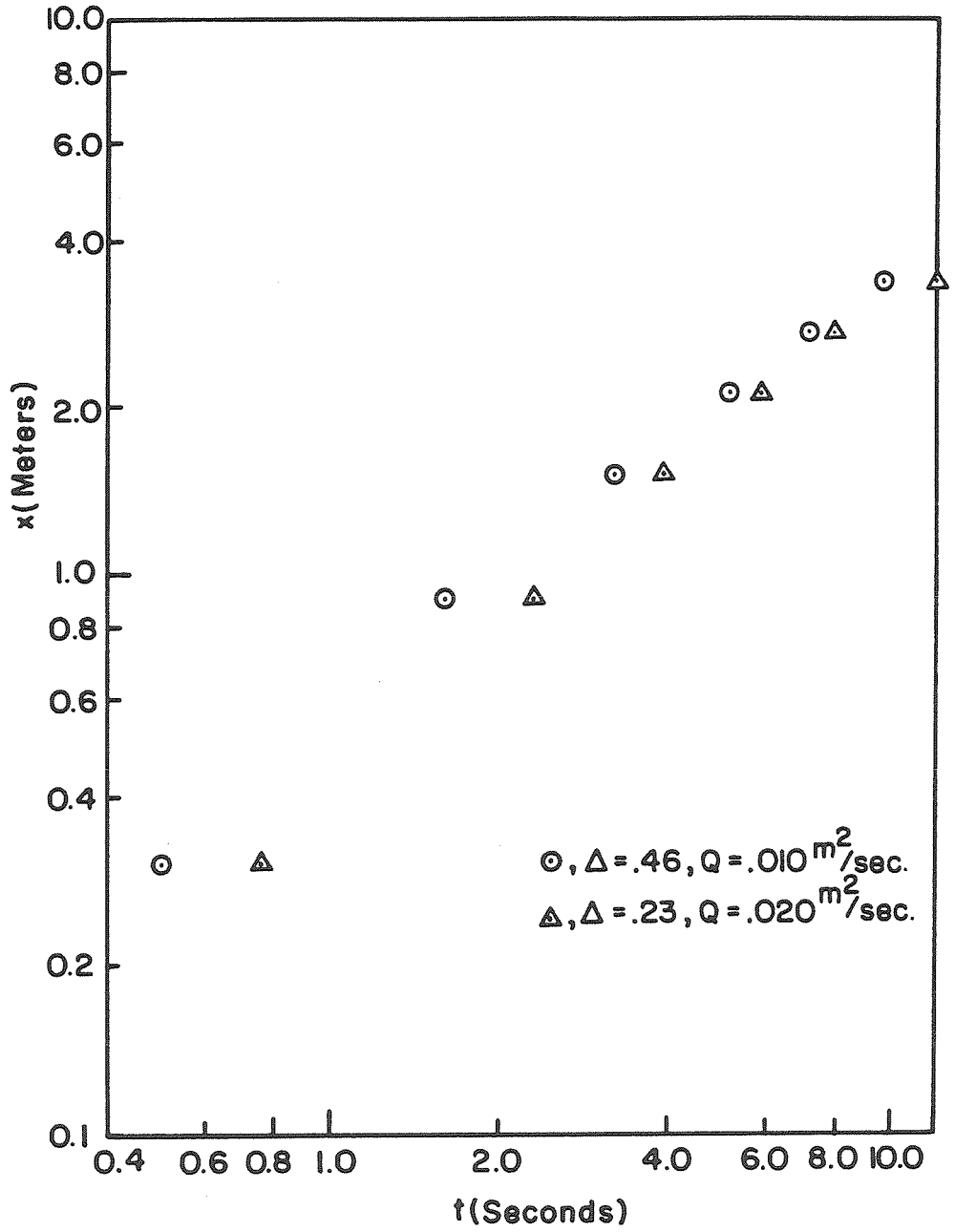

Figure 3.8 Thermal current front position versus time for flow of $\Delta = .46$, $Q = .010\,\mathrm{m}^2/\mathrm{sec}$, and $\Delta = .23$, $Q = .020\,\mathrm{m}^2/\mathrm{sec}$.

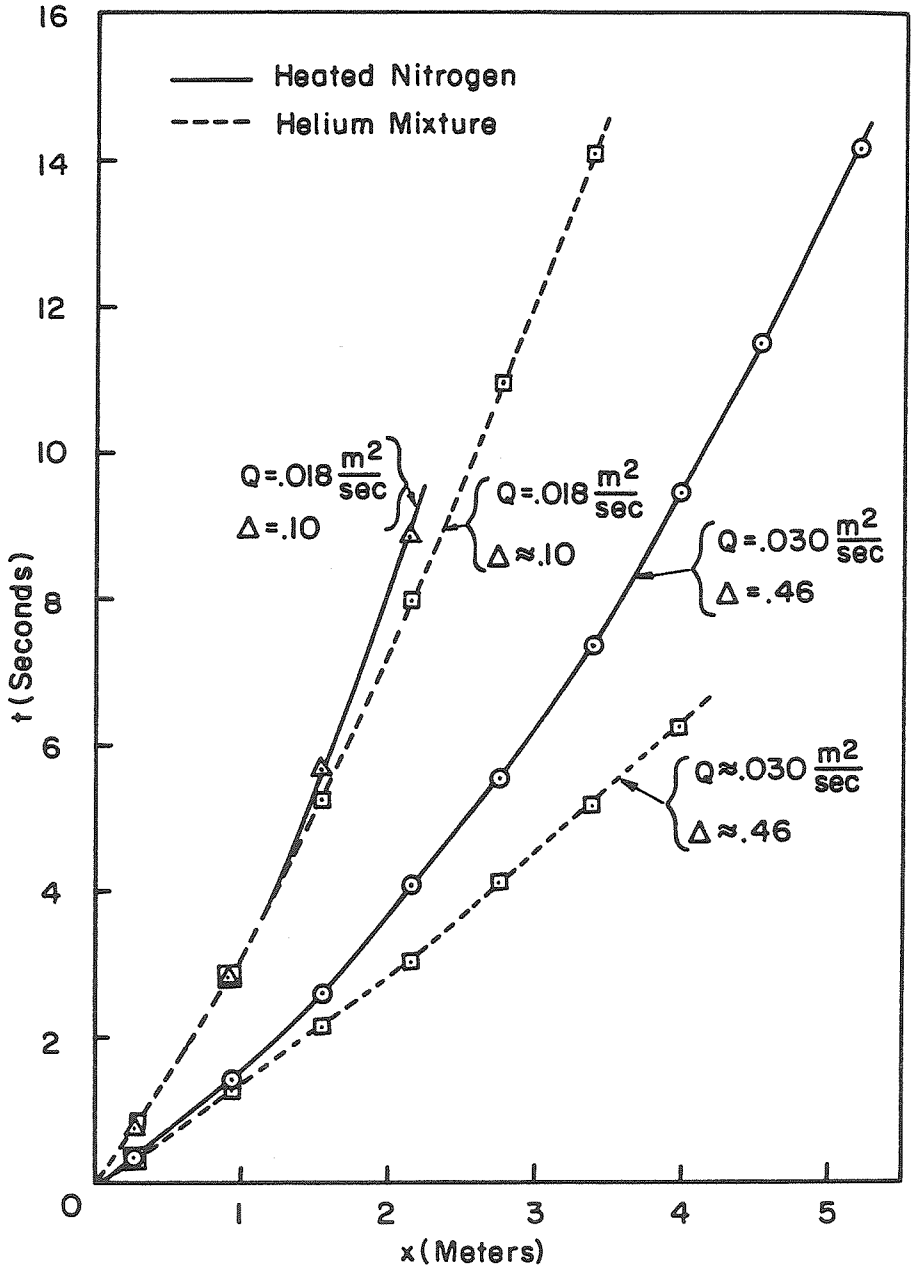

Figure 3.9 Current front position versus time for thermal and adiabatic flows with equivalent initial parameters Δ and Q.

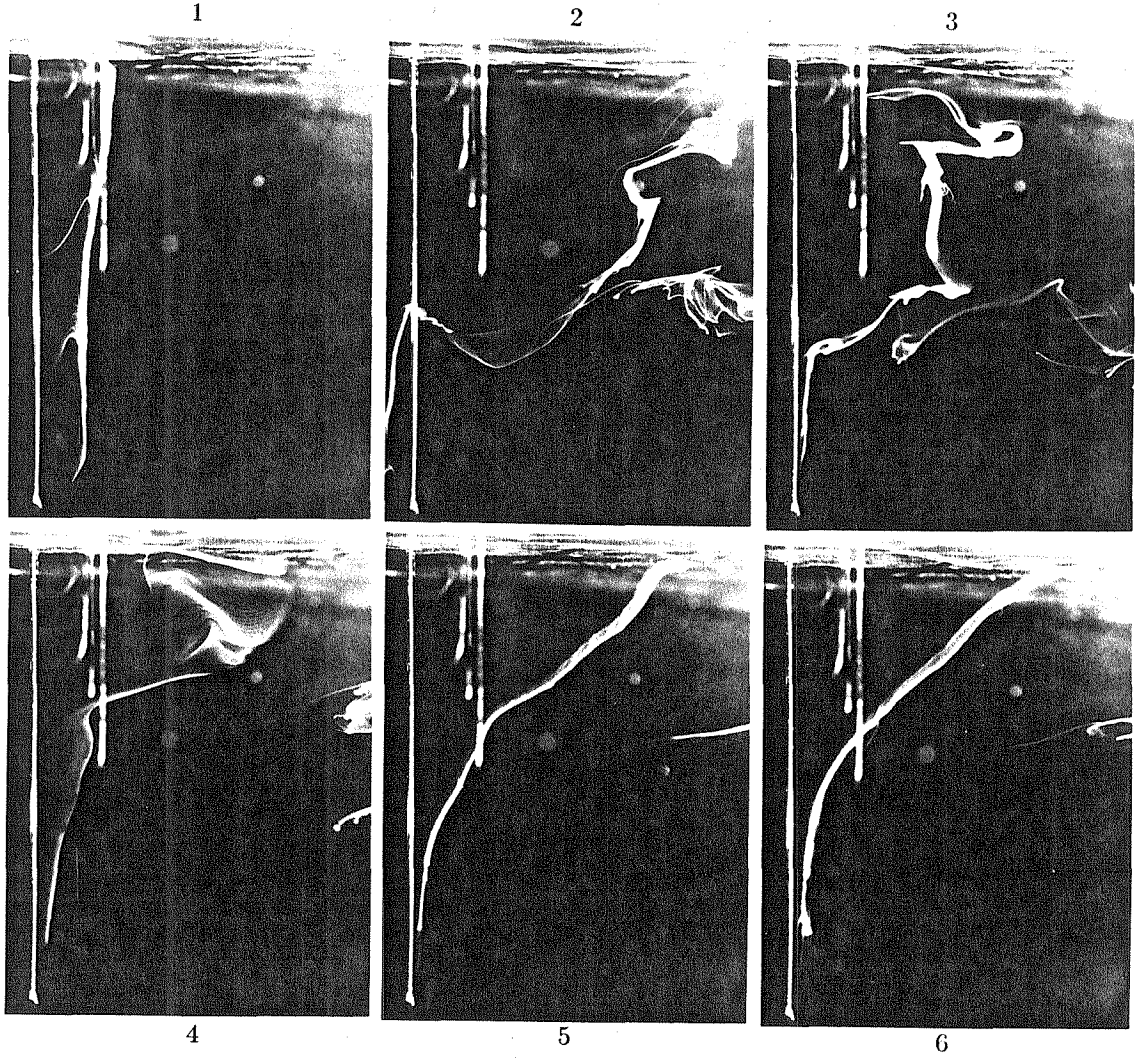

Figure 3.10 Sequence of smoke plume photographs taken at X=3 for thermal flow with $\Delta = .36$ and $Q = .025\,\mathrm{m}^2/\mathrm{sec}$.

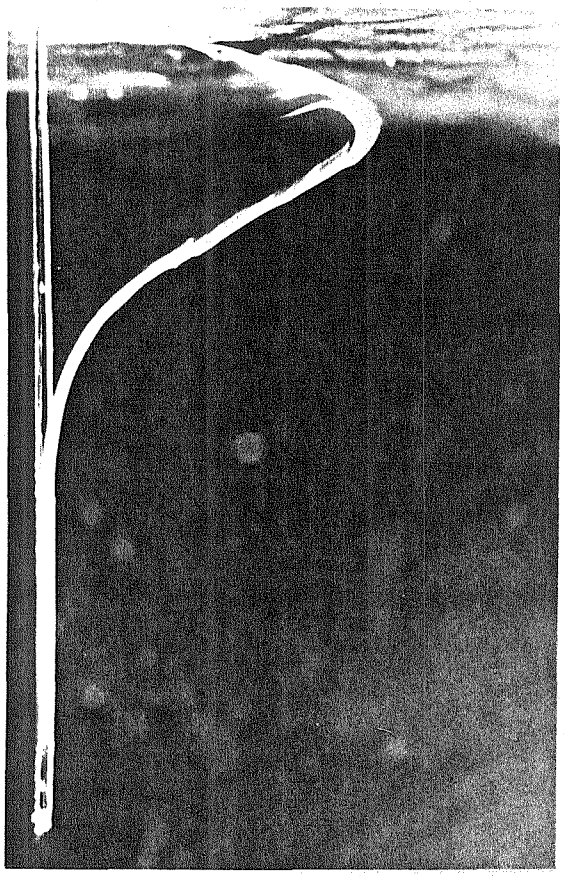

adiabatic flow with $\Delta \approx .30$ and $Q \approx .015\,\mathrm{m}^2/\mathrm{sec}$

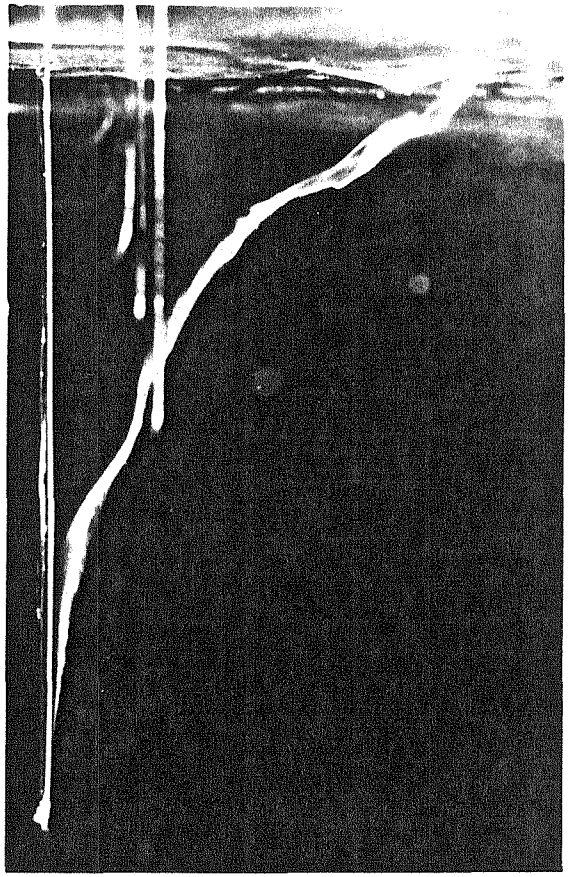

thermal flow with $\Delta = .36$ and $Q = .020\,\mathrm{m}^2/\mathrm{sec}$

Figure 3.11 Comparison of smoke pulse velocity profile photographs for adiabatic and thermal flows taken at X=3 .

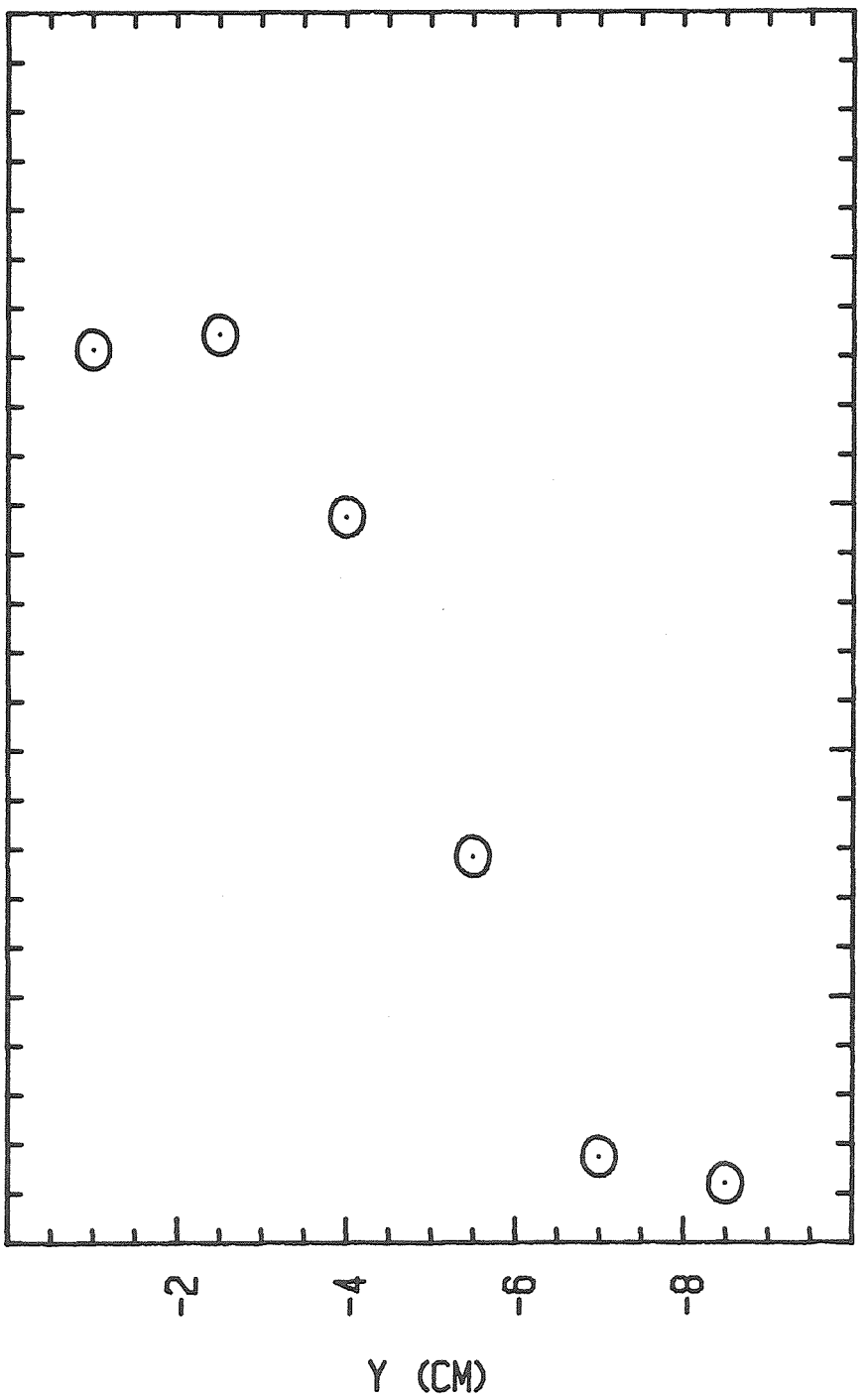

Figure 3.12 Temperature profile for nominal case thermal flow measured at X=3; $\frac{T-T_o}{T_{inlet}-T_o}$ versus y (cm).

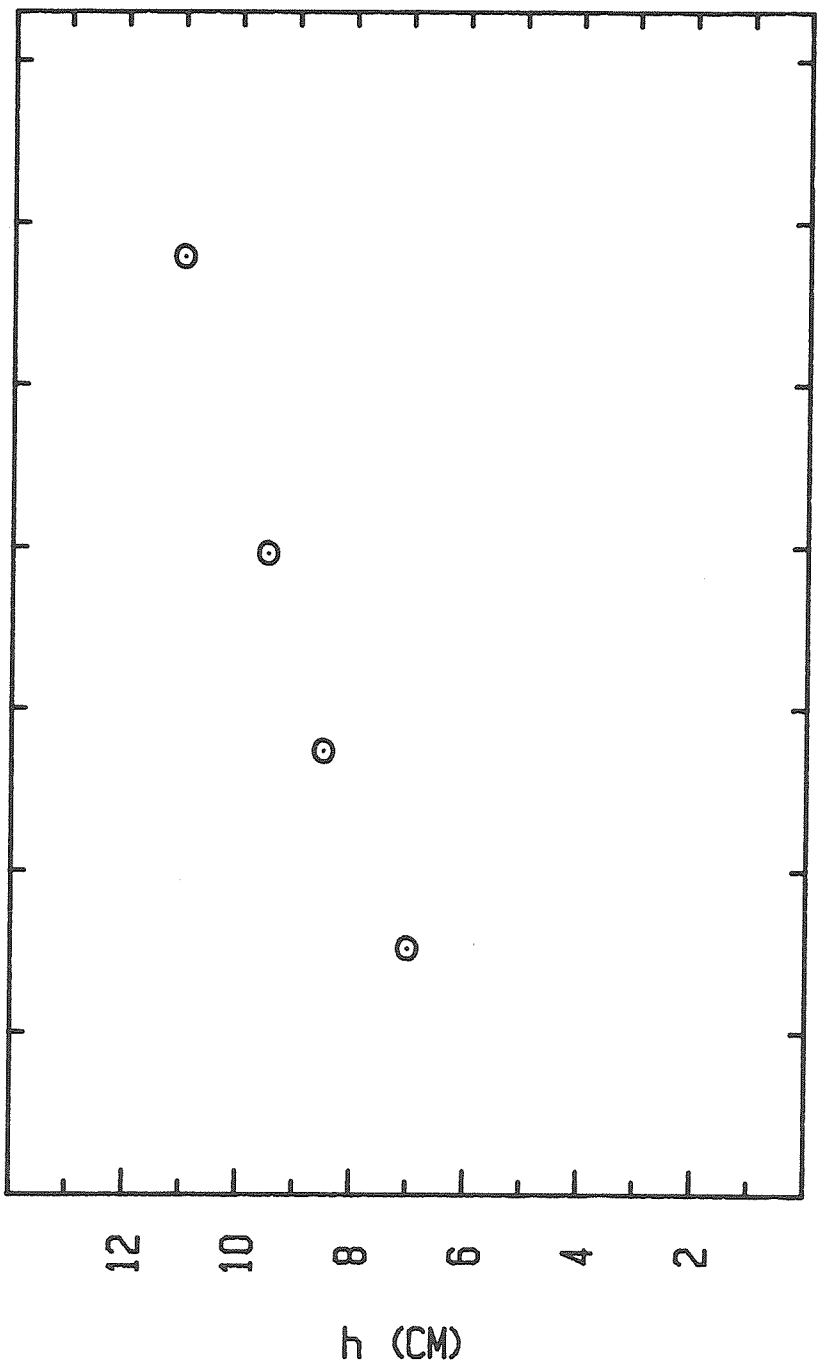

Figure 3.13 Thermal current layer thickness, h, versus streamwise position, x, for nominal case flow.

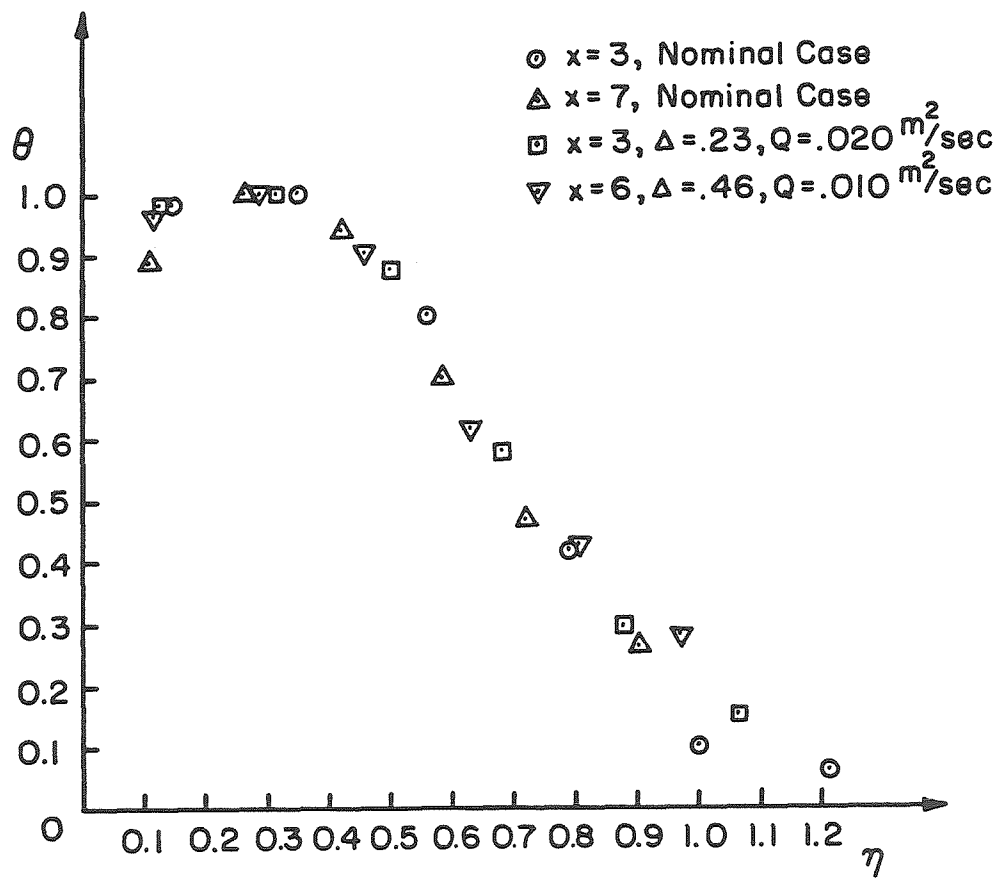

Figure 3.14 Dimensionless temperature profile self-similarity; $\Theta = \frac{T-T_o}{T_{max}-T_o}$ vs. $\eta = \frac{y}{\delta}$.

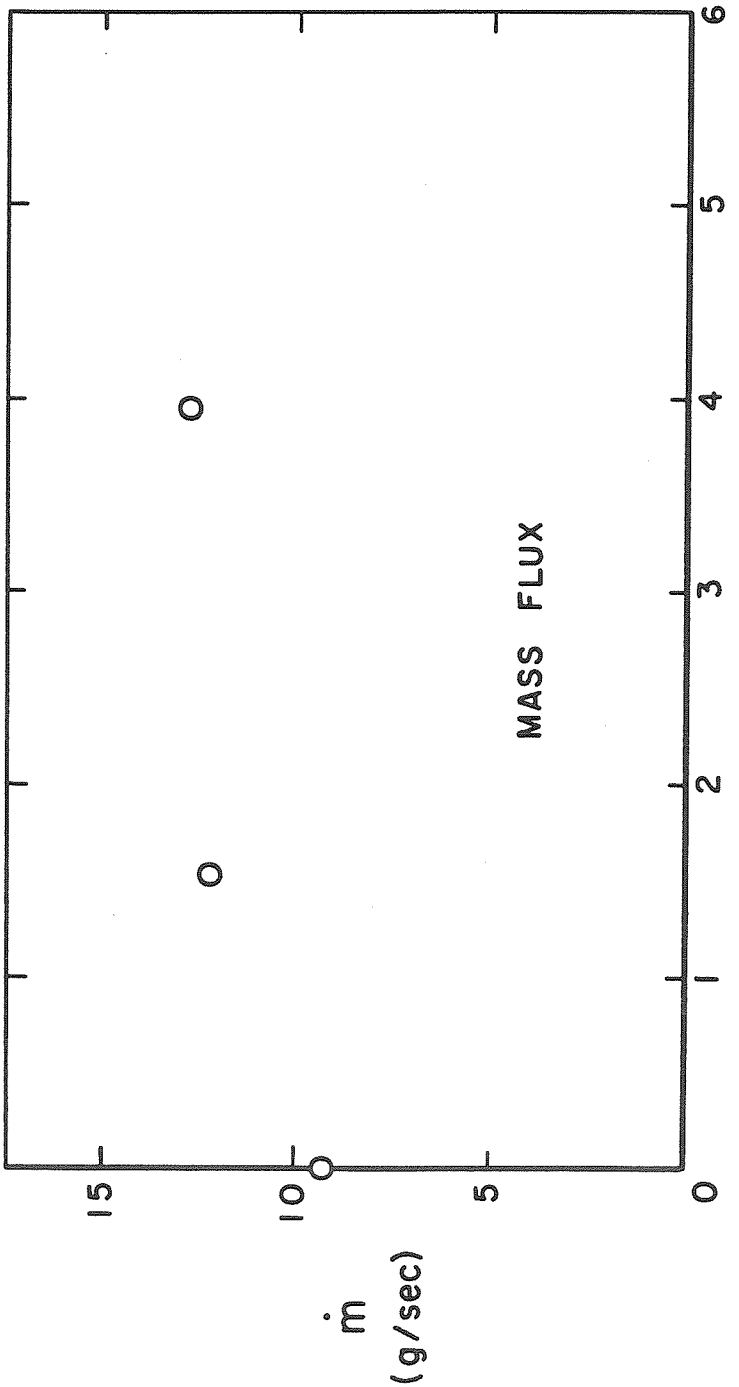

Figure 3.15 Thermal current layer mass flux, $\dot{m}$ (m/sec), versus streamwise position, x(m), for nominal case flow.

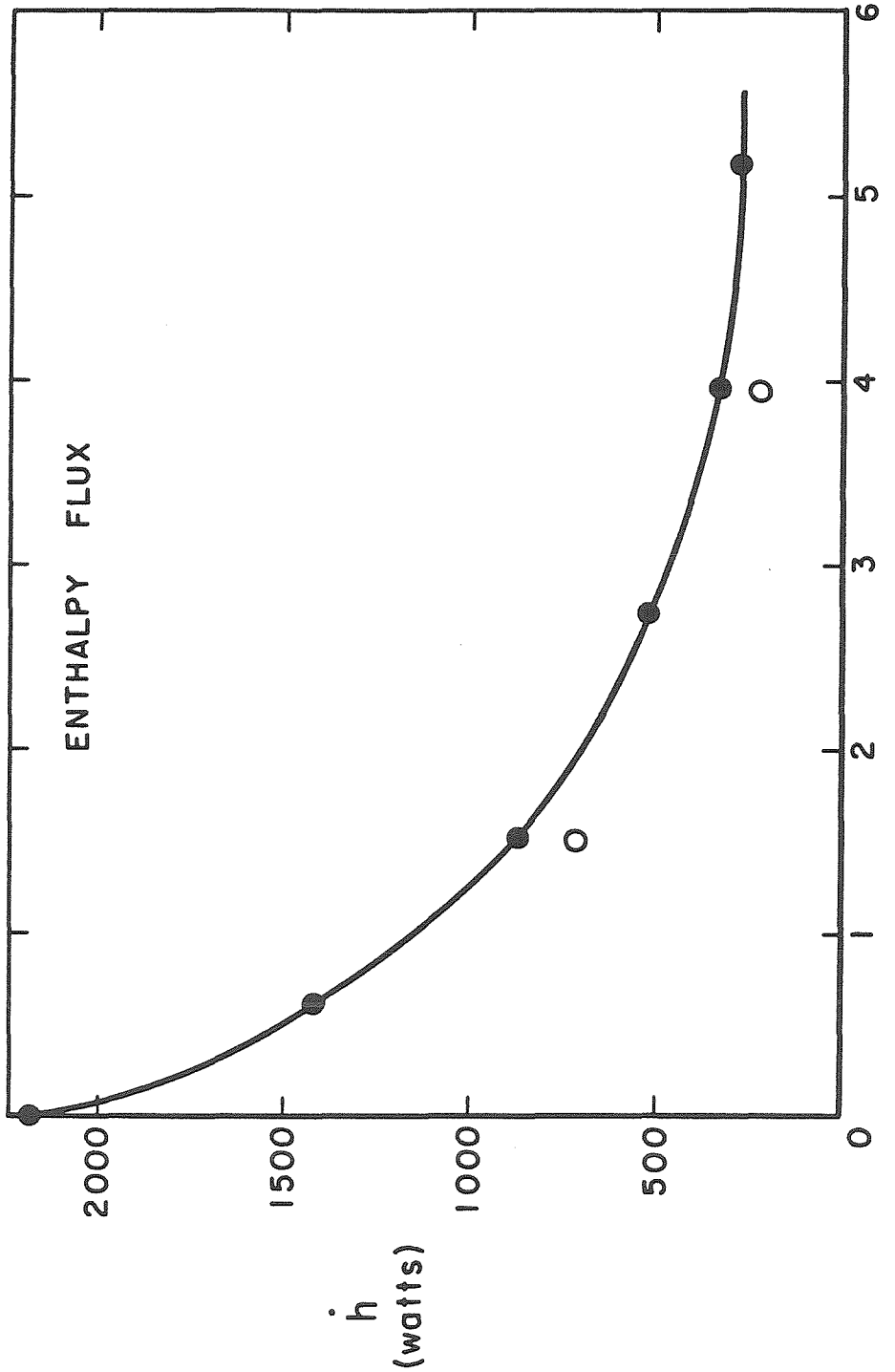

Figure 3.16 Thermal current layer enthalpy flux, $\dot{h}$ (watts), versus streamwise position, x(m), for nominal case flow.

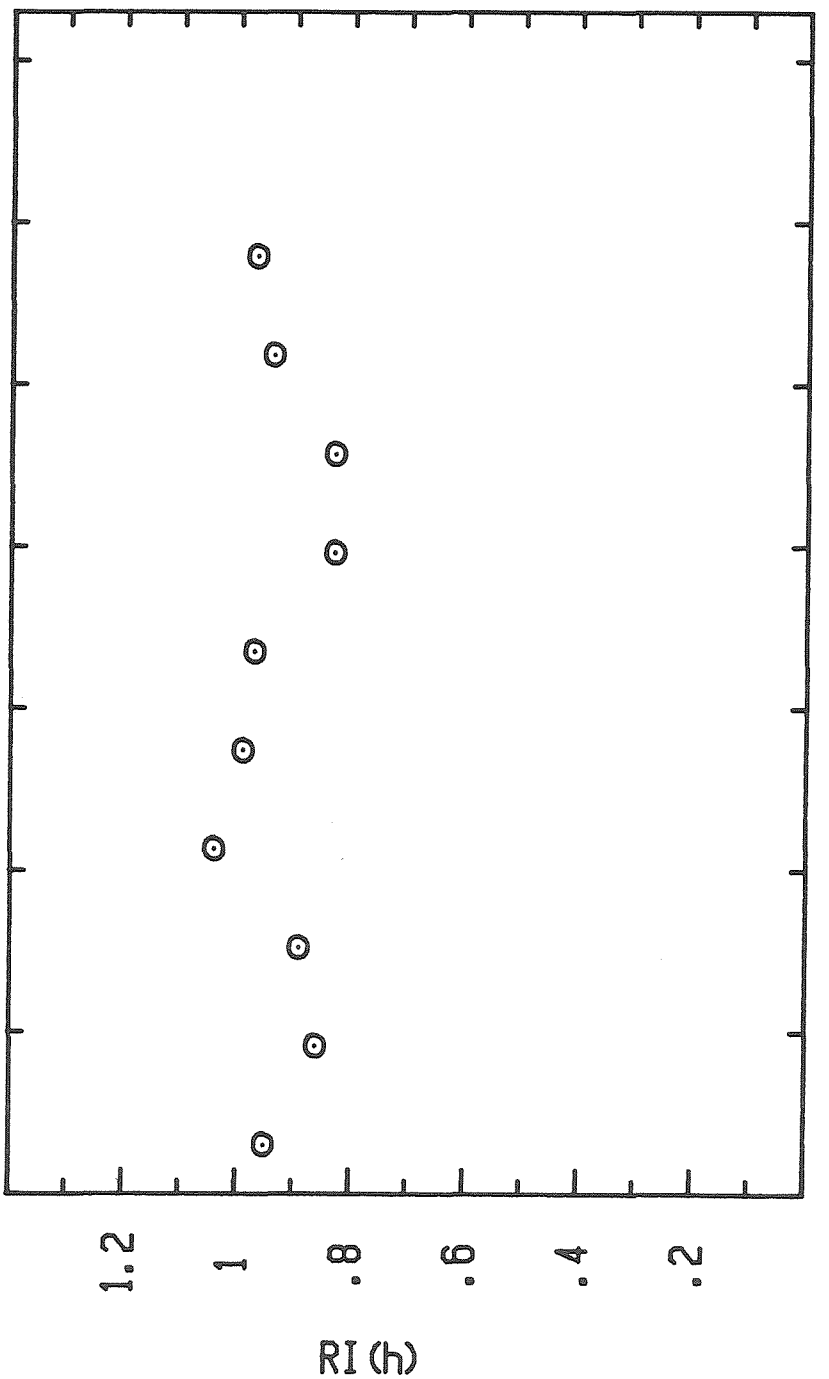

Figure 3.17 Thermal current layer Richardson number, $Ri = \frac{\Delta g h}{u^2}$, versus streamwise position, x(m), for nominal case flow.

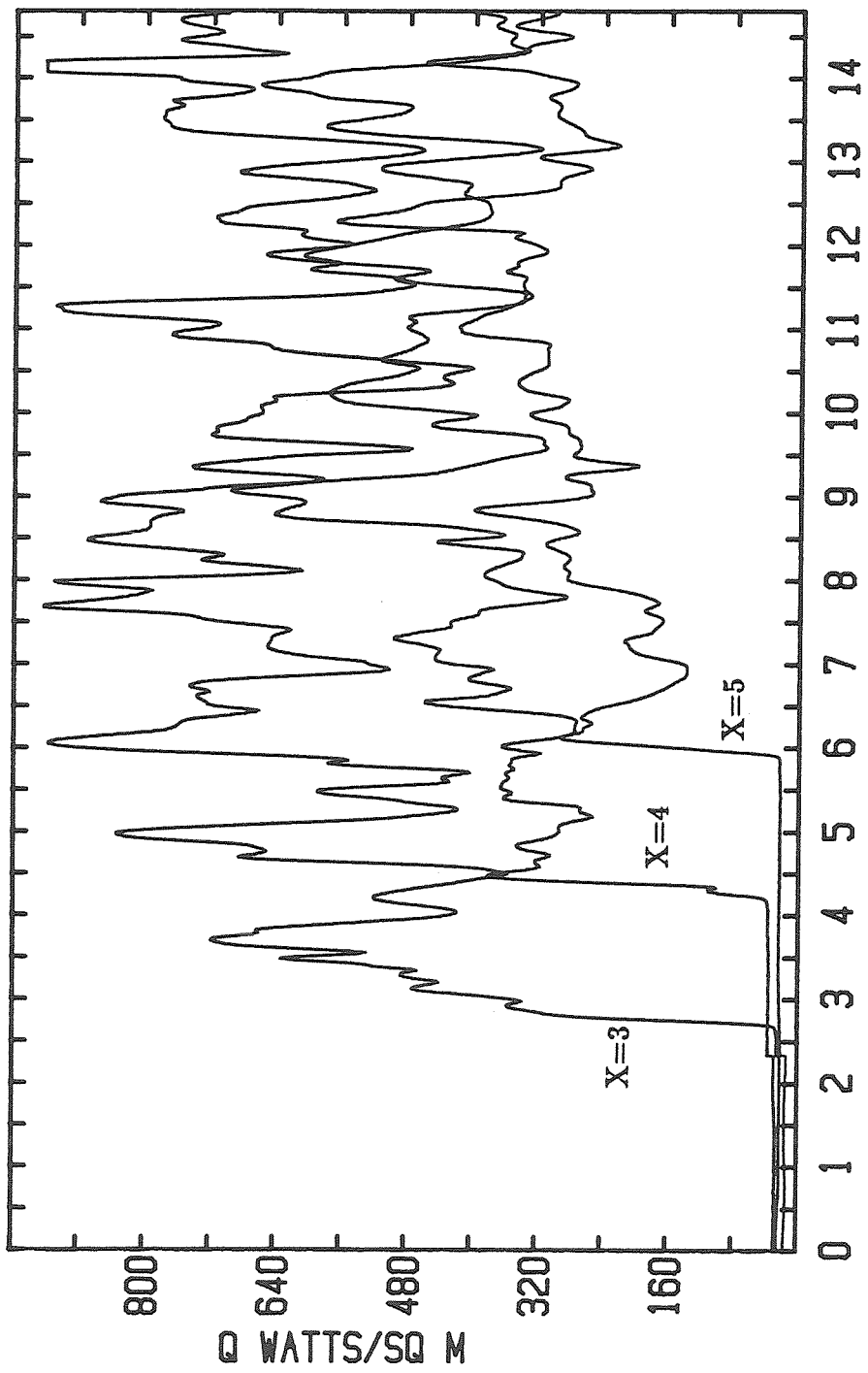

Figure 3.18 Ceiling heat flux, $q_w\,(w/m^2)$, versus time measurements for a nominal condition thermal current.

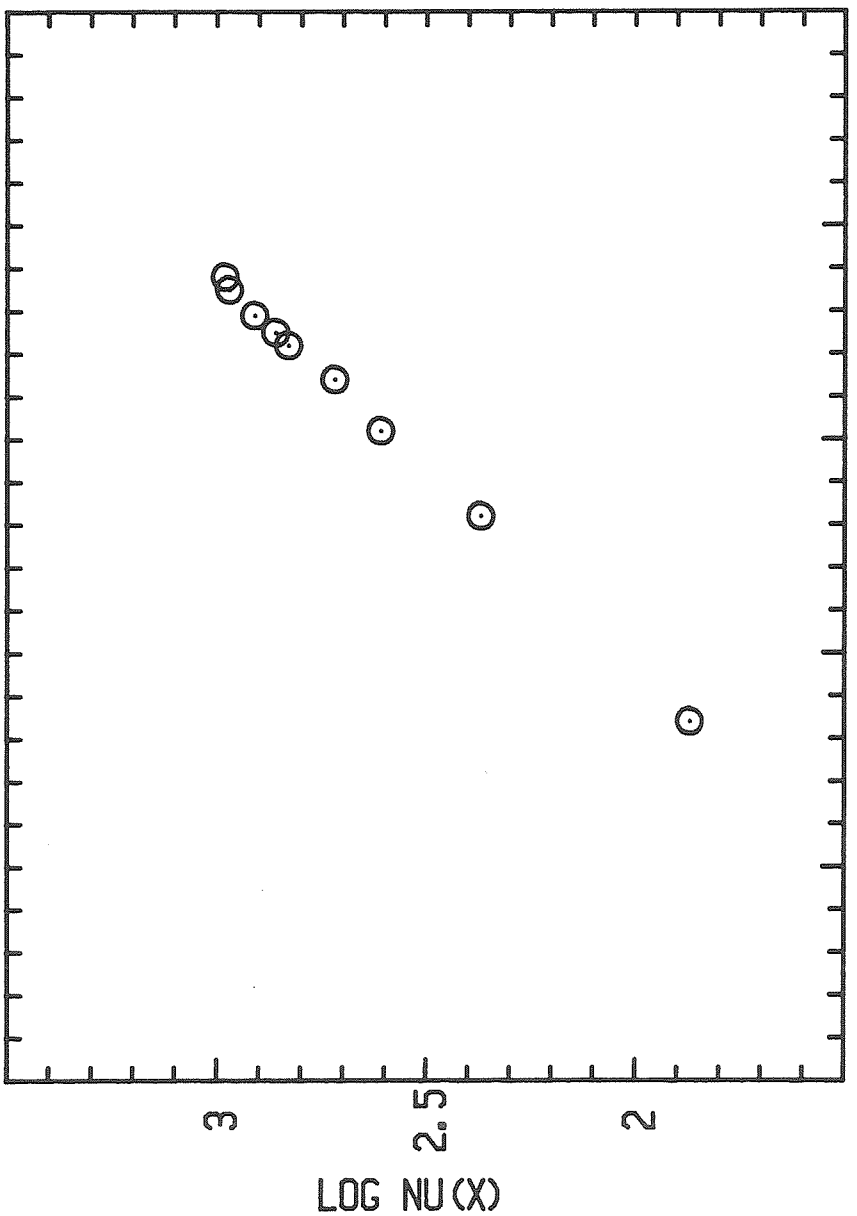

Figure 3.19 Variation of Nusselt number, $Nu_x = \frac{q_w x}{k\Delta T}$, as a function of Reynolds number, $Re_x = \frac{V x}{\nu}$, nominal condition thermal flow.

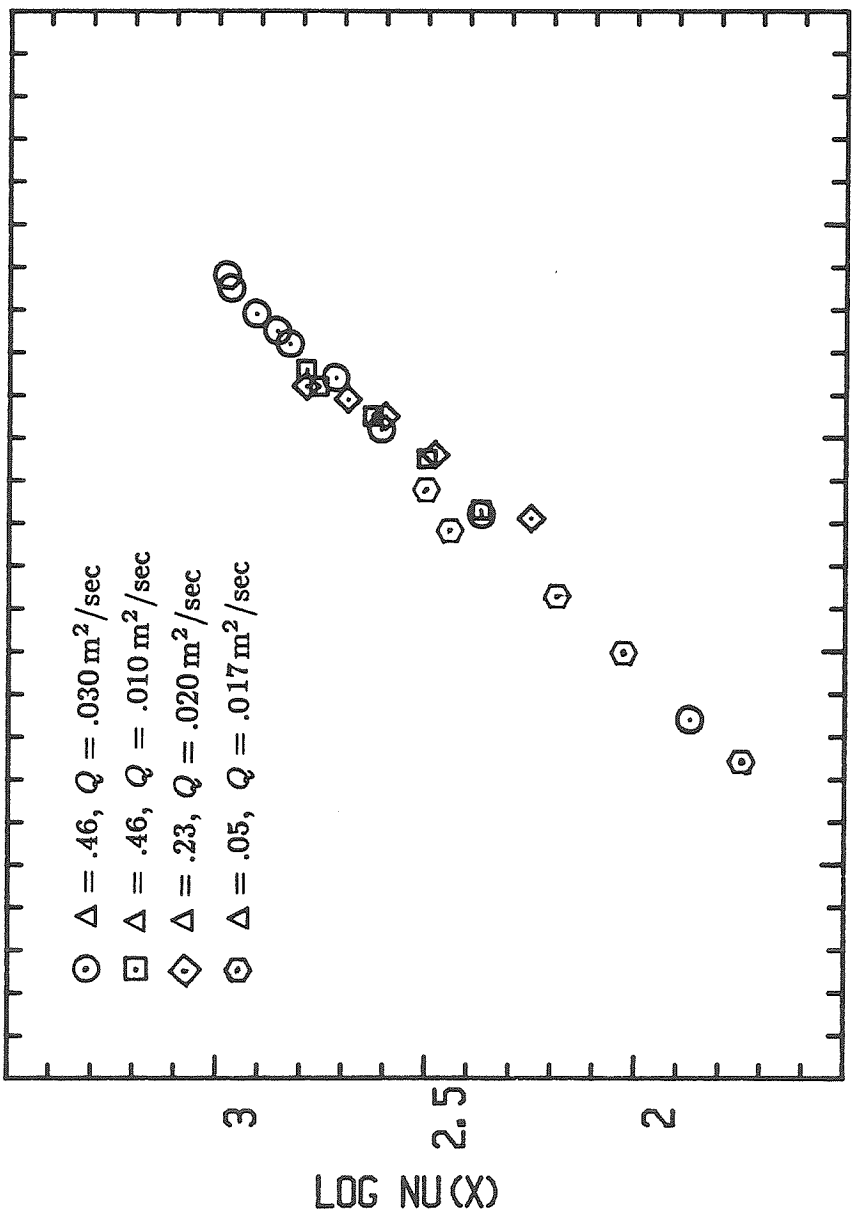

Figure 3.20 Variation of Nusselt number, $Nu_x = \frac{q_w x}{k\Delta T}$, as a function of Reynolds number, $Re_x = \frac{V_x}{\nu}$, for flows with various values of Δ and Q.

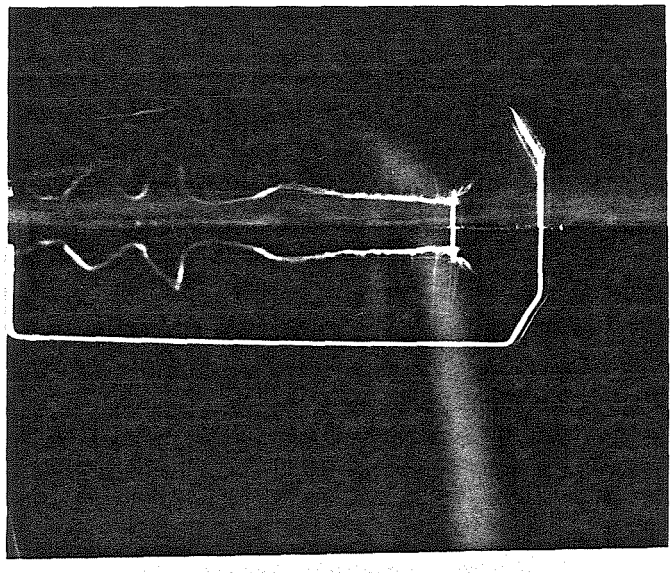

Figure 3.21 Photograph of a horizontal smoke plume, taken 100 msec after generation at X=3, Y=1 cm, for thermal flow with $\Delta = .36$ and $Q = .016\,m^2/sec$.

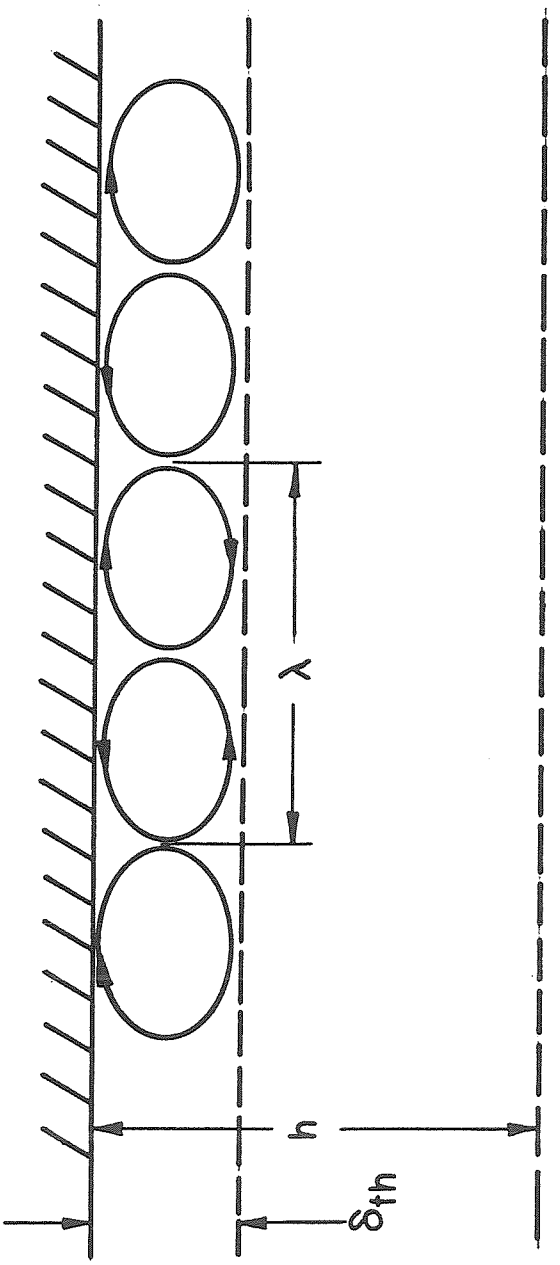

Figure 3.22 Sketch of transverse cross-section view of longitudinal convection rolls.

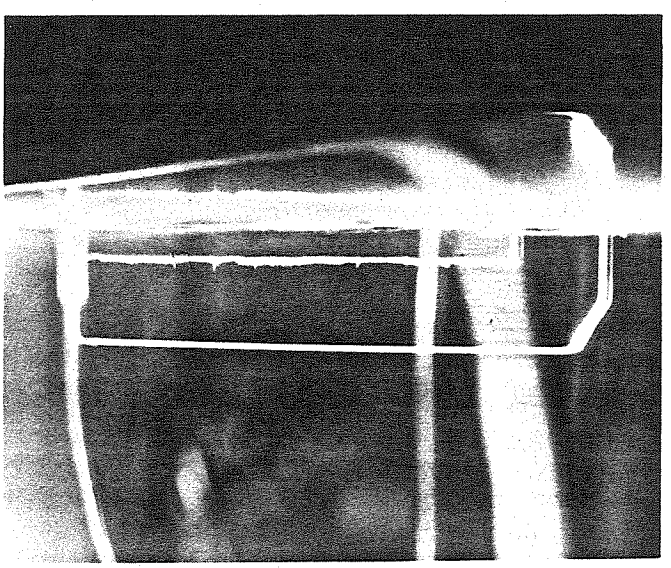

Figure 3.23 Photograph of horizontal smoke plume, taken 100 msec after generation at X=3, Y=1 cm, for adiabatic flow with $\Delta \approx .30$ and $Q \approx .015\,\mathrm{m}^2/\mathrm{sec}$.

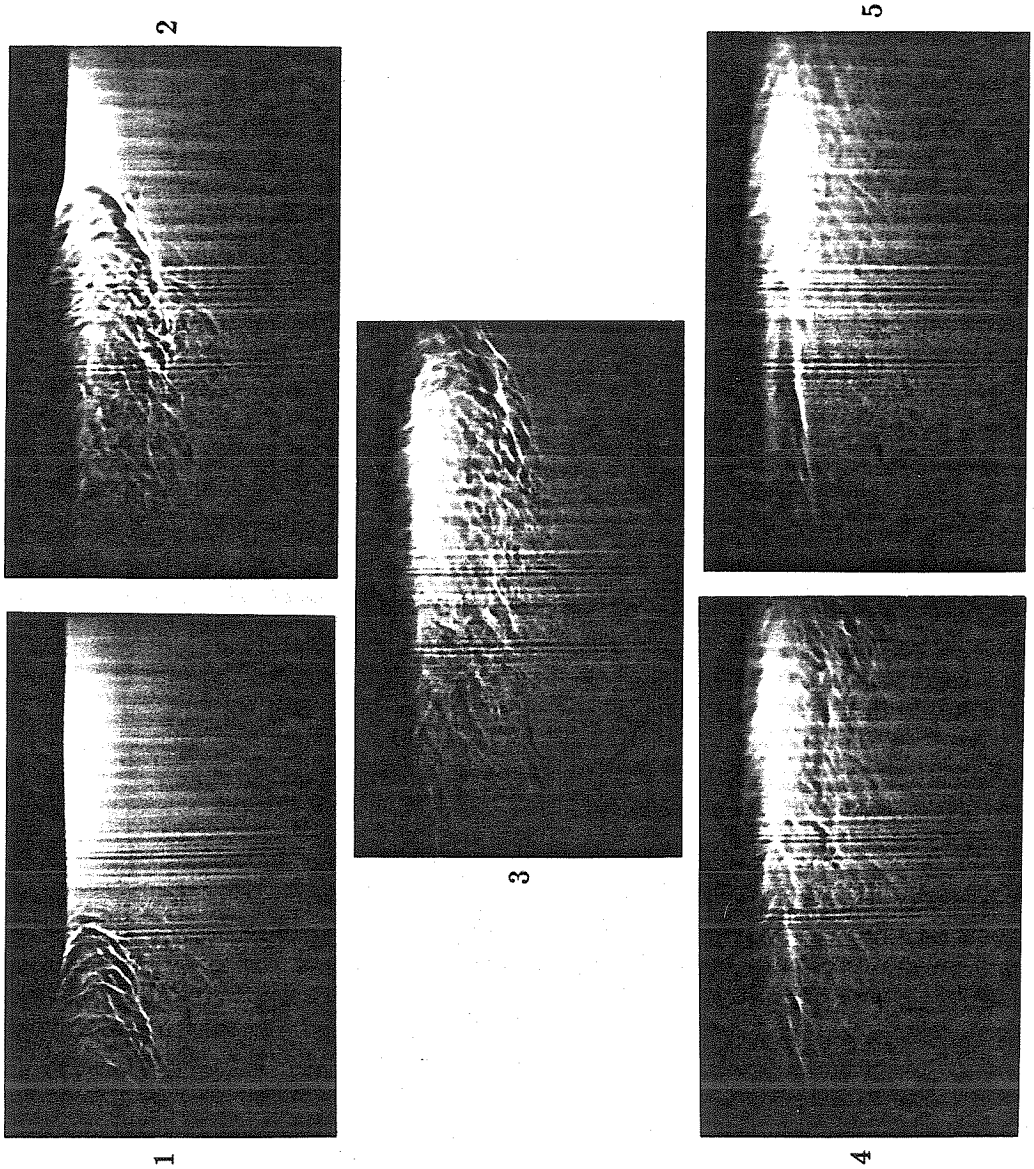

Figure 3.24 Sequence of shadowgraph photographs taken at X=2 for nominal case thermal flow.

Chapter 4

Heat Transferring Current Modeling

The following chapter pertains to the development of an analytical model for gravity current flow employing some of the empirically derived features of the flow discussed in the previous chapters. This model will help illuminate the roles heat transfer and viscous wall shear have in the determination of gravity current flow fields, and in addition, will contribute to the efforts of fire research aimed at understanding the convective processes present in building fires. During the course of the model development, empirically based assumptions will be introduced and discussed.

A steady state approximation of the local gravity current quantities is assumed since the mean velocity, temperature, and layer thicknesses measured in the thermal current experimental study indicated that these quantities did not vary appreciably during the time required for the current front to reach the test section end. The relatively small difference seen between current front spreading rate and local layer velocity profile maximum will serve as the basis for obtaining the transient current front propagation from the quasi-steady layer velocity results of the present model. Heat transfer effects in the model will be introduced in the form of convective heat transfer to the ceiling, and viscous effects will be accounted for in the form of wall shear and sidewall boundary layers. After general formulation of the model, the specific cases of heat transfer without viscous effects, and heat transfer with each of the two viscous approximations, will be examined.

4.1 General Thermal Current Equations

In the following analysis, the coordinate system of the previous discussions is retained, i.e., x refers to the streamwise direction, y the dimension positive downward from the ceiling, and z the spanwise dimension. The velocity components corresponding to these dimensions are u, v, and w, respectively. We begin by writing the steady equation of continuity for the gravity current layer:

$$\frac{\partial}{\partial x}(\rho u) + \frac{\partial}{\partial y}(\rho v) + \frac{\partial}{\partial z}(\rho w) = 0\,, \tag{4.1.1}$$

and invoking the boundary layer assumptions to equation 3.4.4, we write the x and y direction momentum equations as:

$$\frac{\partial}{\partial x}(\rho u^2) + \frac{\partial}{\partial y}(\rho uv) + \frac{\partial}{\partial z}(\rho uw) + \frac{\partial}{\partial x}(p - p_o) = \frac{\partial \tau}{\partial y}\,, \tag{4.1.2}$$

$$\frac{\partial}{\partial y}(p - p_o) = g(\rho - \rho_o)\,. \tag{4.1.3}$$

Here τ is the viscous shear stress, p_o the ambient fluid pressure, and ρ_o the ambient fluid density. All quantities are assumed to be functions of x, y, and z, unless otherwise specified, and v and w are assumed small compared to u. The equation of conservation of energy can be written in the form:

$$\frac{\partial}{\partial x}[\rho u C_p (T - T_o)] + \frac{\partial}{\partial y}[\rho v C_p (T - T_o)] + \frac{\partial}{\partial z}[\rho w C_p (T - T_o)] = \frac{\partial q}{\partial y}\,. \tag{4.1.4}$$

Finally, the equation of state for perfect gases is assumed:

$$p = \rho R T\,. \tag{4.1.5}$$

The boundary conditions imposed on the above equations are:

$$(i) \quad u, v, w = 0, \;\; T = T_w = T_o \qquad \text{at y} = 0$$

$$(ii) \quad u = 0, \;\; T = T_o \qquad\qquad \text{at y} = \delta\,.$$

In addition, q and τ are assumed to vanish at the layer edge, $y = \delta$.

Integrating equation 4.1.1 with respect to z, from $z = 0$ to $z = b$, where b is the width of the layer, and assuming u and v to be independent of z, we get:

$$b(x)\frac{\partial}{\partial x}(\rho u) + b(x)\frac{\partial}{\partial y}(\rho v) + \rho u\frac{db}{dx} = 0\,, \tag{4.1.6}$$

where the approximation:

$$w(x,y,b) = -w(x,y,0) = \frac{1}{2}u(x,y)\frac{db}{dx}\,,$$

is used. Regrouping terms in equation 4.1.6, and integrating with respect to y, from $y = 0$ to $y = \delta$, we get the result:

$$\frac{d}{dx}\left[b(x)\int_0^\delta \rho u dy\right] = 0\,, \tag{4.1.7}$$

where in addition to the boundary conditions, we have used the assumption of zero gravity current entrainment.

In an analogous manner, we get the integral form of the momentum equation:

$$\frac{d}{dx}\left[b(x)\left[\int_0^\delta \rho u^2 dy + \int_0^\delta (p - p_o)\,dy\right]\right] = -b(x)\tau_w(x) + \frac{db}{dx}\int_0^\delta (p - p_o)\,dy\,. \tag{4.1.8}$$

By integration of equation 4.1.3, using the condition that $p = p_o$ at $y = \delta$, the pressure term in equation 4.1.8 can be written in the form:

$$p - p_o = -g\int_y^\delta (\rho - \rho_o)\,dy'\,,$$

so that:

$$\int_0^\delta (p - p_o)\,dy = -g\int_0^\delta dy\int_y^\delta (\rho - \rho_o)\,dy'\,.$$

Now equation 4.1.8 can finally be written:

$$\frac{d}{dx}\left[b(x)\left[\int_0^\delta \rho u^2 dy - g\int_0^\delta dy\int_y^\delta (\rho-\rho_o)\,dy'\right]\right]$$
$$= -b(x)\tau_w(x) - \frac{db}{dx}\,g\int_0^\delta dy\int_y^\delta (\rho-\rho_o)\,dy'\,. \quad (4.1.9)$$

We have assumed here that the current layer occupies a small fraction of the channel height so that the velocity in the ambient fluid, and hence the streamwise pressure gradient in the ambient fluid, can be neglected. Finally, the integral form of the energy equation simplifies to:

$$\frac{d}{dx}\left[b(x)\int_0^\delta \rho u C_p\,(T-T_o)\,dy\right] = -b(x)q_w(x)\,. \quad (4.1.10)$$

Since the density variations are often large in the thermal current flow, and for the purpose of simplifying the above equations to their incompressible forms, the Howarth transformation of the vertical length scale is used:

$$\rho dy = \rho_o dy_i\,,$$
$$y_i = \int_0^y \frac{\rho}{\rho_o}dy' = \int_0^y \frac{T_o}{T}dy'\,. \quad (4.1.11)$$

We assume velocity and temperature profiles of the form:

$$\frac{u}{u_m(x)} = U(\eta)\,,$$
$$\frac{T-T_o}{T_m(x)-T_o} = \Theta(\eta)\,,$$
$$\eta = \frac{y_i}{\delta_i}\,, \quad (4.1.12)$$

where $u_m(x)$ and $T_m(x)$ are the local velocity and temperature maximum values, and the profiles U and Θ can be approximated by the same function for this case of Pr close to one:

$$\Theta(\eta) = U(\eta) = \begin{cases} a\eta(1-\eta)^4, & \text{for } 0 \le \eta \le 1; \\ 0, & \text{for } \eta \ge 1. \end{cases} \quad (4.1.13)$$

The value of a is such that $U_{max} = \Theta_{max} = 1$, i.e., $a = 5(5/4)^4$. This profile function closely follows the features of the experimentally determined profiles, where the value of δ_i is related to h, the minimum slope thickness of the profile shapes in the non-transformed y coordinate system. The details of the analytic computation of δ_i from h are given in appendix C, but for our purposes a simpler empirically deduced relationship is suitable. We assume h to be independent of whether temperature or velocity profiles are used for its calculation. Comparing the transformed experimental temperature profile data at several values of x with the results from equation 4.1.13 shows reasonable agreement, when using the following empirically based relation for δ_i:

$$\delta_i = \frac{3}{2} \frac{h}{1 + \frac{2}{3}\left(\frac{T_m - T_o}{T_o}\right)} . \tag{4.1.14}$$

Substituting the profile assumptions and transformation into the integral equations, and defining integral constants, produces the following set of results:

$$b(x) C_1 \rho_o u_m \delta_i = \dot{m}_o = \text{constant} , \tag{4.1.15}$$

$$\frac{d}{dx}\left[b(x)\left[C_2 \rho_o u_m^2 \delta_i + C_3 g \rho_o \delta_i^2 \left(\frac{T_m - T_o}{T_o}\right)\left(1 + C_4\left(\frac{T_m - T_o}{T_o}\right)\right)\right]\right]$$
$$= -b(x)\tau_w(x) + C_3 g \rho_o \delta_i^2 \left(\frac{T_m - T_o}{T_o}\right)\left(1 + C_4\left(\frac{T_m - T_o}{T_o}\right)\right)\frac{d}{dx}b(x) , \tag{4.1.16}$$

$$\frac{d}{dx}\left[b(x) C_2 \rho_o u_m \delta_i C_p (T_m - T_o)\right] = -b(x) q_w(x) , \tag{4.1.17}$$

where the integral constants are defined in the following relations:

$$\int_0^\delta \rho u dy = C_1 \rho_o u_m \delta_i ,$$

$$\int_0^\delta \rho u^2 dy = C_2 \rho_o {u_m}^2 \delta_i ,$$

$$\int_0^\delta \rho u\,(T - T_o)\,dy = C_2 \rho_o u_m (T_m - T_o)\delta_i\,,$$

$$\int_0^\delta dy \int_y^\delta (T - T_o)\,dy' = C_3 (T_m - T_o){\delta_i}^2\,,$$

$$\int_0^\delta (T - T_o)\,dy \int_y^\delta (T - T_o)\,dy' = C_3 C_4 (T_m - T_o)^2 {\delta_i}^2\,.$$

For the profile assumption given in equation 4.1.13, the values of these constants are calculated to be:

$$C_1 = \frac{a}{30}\,,\quad C_2 = \frac{a^2}{495}\,,\quad C_3 = \frac{a}{105}\,,\quad and\,,\quad C_4 = \frac{7a}{120}\,.$$

For the terms $q_w(x)$ and $\tau_w(x)$ in the above set of equations, we use our empirical results for Nu_x, and Reynolds' analogy. Equation 3.4.13 implies that:

$$\begin{aligned} q_w &= C_H \frac{k}{\nu} u_m (T_m - T_w)\,, \\ \tau_w &= \frac{C_f}{2} \rho u_m^2\,, \end{aligned} \tag{4.1.18}$$

while Reynolds' analogy states that:

$$C_f = 2C_H = 2\frac{Nu_x}{Re_x Pr} = \frac{2(.013)}{Pr} \approx .037\,. \tag{4.1.19}$$

For the constant wall temperature heat transfer of our thermal flows, $T_w = T_o$. The temperature dependence of term k/ν in equation 4.1.18 can be approximated to be:

$$\frac{k}{\nu} = \frac{\rho C_p \alpha}{\nu} = \frac{\rho C_p}{Pr} \propto \frac{1}{T}\,,$$

since in the last ratio only ρ is a strong function of temperature. Furthermore, the width of the layer, $b(x)$, can be approximated by the expression:

$$b(x) = \mathrm{w} - 2\delta_1 = \mathrm{w} - C_5 \sqrt{\frac{\nu x}{u_m}}\,, \tag{4.1.20}$$

where w is the width of the channel and equation 2.4.7 is used for the sidewall displacement thickness, δ_1.

The above system of equations, with unknowns u_m, δ_i, and T_m, can now be simplified to the form:

$$\frac{d\vartheta}{dx} = -\frac{C_H}{C_2 Pr}\frac{T_o}{T_f}\frac{\vartheta}{\delta_i}, \tag{4.1.21}$$

$$\frac{du_m}{dx} = -\frac{\mathcal{N}(u_m, \delta_i, \vartheta)}{\mathcal{D}(u_m, \delta_i, \vartheta)}, \tag{4.1.22}$$

and,

$$\delta_i = \frac{1}{C_1}\frac{\dot{m}_o}{\rho_o u_m b(x)}, \tag{4.1.23}$$

where:

$$\vartheta = \frac{T_m - T_o}{T_o},$$

$$\mathcal{D}(u_m, \delta_i, \vartheta) = 1 - 2\frac{C_3}{C_2}\frac{g\delta_i}{u_m^2}\vartheta(1 + C_4\vartheta)\left(1 + \frac{C_5}{2b}\sqrt{\frac{\nu x}{u_m}}\right),$$

$$\mathcal{N}(u_m, \delta_i, \vartheta) = \frac{1}{2}\frac{C_f}{C_2}\frac{u_m}{\delta_i} + \frac{C_5 C_3}{C_2}\frac{g\delta_i}{u_m b}\sqrt{\frac{\nu}{u_m x}}\vartheta(1 + C_4\vartheta)$$

$$+\frac{C_3}{C_2}\frac{g\delta_i}{u_m}\left[1 + 2C_4\vartheta + C_5\frac{T_o}{\nu}\frac{d\nu}{dT_f}\frac{dT_f}{dT_m}\frac{x}{b}\sqrt{\frac{\nu}{u_m x}}\vartheta(1 + C_4\vartheta)\right]\frac{d\vartheta}{dx},$$

and ν is the kinematic viscosity evaluated at the film temperature,

$$T_f = \frac{T_m + T_o}{2}.$$

4.2 Solutions to the Equations

In this section, the solution to the above equations is examined, and an assumption of critical flow is introduced. The solution is then compared to experimental results. The effects of the sidewall boundary layer correction will not be considered in this section, i.e., the constant C_5 is set to zero. We begin by first examining the inviscid solution to the equations presented at the end of the previous

section. By setting both C_f and C_5 equal to zero (no wall shear stress, and $b(x)$ = w= constant), the solution can be examined in the following manner:

From equation 4.1.23, we write:

$$u_m \delta_i = u_o \delta_o \,,$$

$$u_o = u_m(x_o), \quad \delta_o = \delta_i(x_o) \,,$$

where x_o represents the streamwise coordinate of the initial conditions (for comparison to experiment, we let x_o be the location of the first downstream measuring station). Equations 4.1.21 and 4.1.22 can then be written:

$$\frac{du_m}{dx} = -\frac{\mathcal{N}_o(u_m, \vartheta)}{\mathcal{D}_o(u_m, \vartheta)} \,,$$

where:

$$\mathcal{N}_o = \frac{C_3}{C_2} \frac{g\delta_o}{u_o} \left(\frac{u_o}{u_m}\right)^2 (1 + 2C_4\vartheta) \frac{d\vartheta}{dx}$$

$$\mathcal{D}_o = 1 - 2\frac{C_3}{C_2} \frac{g\delta_o}{{u_o}^2} \left(\frac{u_o}{u_m}\right)^3 \vartheta(1 + C_4\vartheta) \,.$$

Hence,

$$\frac{1}{u_o} \frac{du_m}{d\vartheta} = \frac{\frac{C_3}{C_2} \frac{g\delta_o}{u_o^2} (1 + 2C_4\vartheta) \frac{u_m}{u_o}}{2\frac{C_3}{C_2} \frac{g\delta_o}{u_o^2} \vartheta(1 + C_4\vartheta) - \left(\frac{u_m}{u_o}\right)^3} \,. \tag{4.2.1}$$

Figure 4.1 illustrates the family of solutions described by equation 4.2.1, with a curve passing through the points of infinite slope indicated as the critical solution found from $\mathcal{D}_o$=0. The horizontal line through $U_m/U_o = 1$ denotes the locus of initial condition points, ϑ_o, for the fixed values of u_o and δ_o. The solution for increasing x will proceed up or down a specific solution curve passing through the corresponding initial condition point, depending on whether the initial condition falls in the supercritical or subcritical flow region, as indicated in the figure.

Inclusion of the wall shear stress term ($C_f \neq 0$) into the velocity gradient equation changes this solution behavior. Integration of equations 4.1.21 and 4.1.22 with respect to x, from the initial upstream location, in this case reveals discontinuities, analogous to hydraulic jumps, in the solution curves represented in figure 4.1. These jumps invariably lead to infinitely large values of the derivatives and failure of the integration scheme. Consequently, another approach to the solution of the equations is taken. Since the solution method described above is observed to approach the critical solution before becoming unstable and blowing up, a solution assuming the approximation of critical flow for all x is attempted.

Integration of equation 4.1.21 using a fourth order Runge-Kutta scheme (White, 1974), while using the critical condition from equation 4.1.22 (the denominator of the expression going to zero), gives the solution for a flow critical at all streamwise positions. This solution gives remarkably good agreement with experiment, the extent of which can be seen in figures 4.2, 4.3, and 4.4, which present the results of the critical inviscid solution of the equations. In this example, the nominal initial conditions of $\Delta = .46$ and $\dot{m}_o = .0093\,\mathrm{kg/sec}$ are used, and the circled points in the figures represent the experimentally measured values of local temperature maxima, front velocities, and layer thicknesses. The step size used for integration is $\Delta x = .05\,\mathrm{meters}$. While figures 4.2 and 4.4 show close agreement between calculations and measurements, figure 4.3 shows the calculated layer velocities (and front velocities, under our assumptions) to be about 10% greater than the measured front velocities for low values of x. This result is consistent with the experimental observations reported in section 3.4.2 concerning the relationship between the layer velocity profile maximum and the front velocity at a particular x location.

Another such comparison between calculations and observations, for the initial parameters $\Delta = .36$ and $\dot{m}_o = .007\,\mathrm{kg/sec}$, appears in figures 4.5, 4.6, and 4.7. This reduced buoyancy flux example demonstrates agreement comparable to that in the nominal case discussed above.

Since the Richardson number of the gravity current layer was experimentally observed to be near one, implying an approximately critical value of Froude number, it is not surprising that the critical flow approximation produces good agreement of the model with the measurements. The gravity current flowing along the ceiling, spilling out of the channel end, can in a sense be considered analogous to the hydraulic flow over a broad crested weir, which is critical throughout its length.

4.3 Sidewall Viscous Effects

Retaining the $\frac{db}{dx}$ term ($C_5 \neq 0$) in the original formulation of the equations does not significantly affect their solution for the nominal case, as can be seen in figures 4.8, 4.9, and 4.10, which represent the solution for the nominal case flow with the sidewall boundary layers accounted for. As estimated in section 3.4.4, the sidewall displacement layers occupy a fraction of the spanwise dimension of the order 10% for the nominal case flow, so that the increases in layer thicknesses and velocities introduced by their consideration are thus small. These increases can be seen in figures 4.9 and 4.10, and figure 4.8 shows a slightly greater decrease in temperature with x increase. This latter effect is attributed to the heat transfer coefficient's dependence on local velocity, which appears in the model as the u_m term in the heat flux expression of equation 4.1.18.

4.4 Skin Friction Effect

Since the assumption of critical flow in the layer, made in section 4.2, does

not incorporate wall shear stress in its formulation (C_f does not appear in the expression $\mathcal{D}_o = 0$), a perturbation scheme is used to examine the effects of wall shear stress on the model flow. Equation 4.1.22, for the velocity gradient, can be expressed in the form (for a given mass flux):

$$\frac{du_m}{dx} = -\frac{\mathcal{N}(x, u_m, \vartheta)}{\mathcal{D}(x, u_m, \vartheta)},$$

and for the case of no sidewall correction ($C_5 = 0$), in the form:

$$\frac{du_m}{dx} = -\frac{\mathcal{N}(u_m, \vartheta)}{\mathcal{D}(u_m, \vartheta)}. \tag{4.4.1}$$

The critical condition,

$$\mathcal{D}(u_m, \vartheta) = 0, \tag{4.4.2}$$

implies an inviscid result for u_m as a function f of ϑ:

$$u_m^o = f(\vartheta). \tag{4.4.3}$$

Assuming that the wall friction perturbs this velocity by the quantity u':

$$u_m = u_m^o + u', \quad |u'| << u_m^o, \tag{4.4.4}$$

we can now write equation 4.4.1 as:

$$\mathcal{D}(u_m^o + u', \vartheta)\frac{d}{dx}(u_m^o + u') = -\mathcal{N}(u_m^o + u', \vartheta). \tag{4.4.5}$$

Expanding the terms $\mathcal{D}$ and $\mathcal{N}$ in equation 4.4.5 using a Taylor series about (u_m^o, ϑ), and using equation 4.4.2, we get:

$$-\frac{\partial}{\partial u_m}\left[\mathcal{D}(u_m^o, \vartheta)\right] u' \frac{du_m^o}{dx} \approx \mathcal{N}(u_m^o, \vartheta) + \frac{\partial}{\partial u_m}\left[\mathcal{N}(u_m^o, \vartheta)\right] u', \tag{4.4.6}$$

which solving for u', gives:

$$u' = \frac{-\mathcal{N}(u_m^o, \vartheta)}{\frac{\partial}{\partial u_m}\left[\mathcal{D}(u_m^o, \vartheta)\right]\frac{du_m^o}{dx} + \frac{\partial}{\partial u_m}\left[\mathcal{N}(u_m^o, \vartheta)\right]}. \tag{4.4.7}$$

In the nomenclature of equation 4.1.22, this expression for u' can be written as:

$$u' = \frac{-\frac{1}{2}\frac{C_f C_1}{C_2}\frac{\rho_o w}{\dot{m}_o}u_m^2 + \frac{C_3 C_H}{C_2^2 Pr}g\vartheta(1+2C_4\vartheta)\frac{T_o}{T_f}\frac{1}{u_m}}{6\frac{C_3}{C_2 C_1}\vartheta(1-C_4\vartheta)\frac{\dot{m}_o g}{\rho_o w}\frac{1}{u_m^4}\frac{du_m^o}{dx} + \frac{C_f C_1}{C_2}\frac{\rho_o w}{\dot{m}_o}u_m + \frac{C_3 C_H}{C_2^2 Pr}g\vartheta(1+2C_4\vartheta)\frac{T_o}{T_f}\frac{1}{u_m^2}}, \tag{4.4.8}$$

where:

$$\frac{du_m^o}{dx} = -\frac{2}{3}\frac{C_3 C_H}{C_2^2 Pr}g\vartheta(1+2C_4\vartheta)\frac{T_o}{T_f}\frac{1}{u_m},$$

using equation 4.1.21 for $\frac{d\vartheta}{dx}$.

Solving the model equations for the nominal case, including this perturbation velocity u', gives the results presented in figures 4.11, 4.12, and 4.13. In comparison to the inviscid case, these results show a more substantial reduction in u_m with increasing x, and correspondingly lower levels of heat transfer. The layer thickness increased even more with x, as specified by mass conservation in light of the more rapid decrease in u_m.

4.5 Conclusion

Application of the above analysis to adiabatic flows requires recomputation of the constants C_1, C_2, C_3, and C_4 using the uniform temperature profile and thicker boundary layer velocity profile of the adiabatic case. An isothermal temperature profile gives a monotonically increasing density for increasing y, as opposed to the inversion seen in the thermal current temperature profile, where the density decreases for increasing y in the thermal boundary layer. For the simple case of a uniform velocity and density profile (a homogeneous layer approximation) in an adiabatic, inviscid flow, the governing equations reduce to the constant velocity result:

$$u = (g\,\Delta\,Q)^{1/3},$$

or,

$$C = 1,$$

equivalent to the spreading rate results for the constant velocity adiabatic flow regime obtained in section 2.4. Although more accuracy can be obtained by using a non-uniform velocity profile similar to those measured experimentally, the assumption of uniform density in the layer should closely reproduce the actual density profile since essentially no mixing was observed at the current layer interface.

Thus, the integral model scheme developed above, under the assumptions of zero gravity current layer entrainment and quasi-steadiness, employing our experimentally derived heat transfer relation and the critical flow assumption, gives good agreement with our measurements. The sidewall boundary layer correction did not significantly affect the nominal case solution, and since applications such as building fire gravity currents will have even greater Reynolds numbers (but lower layer cross-section aspect ratios), this correction does not justify its complication to the model formulation. Similarly, for buoyant-inertially dominated flows such as these, inclusion of wall shear stress effects did not substantially alter the model results, and can also be neglected in a basic model scheme. It is suspected that the relative difference between the local layer velocity profile maximum and current front velocity may increase for higher Reynolds number flows, although the Reynolds number dependence of the magnitude of the relative inflow into the current head, Q_1/Q, is not fully understood. For reference, a sample model Fortran code and integration routine appear in appendix D.

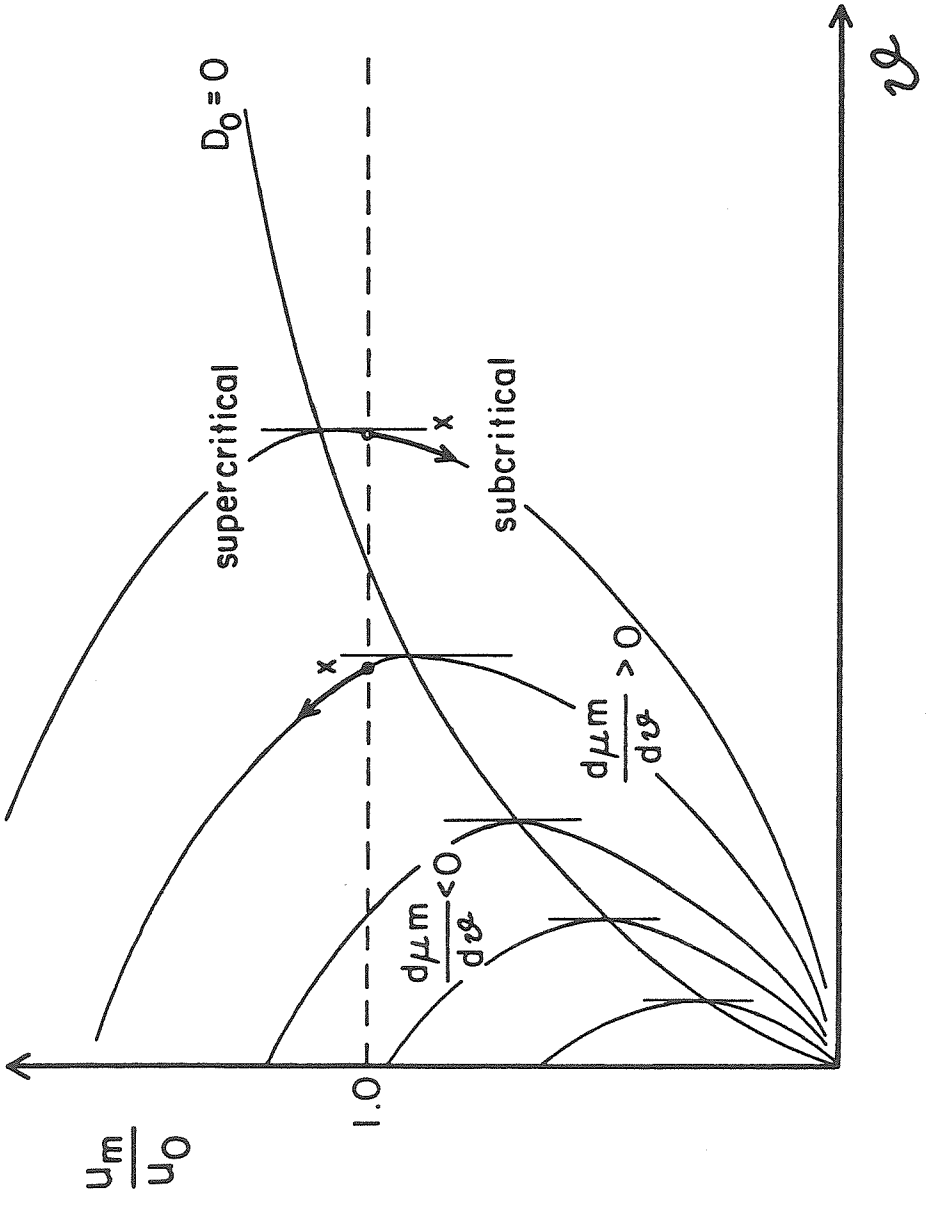

Figure 4.1 Inviscid model solution behavior.

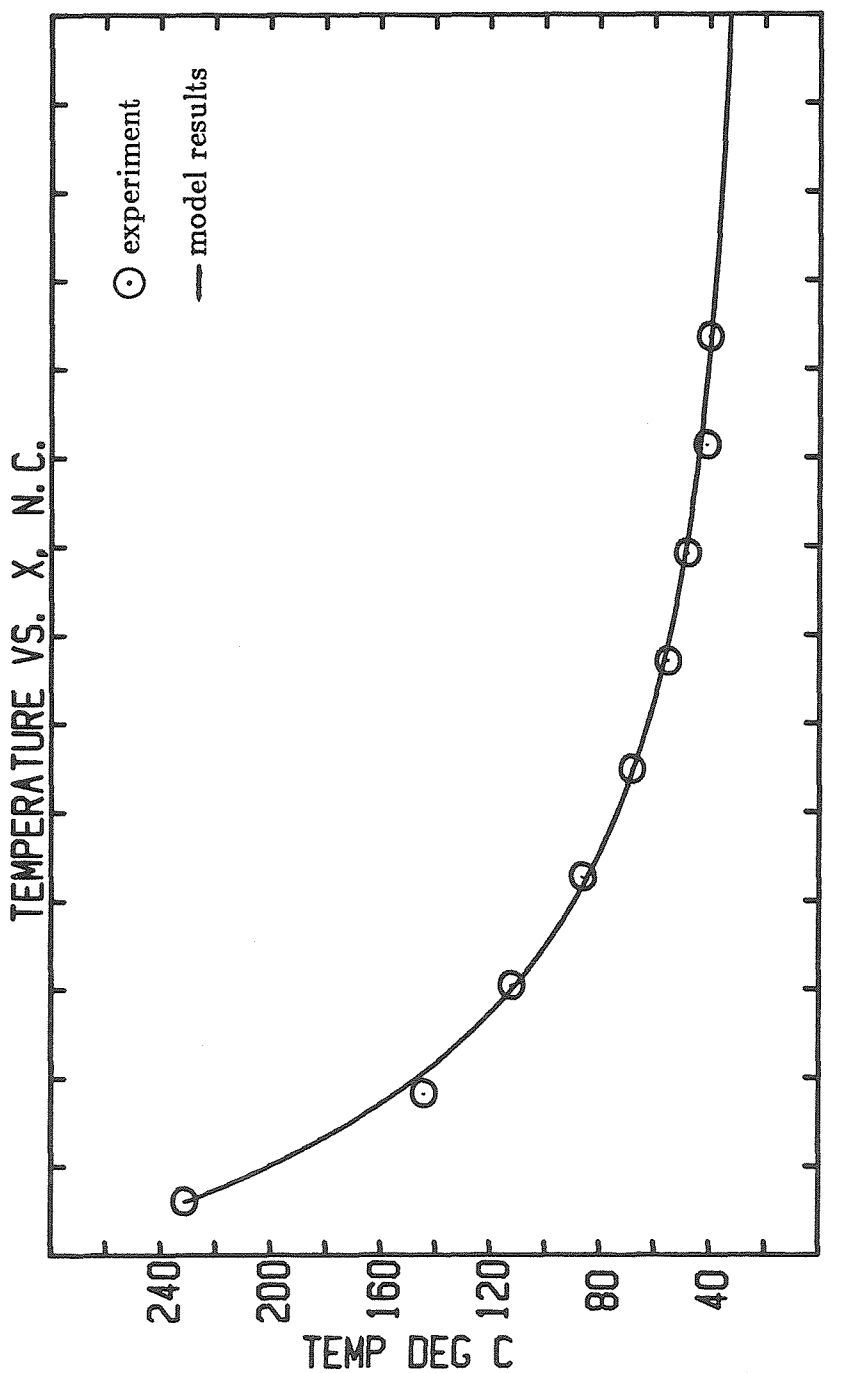

Figure 4.2 Comparison of critical solution with measurements, $T(^\circ\,\mathrm{C})$ versus $x(\mathrm{m})$, for nominal case thermal flow.

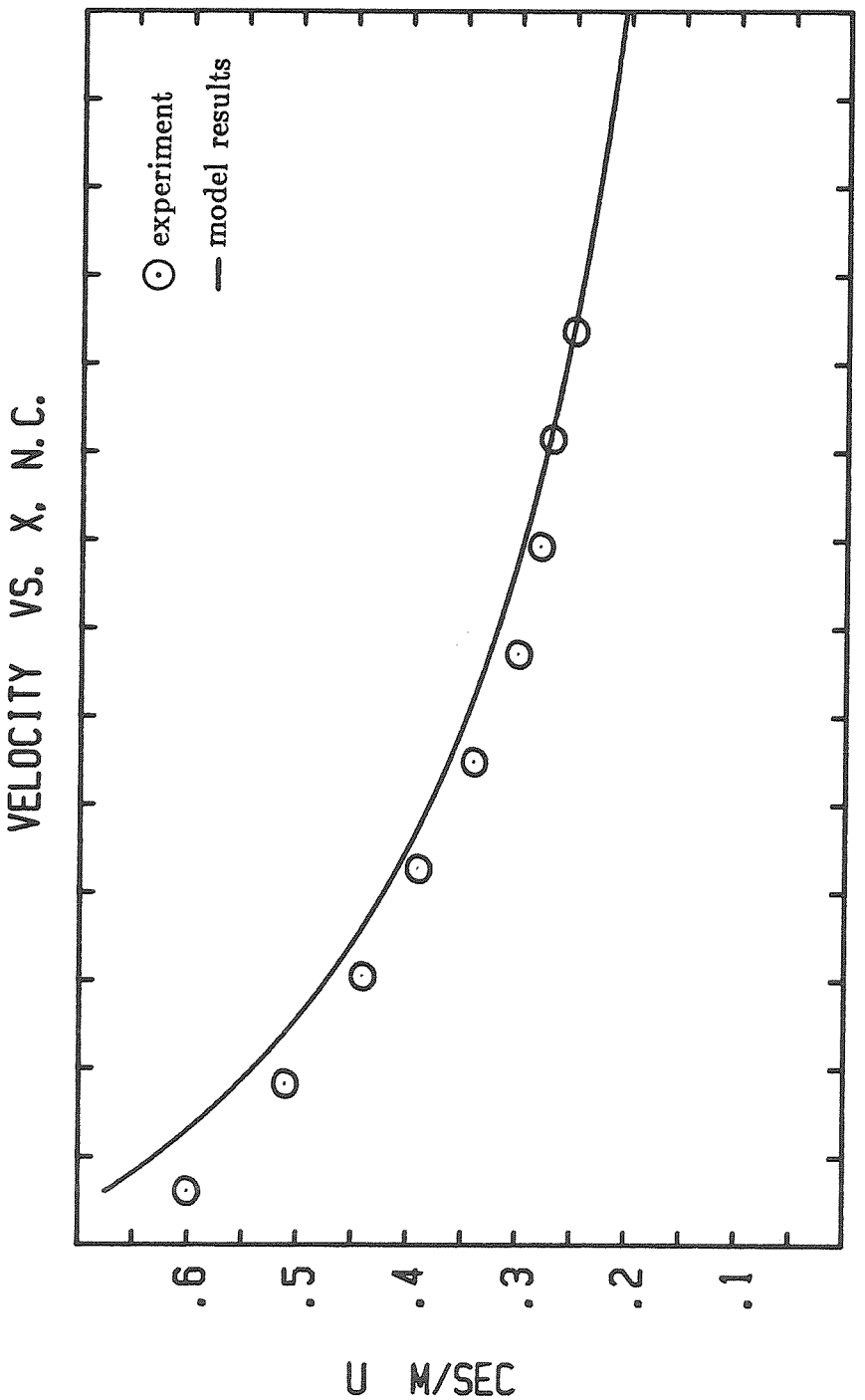

Figure 4.3 Comparison of critical solution with measurements, u(m/sec) versus x(m) for nominal case thermal flow.

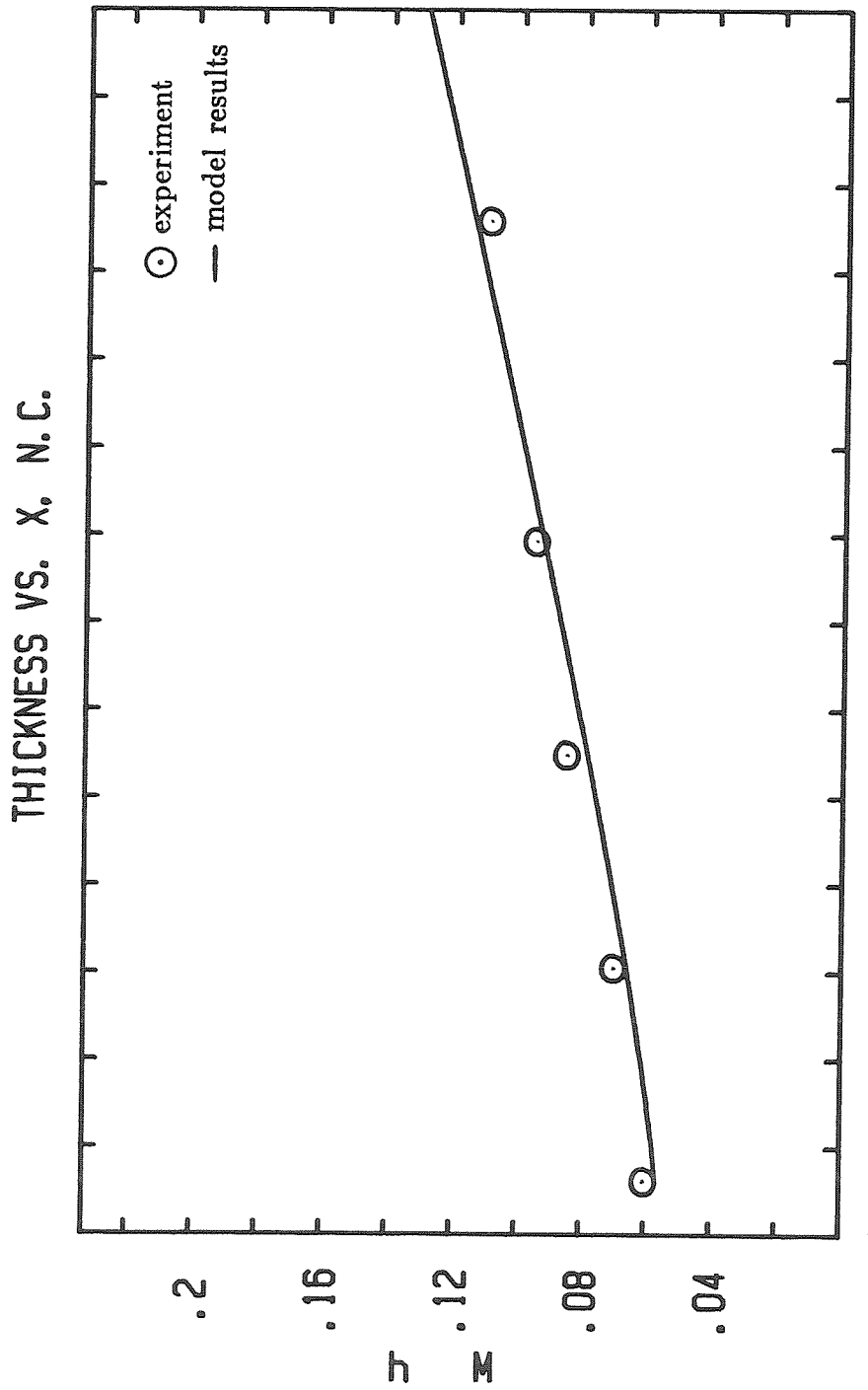

Figure 4.4 Comparison of critical solution with measurements, h(m) versus x(m) for nominal case thermal flow.

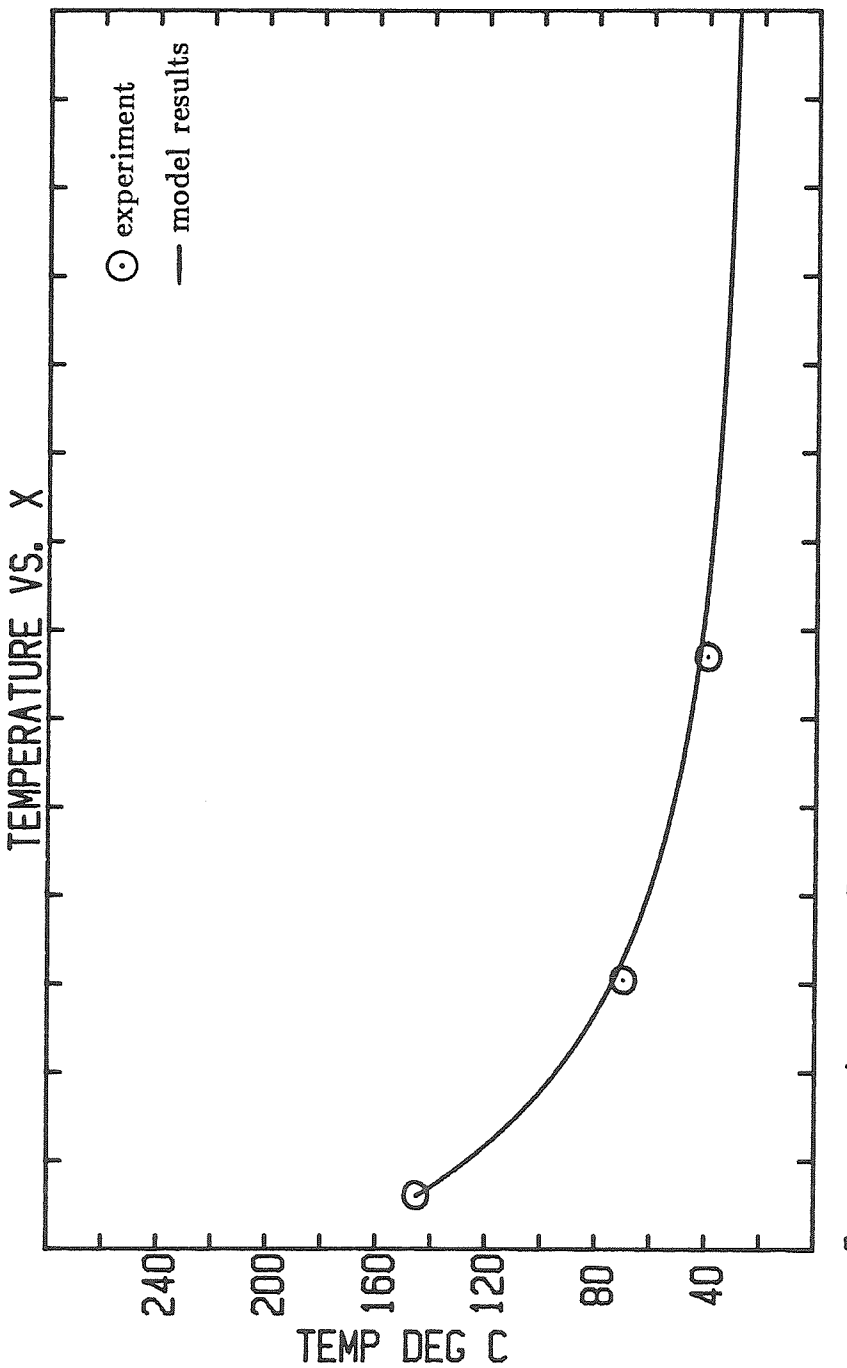

Figure 4.5 Comparison of critical solution with measurements, $T(^\circ\,\mathrm{C})$ versus $x(\mathrm{m})$, for thermal flow with $\Delta = .36$ and $Q = .019\,\mathrm{m}^2/\mathrm{sec}$.

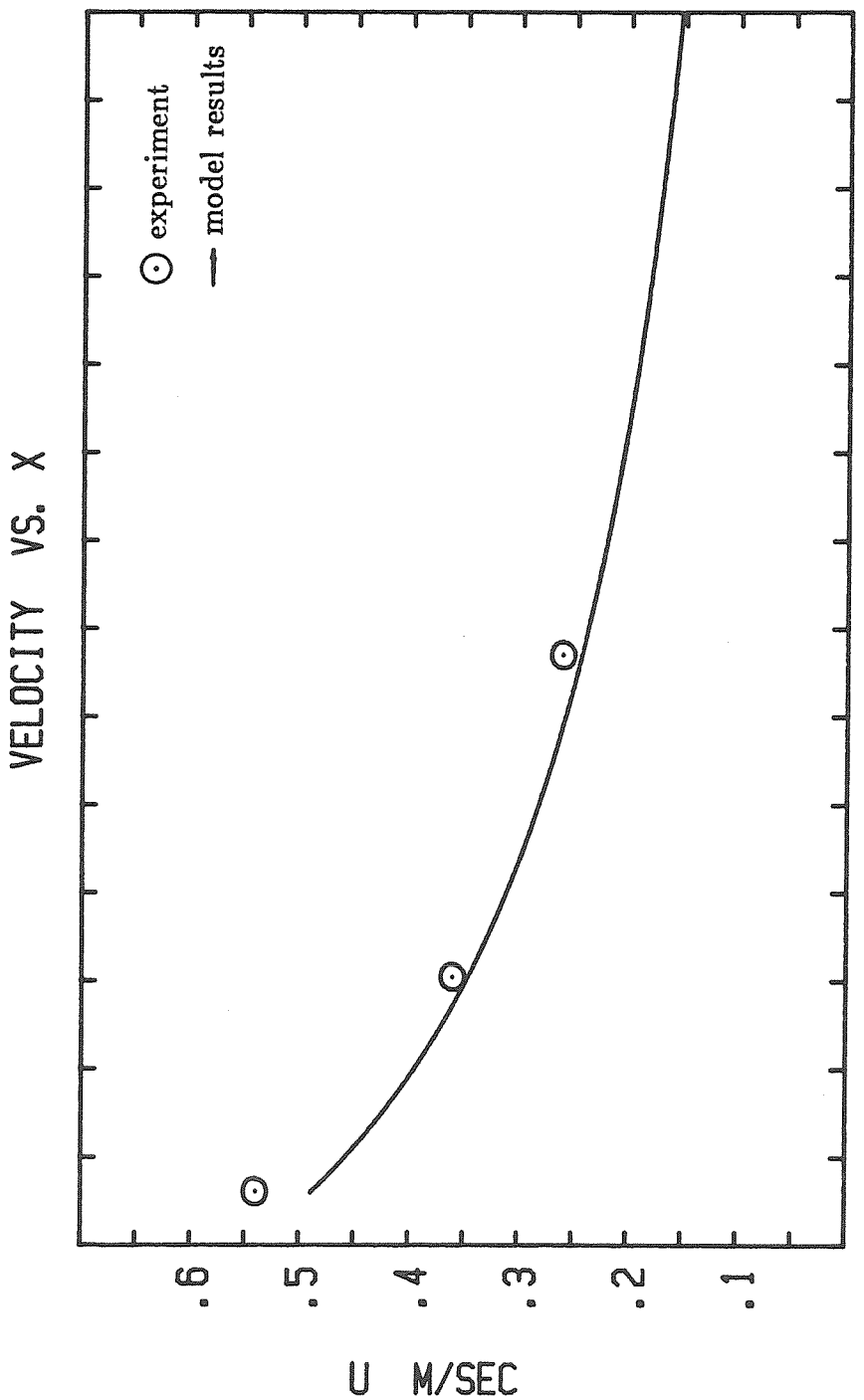

Figure 4.6 Comparison of critical solution with measurements, u(m/sec) versus x(m), for thermal flow with $\Delta = .36$ and $Q = .019\,\mathrm{m}^2/\mathrm{sec}$.

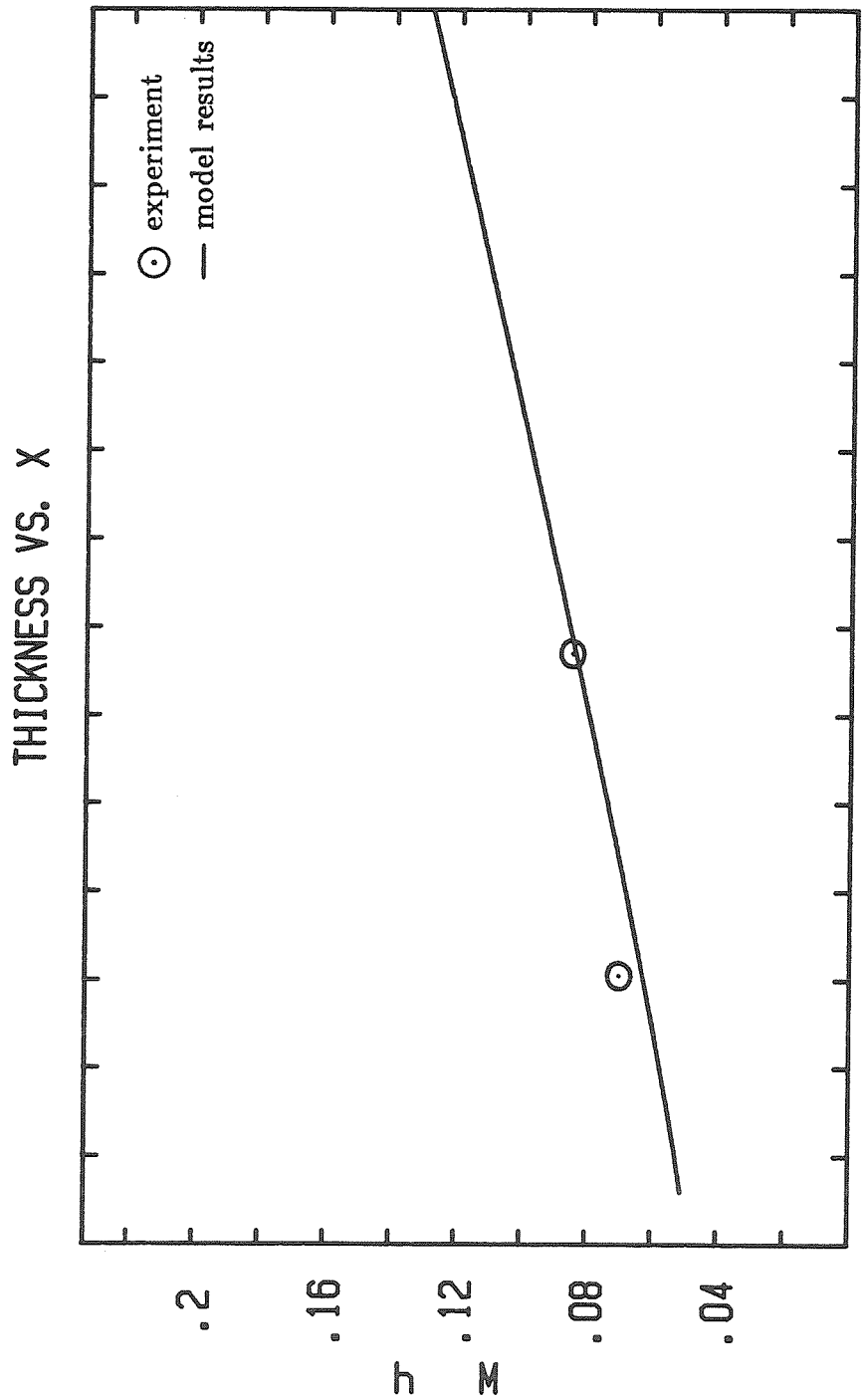

Figure 4.7 Comparison of critical solution with measurements, $h(\mathrm{m})$ versus $x(\mathrm{m})$, for thermal flow with $\Delta = .36$ and $Q = .019\,\mathrm{m}^2/\mathrm{sec}$.

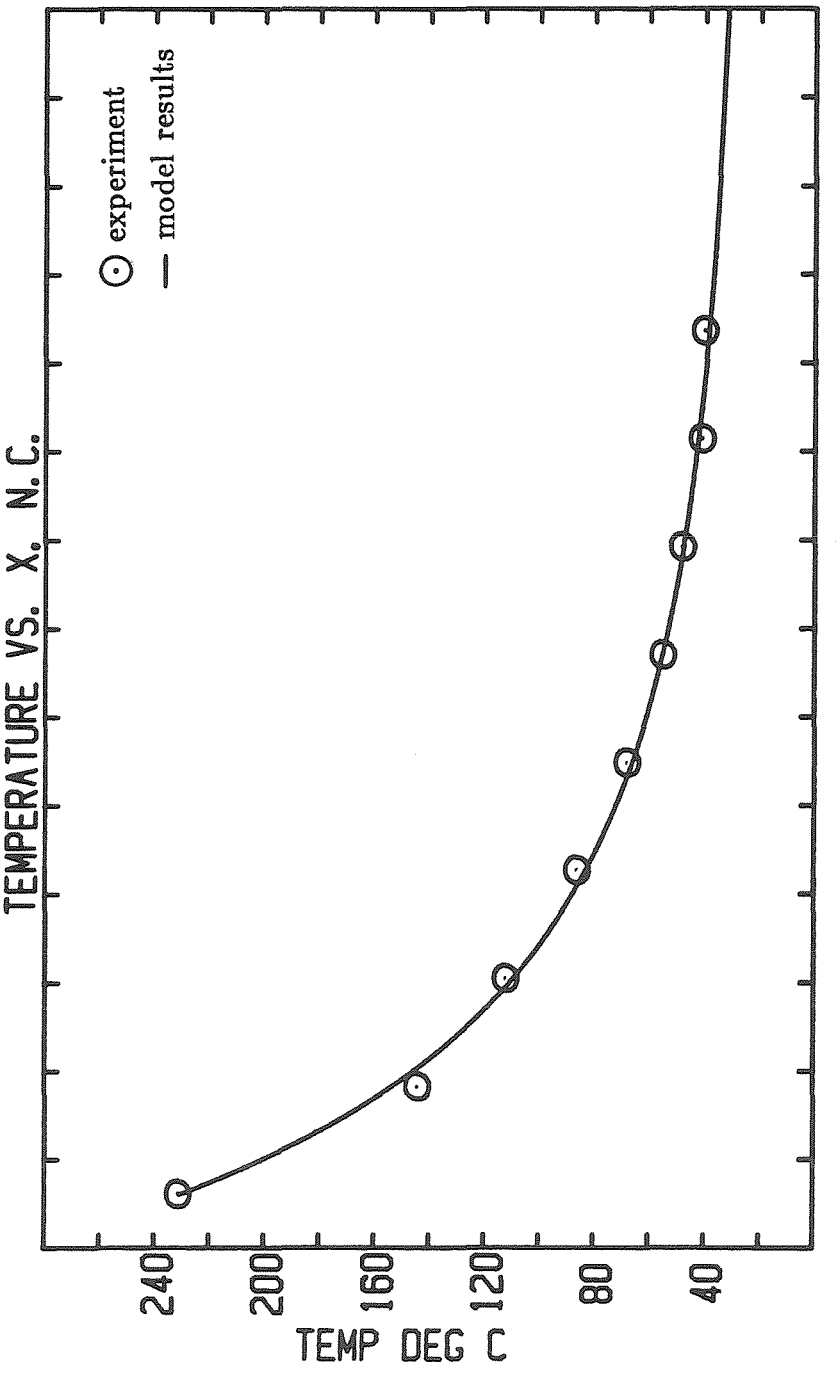

Figure 4.8 Comparison of critical solution using sidewall correction with measurements, T(° C) versus x(m), for nominal case thermal flow.

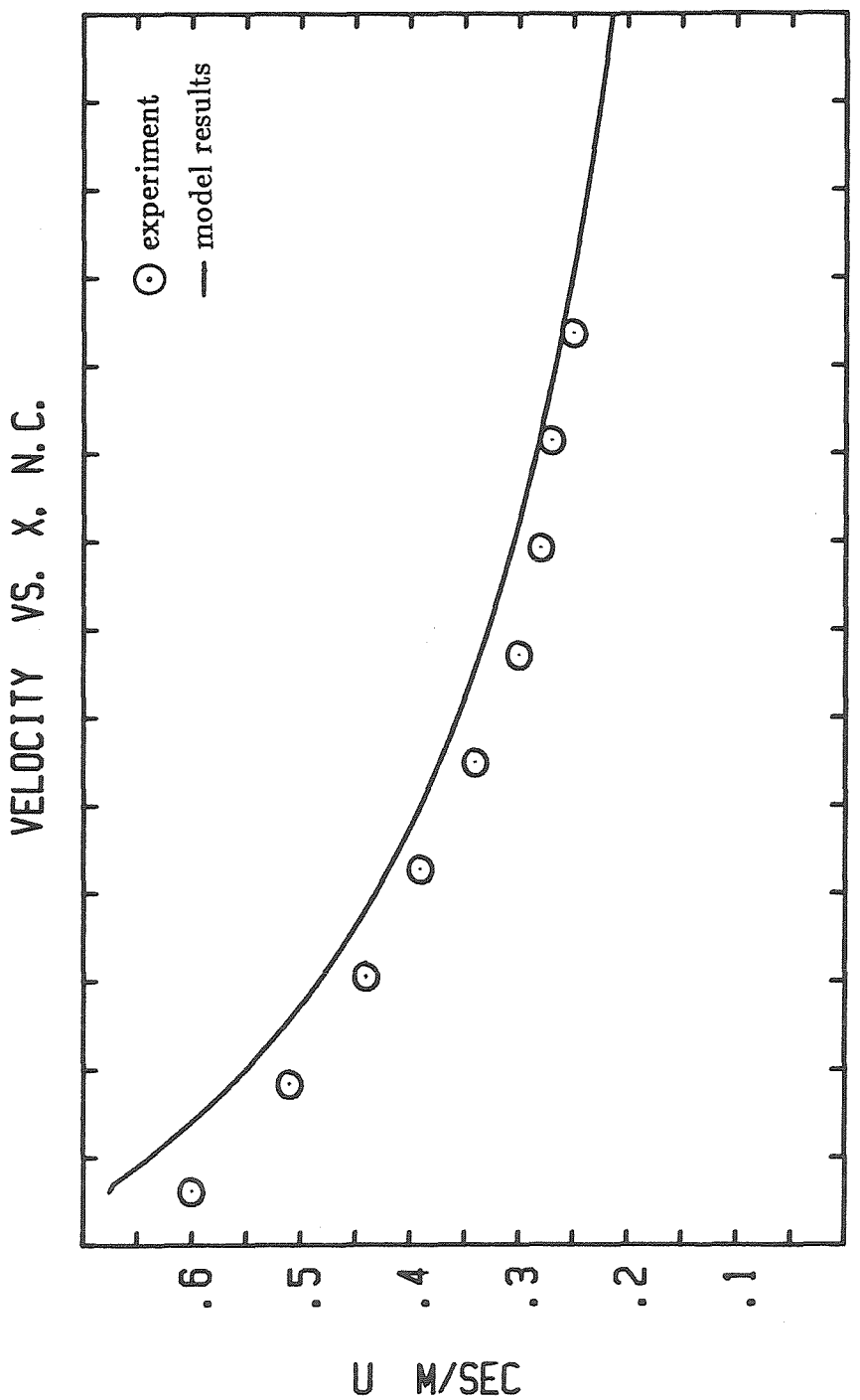

Figure 4.9 Comparison of critical solution using sidewall correction with measurements, u(m/sec) versus x(m), for nominal case thermal flow.

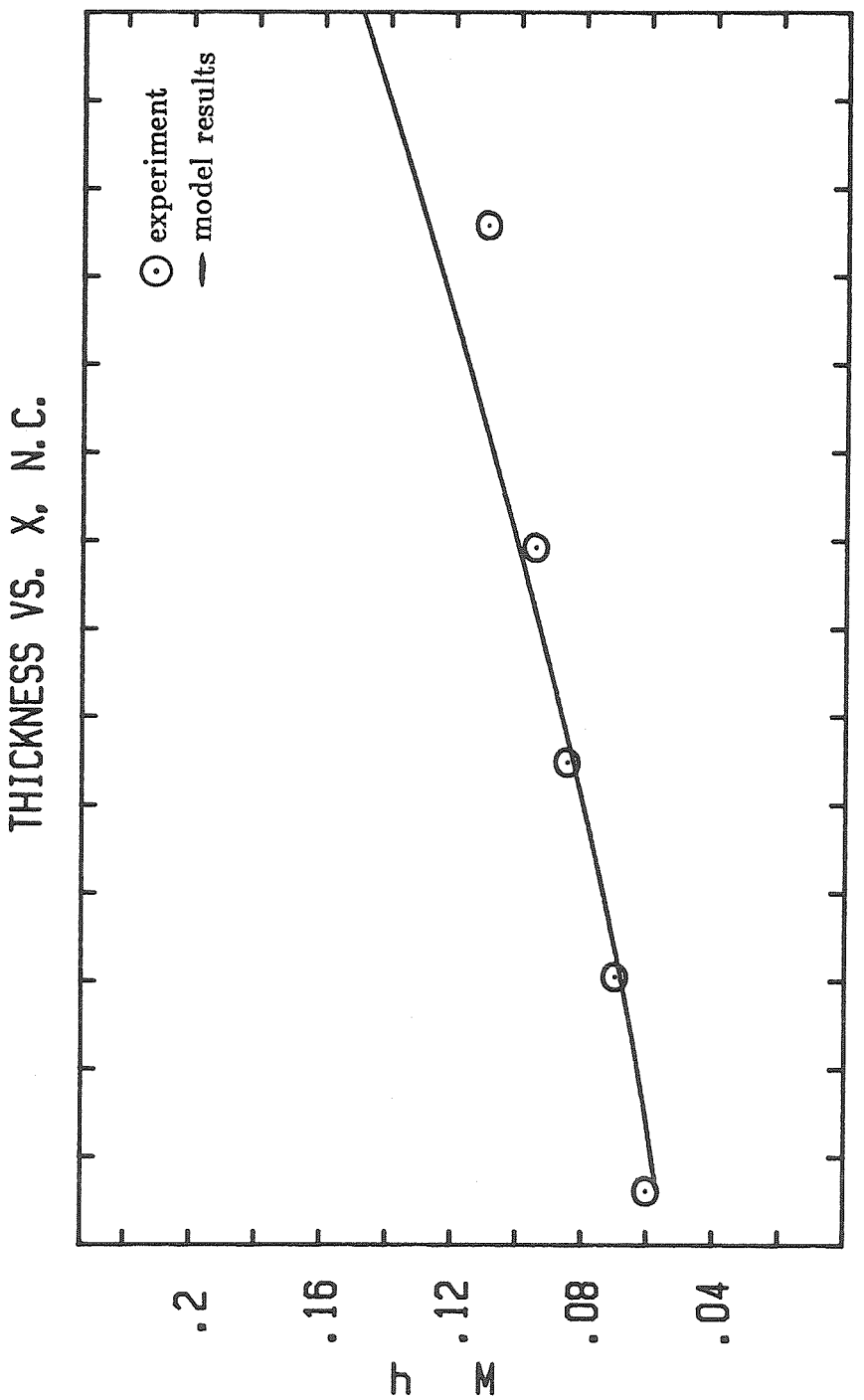

Figure 4.10 Comparison of critical solution using sidewall correction with measurements, h(m) versus x(m), for nominal case thermal flow.

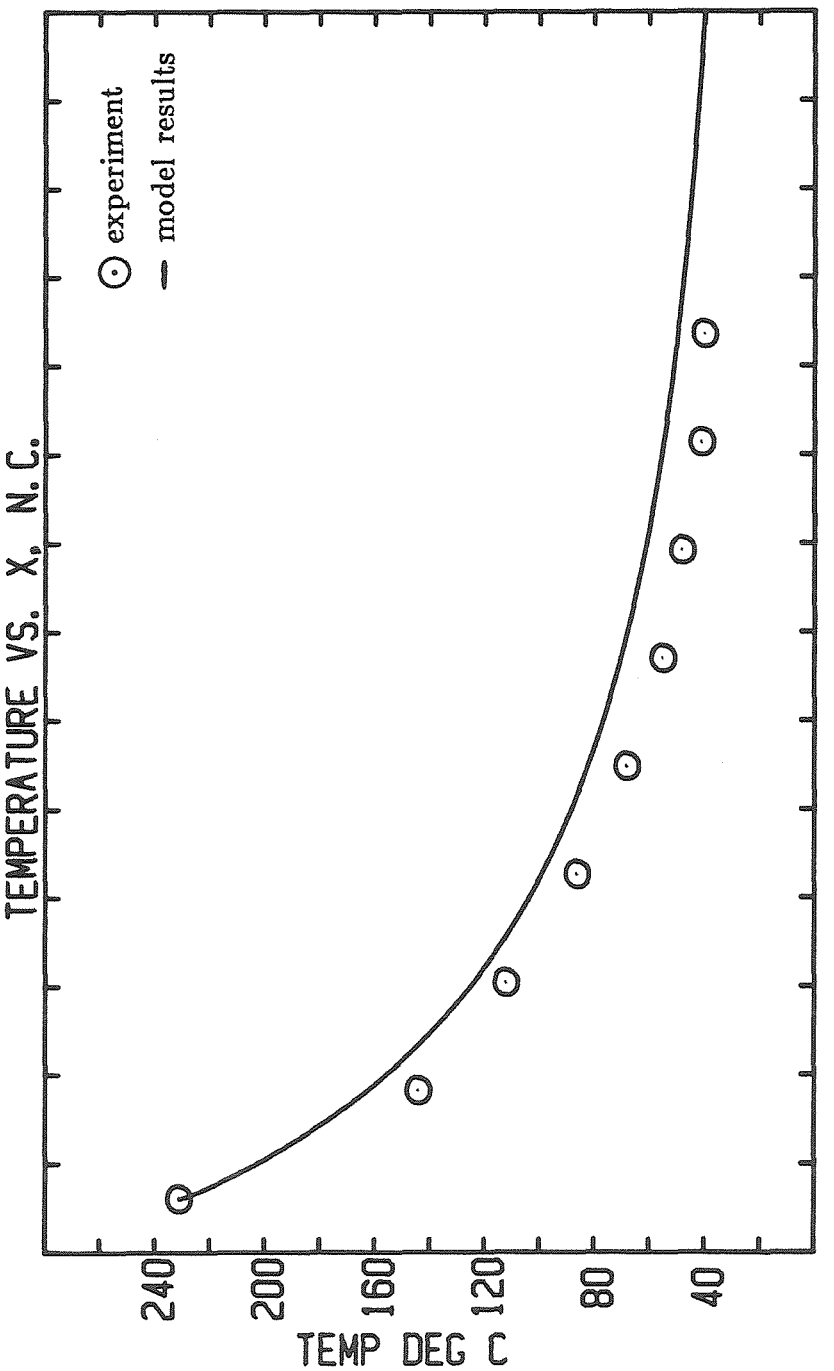

Figure 4.11 Comparison of critical solution using wall shear stress velocity perturbation, $T(^\circ\mathrm{C})$ versus $x(\mathrm{m})$, for nominal case thermal flow.

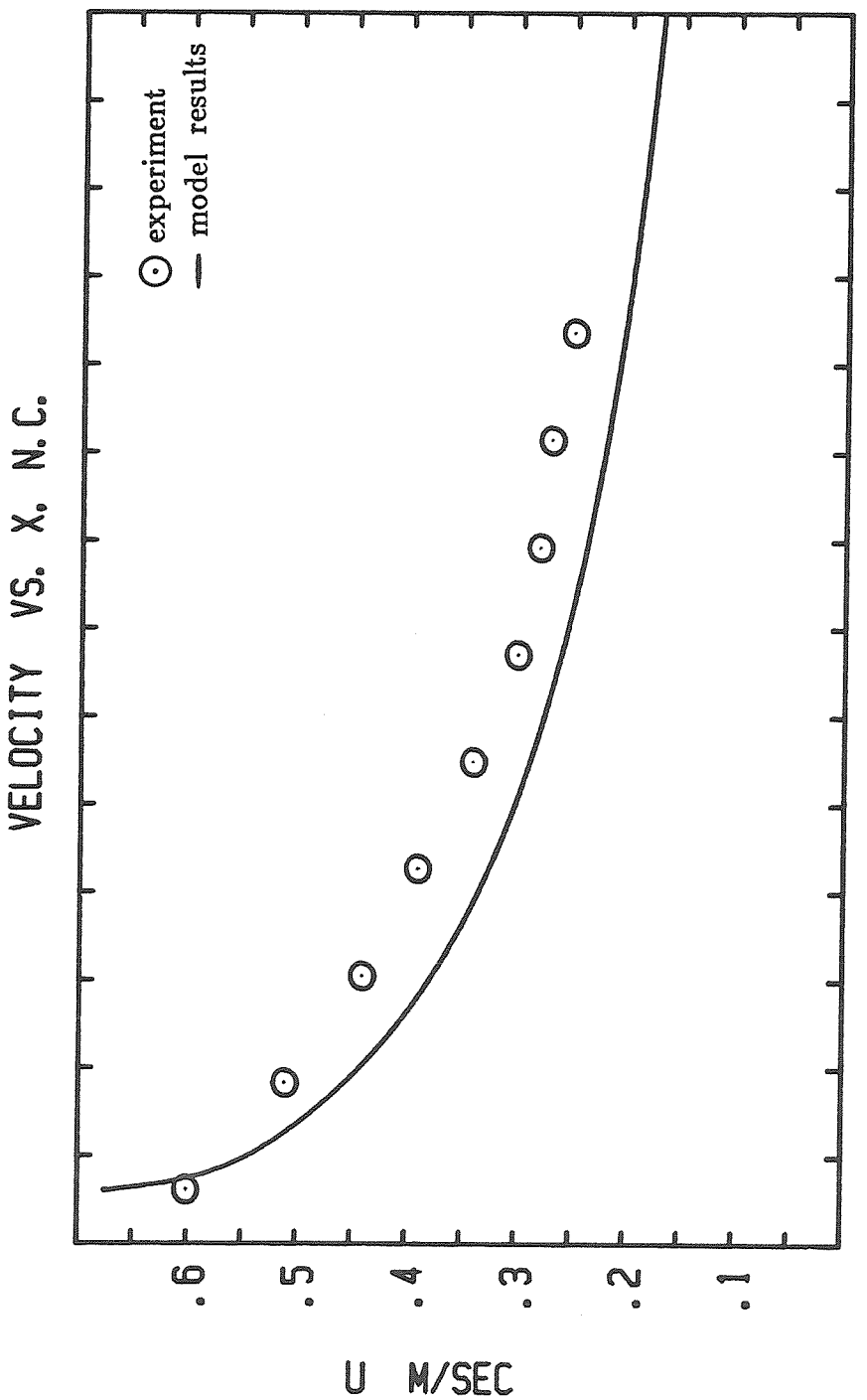

Figure 4.12 Comparison of critical solution using wall shear stress velocity perturbation, u(m/sec) versus x(m), for nominal case thermal flow.

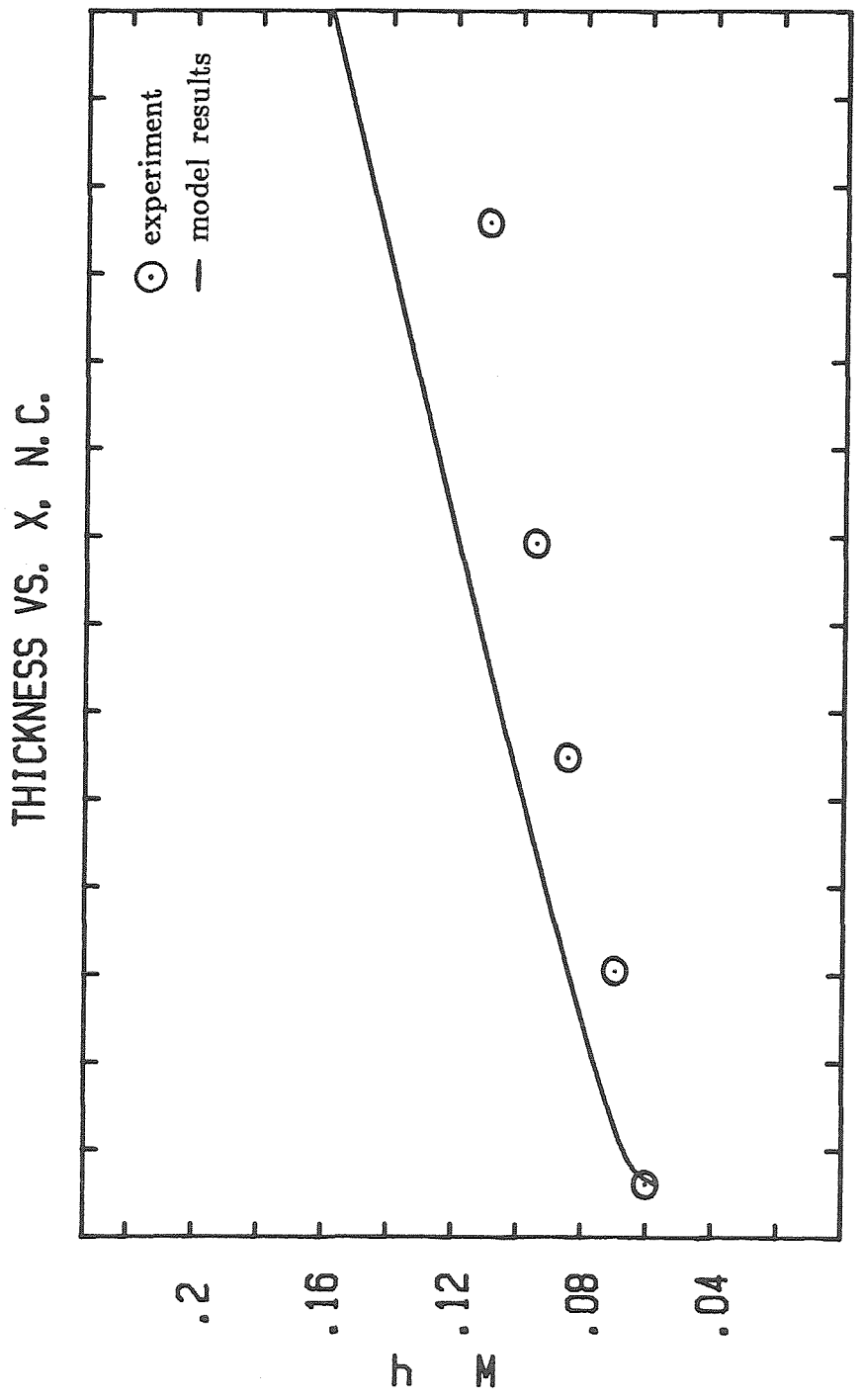

Figure 4.13 Comparison of critical solution using wall shear stress velocity perturbation, h(m) versus x(m), for nominal case thermal flow.

Chapter 5

Summary and Conclusion

An experimental study of the flow field characteristics of two-dimensional gravity currents, of both the adiabatic and heat transferring types, flowing in a horizontal duct is performed. Both qualitative and quantitative characteristics of adiabatic currents are examined through the use of dyed saline solution as the gravity current fluid propagating through ambient fresh water. Video photography is used as the principal data gathering technique. The relative importances of viscous and inertial forces compared with buoyancy driving forces of the flows are studied and are summarized here. In addition, the main qualitative characteristics of both types of gravity current flows are highlighted.

The thermal gravity current flows are generated using heated gas as the current fluid, introduced at a constant volumetric flow rate into a duct containing ambient temperature air. Quantitative measurements are made with the use of thermocouples, heat flux gauges, and a smoke wire technique developed for this application. The effect of heat transfer on these transient thermal flows along the constant temperature duct ceiling is examined, and the major results and conclusions are presented here. Results of the modeling of this thermal flow based on experimental observations are also reviewed.

Adiabatic Gravity Currents:

Two-dimensional adiabatic gravity currents propagating in a horizontal duct were observed to move with a constant current front velocity, until viscous shear forces became significant and slowed the front spreading rate so that the

frontal downstream position increased with time roughly proportional to $t^{.8}$. This inertial-viscous transition was observed to occur at downstream positions of about 100 times the current layer thickness. The spreading rate constant, C, exhibited an Re dependence, increasing to an asymptotic value near 1.1 for high Re. Ambient fluid effects were observed to be small when the layer thickness-to-channel height ratio, h/d, was low (of order .1). The qualitative features of the current head demonstrated dependence on Reynolds number based on head thickness. The general understanding of gravity current entrainment is believed to include a Reynolds number dependent entrained ambient fluid flow into the head at its foremost turbulent region. For the case in which viscous effects became important, the layer thickness of the current was observed to grow in accordance with laminar viscous boundary layer theory.

Heat Transferring Gravity Currents:

Convective heat transfer to the ceiling of the duct by the thermal currents greatly affected the current flows. The local heat transfer coefficient, h, depended only on the local fluid velocity and fluid properties. This coefficient was seen to be some ten times higher than the value estimated for a laminar wall jet with the same Reynolds number, and three to five times greater than the value for the corresponding turbulent wall jet. This heat transfer, expressed in the form of Nusselt number based on the same length scale in the manner:

$$Nu_x = .013\, Re_x\,.$$

Runs representing a wide range of Rayleigh numbers produced results in agreement with this relation. The value of Ra was observed to vary little along the streamwise direction in the thermal flows. This large heat transfer rate resulted from natural convection within the boundary layer of the thermal current which

developed between the cool boundary layer flow adjacent to the wall and the hotter flow below it. This convection appeared in the form of large two-dimensional rolls with their axes parallel to the direction of flow and to the wall, in effect, two-dimensional Bénard cells. These rolls also significantly affected the velocity profiles in the thermal current, reducing the size of the wall boundary layer, and hence increasing the velocity gradient at the wall. The loss of buoyancy due to heat transfer decelerated the flow as it spread downstream, and increased its layer thickness. In spite of this, the significance of buoyant forces compared to inertial forces in the layer was maintained, since the value of the Richardson number did not vary with downstream position ($Ri \approx 1$ for all cases examined). The time dependence of local mean quantities was seen to be weak, and a quasi-steady approximation of the flow field resulted in a model based on experimental observations that reproduced the current behavior well. The observed self similarity of the temperature and velocity profiles was also incorporated into the integral modeling scheme.

Although these experiments studied heat transfer to a wall of essentially constant temperature, non-isothermal wall flows may be of interest. The high levels of heat transfer measured would produce wall surface temperature rises in the range of 20° C to 50° C after a period of 10 to 15 seconds for a ceiling composed of a material with much lower thermal conductivity and heat capacity than that used, such as plasterboard. Thus, for times greater than the time required for the current to reach the end of the test section used, the ceiling surface temperature rise could significantly affect the flow, an effect warranting future investigation.

Appendix A

Heat Flux Gauge Amplifier Schematic

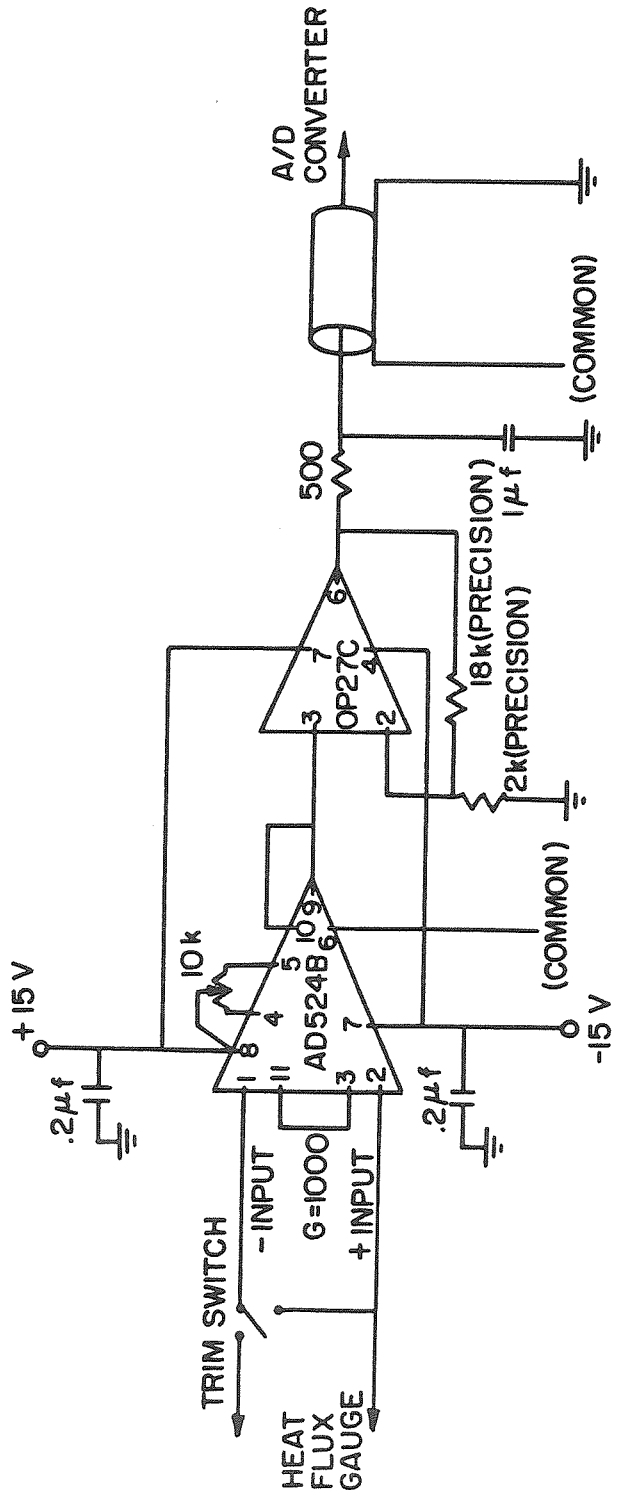

Appendix B

8085 Microprocessor System Details

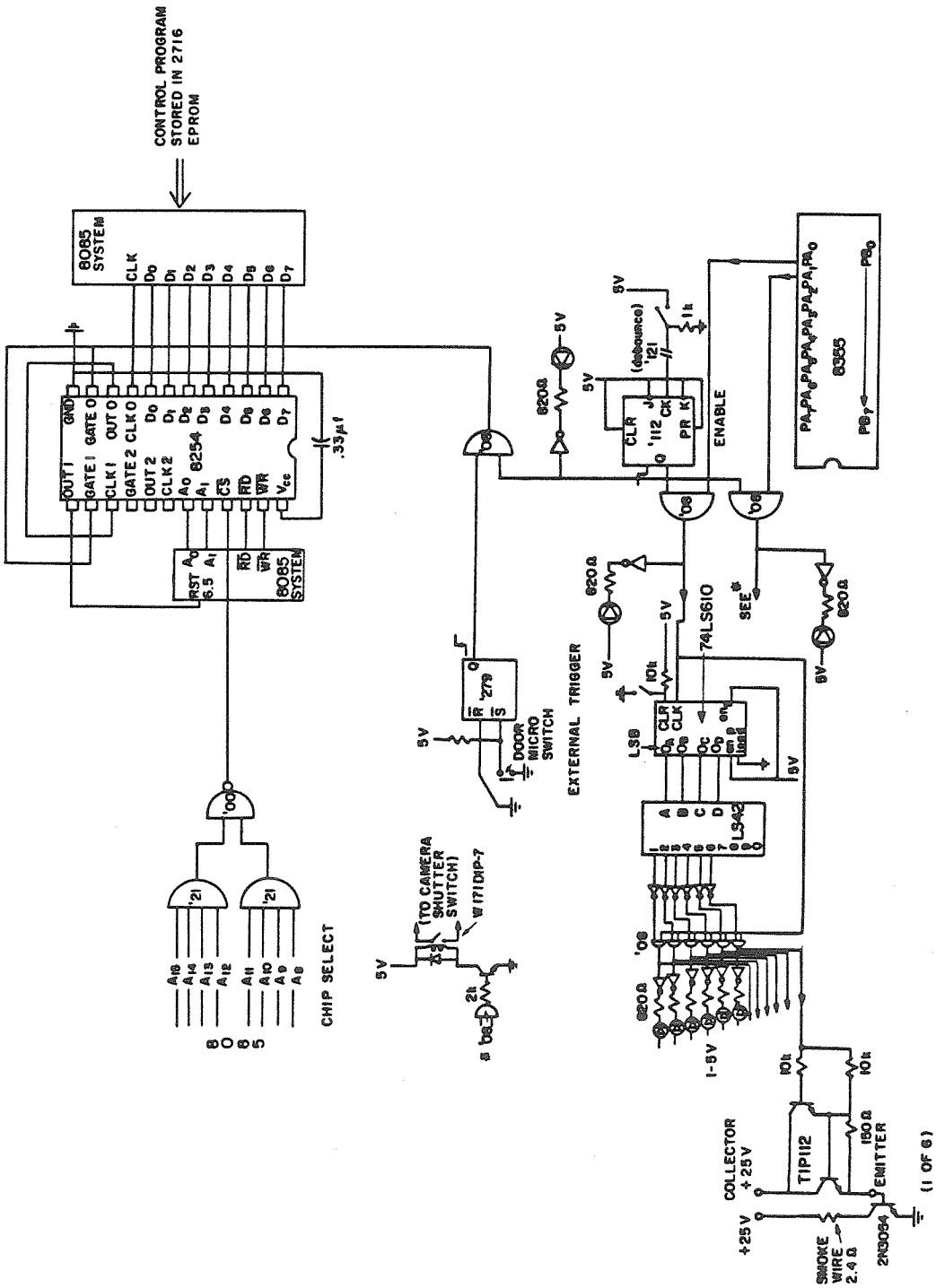

```
2000  31  LXI SP
   1  C2
   2  20
   3  21  LXI H
   4  03
   5  FF
   6  36  MVI M
   7  37
   8  36  MVI M
   9  71
   A  2B  DCX H
   B  2B  DCX H
   C  36  MVI M
   D  99
   E  36  MVI M
   F  99
2010  2B  DCX H
   1  36  MVI M
   2  36
   3  36  MVI M
   4  15
   5  3E  MVI A
   6  FF
   7  D3  OUT
   8  02
   9  3E  MVI A
   A  00
   B  D3  OUT
   C  00
   D  3E  MVI A
   E  OD  (interrupt mask)
   F  30  SIM
2020  FB  EI
   1  76  HALT
   2
   3
   4  06  MVI B
   5  00
2026  3E  MVI A
   7  01
   8  D3  OUT
   9  00
   A  11  LXI D
   B  00  (smoke pulse duration,
   C  08  0008 hex)
   D  CD  CALL
   E  60
   F  20
2030  3E  MVI A
   1  00
   2  D3  OUT
   3  00
   4  11  LXI D
   5  FF  (smoke convection
   6  FF  time, FFFF hex)
   7  CD  CALL
   8  60
   9  20
   A  3E  MVI A
   B  02
   C  D3  OUT
   D  00
   E  11  LXI D
   F  FF  (strobe pulse
2040  FF  duration, FFFF hex)
   1  CD  CALL
   2  60
   3  20
   4  3E  MVI A
   5  00
   6  D3  OUT
   7  00
   8  11  LXI D
   9  FF  (time between sets
   A  FF  of pulses, FFFF hex)
   B  CD  CALL
204C  60
   D  20
   E  04  INR B
   F  78  MOV A,B
2050  FE  CPI
   1  06  (6 CYCLES)
   2  C2  JNZ
   3  26
   4  20
   5  CF  RST 1
   6
   7
   8
   9
   A
   B
   C
   D
   E
   F
2060  1B  DCX D
   1  7A  MOV A,D
   2  B3  OR A,E
   3  FE  CPI
   4  00
   5  C2  JNZ
   6  60
   7  20
   8  C9  RET
```

Appendix C

Calculation of δ_i from h

The following analysis refers to figure C.1, which represents a velocity profile, $u = u(y)$, at a given value x in the thermal gravity current layer modelled in chapter 4. The point denoted by y_{inf} is the y coordinate of the inflection point of the profile, and u_{inf} is its u value. The intersection of the tangent line through this inflection point with the y axis defines the minimum slope intercept, h. The relationship between these values can be written:

$$h = y_{inf} - \frac{u_{inf}}{\left(\frac{\partial u}{\partial y}\right)_{inf}}, \qquad (C.1)$$

and also,

$$\frac{\partial^2 u}{\partial y^2} = 0 \quad \text{at} \quad y = 0. \qquad (C.2)$$

Under the Howarth transformation,

$$y_i = \int_0^y \frac{\rho}{\rho_o} dy, \qquad (C.3)$$

we can write equation C.2 as:

$$\frac{\partial}{\partial y_i}\left(\frac{\rho}{\rho_o}\frac{\partial u}{\partial y_i}\right) = 0,$$

or,

$$\frac{\partial^2 u}{\partial y_i^2} + \frac{1}{\rho}\frac{\partial \rho}{\partial y_i}\frac{\partial u}{\partial y_i} = 0. \qquad (C.4)$$

Since pressure is essentially constant, the equation of state (equation 4.1.5) gives:

$$\frac{1}{\rho}\frac{\partial \rho}{\partial y_i} = -\frac{1}{T}\frac{\partial T}{\partial y_i}, \qquad (C.5)$$

which together with equation C.4 gives:

$$T\frac{\partial^2 u}{\partial y_i^2} - \frac{\partial T}{\partial y_i}\frac{\partial u}{\partial y_i} = 0\,. \qquad (C.6)$$

From the profile assumptions in the transformed coordinate system,

$$U = \frac{u}{u_m} = a\eta(1-\eta)^4\,, \qquad (C.7)$$

$$\Theta = \frac{T - T_o}{T_m - T_o} = a\eta(1-\eta)^4\,, \qquad (C.8)$$

$$\eta = \frac{y_i}{\delta_i}\,,$$

we can compute the terms in equation C.6,

$$\frac{\partial u}{\partial y_i} = \frac{u_m}{\delta_i}a(1-5\eta)(1-\eta)^3\,,$$

$$\frac{\partial^2 u}{\partial y_i^2} = -\frac{u_m}{\delta_i^2}a(8-20\eta)(1-\eta)^2\,,$$

$$\frac{\partial T}{\partial y_i} = \frac{T_m - T_o}{\delta_i}a(1-5\eta)(1-\eta)^3\,.$$

Equation C.6 then simplifies to:

$$4(2-5\eta) + \frac{T_m - T_o}{T_o}a(1-\eta)^4\left(1-2\eta+5\eta^2\right) = 0\,, \qquad (C.9)$$

which determines the value of η corresponding to y_{inf}, and this value will be referred to as η_{inf}.

We will now calculate the individual terms in the righthand side of equation C.1. Using the transformation of equation C.3, the value of the slope of the curve in figure C.1 at the inflection point can be written:

$$\left(\frac{\partial u}{\partial y}\right)_{inf} = \left(\frac{\rho}{\rho_o}\frac{\partial u}{\partial y_i}\right)_{inf}$$

$$= \frac{u_m}{\delta_i}a\left[\frac{(1-5\eta)(1-\eta)^3}{1+\frac{T_m-T_o}{T_o}a\eta(1-\eta)^4}\right]_{\eta=\eta_{inf}}\,, \qquad (C.10)$$

and the value of y_{inf} as:

$$y_{inf} = \delta_i \int_0^{\eta_{inf}} \left[1 + \frac{T_m - T_o}{T_o} a\eta(1-\eta)^4\right] d\eta$$

$$= \delta_i \left[\eta + \frac{T_m - T_o}{T_o} a \left(\frac{1}{2} - \frac{4}{3}\eta + \frac{3}{2}\eta^2 - \frac{4}{5}\eta^3 + \frac{1}{6}\eta^4\right)\eta^2\right]_{\eta=\eta_{inf}} \quad (C.11)$$

Using equation C.7, the value of u_{inf} can be written as:

$$u_{inf} = u_m a \left[\eta(1-\eta)^4\right]_{\eta=\eta_{inf}} . \quad (C.12)$$

Finally, the last term in equation C.1 can be expressed in the form:

$$\frac{u_{inf}}{\left(\frac{\partial u}{\partial y}\right)_{inf}} = \delta_i \left[\frac{\eta(1-\eta)}{(1-5\eta)}\left(1 + \frac{T_m - T_o}{T_o} a\eta(1-\eta)^4\right)\right]_{\eta=\eta_{inf}} . \quad (C.13)$$

Thus, the relationship between δ_i and h can be determined as follows:

- Determine the value of η_{inf} from equation C.9.
- Calculate y_{inf} and $\left(\frac{u}{\frac{\partial u}{\partial y}}\right)_{inf}$ from equations C.11 and C.13.
- Then calculate $h = y_{inf} - \left(\frac{u}{\frac{\partial u}{\partial y}}\right)_{inf}$, which gives h in terms of δ_i.

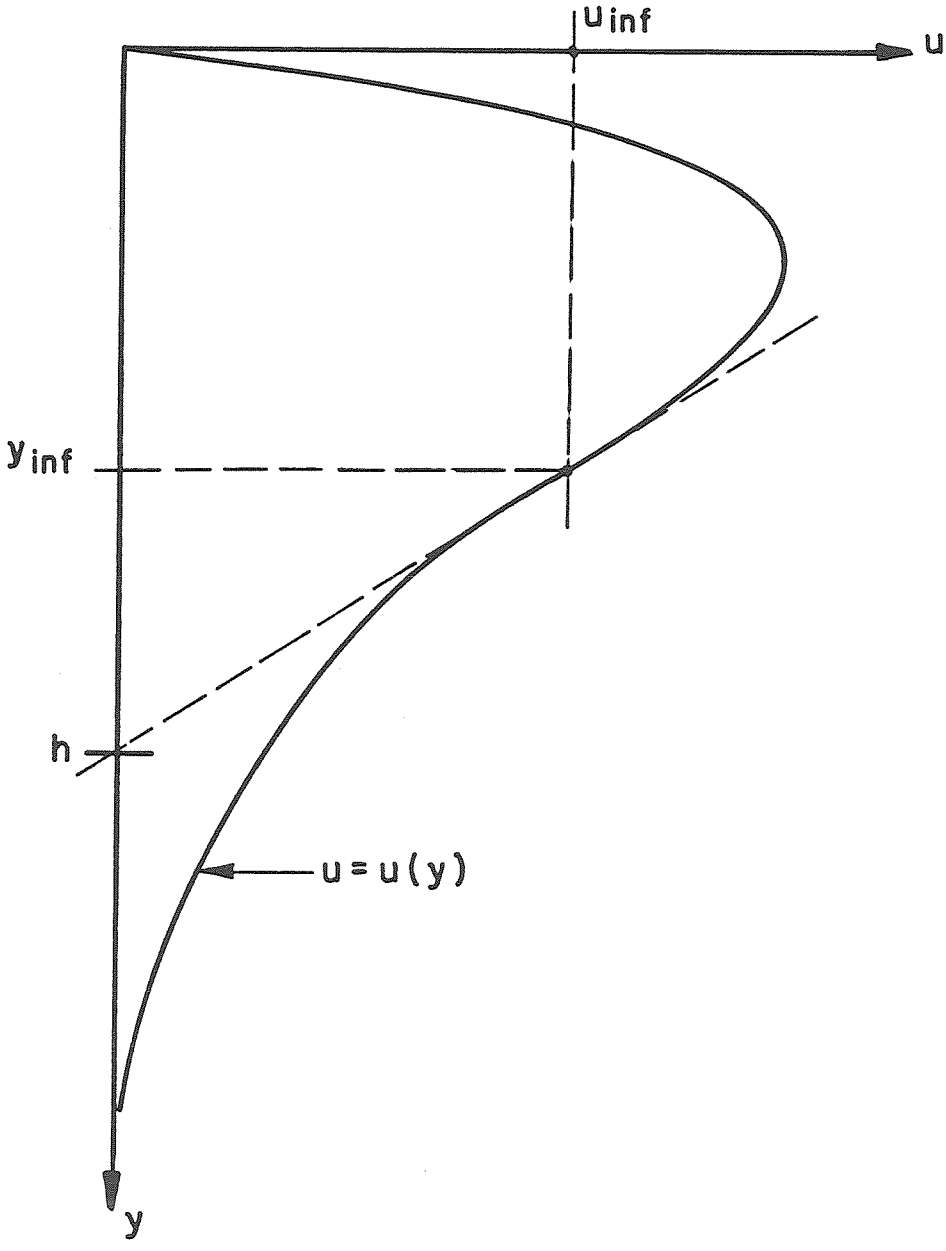

Figure C.1 Velocity profile nomenclature.

Appendix D

Model Computer Programs

```
$DEBUG
      PROGRAM EMBO
C     PROGRAM RUNS RUNGE-KUTTA SCHEME ON STEADY LAYER EQUATIONS
      REAL*8 Y(5),F(5)
      REAL*8 X,DEL,RHO,R,HI,TF,B,C1,EI,AI,BI,DI,GI,P1,P2,P3,WN,WD
     1 ,H,XLIM
      OPEN(13,FILE=' ',STATUS='NEW')
    3 FORMAT(5X,'X',14X,'T',14X,'U',13X,'RHO',14X,'DEL')
    4 FORMAT(3F10.0,2I5/(8F10.0))
    5 FORMAT(1X,5(F12.4,2X))
  100 WRITE (*,*)'INPUT STARTING X [M]'
      READ  (*,*,ERR=100) X
      XLIM=7.0
  122 WRITE (*,*)'INPUT STEP SIZE [M]'
      READ  (*,*,ERR=122) H
      M=0
      N=1
  101 WRITE (*,*)'INPUT INITIAL T MAX [DEG K]'
      READ  (*,*,ERR=101) Y(1)
  102 WRITE (*,*)'INPUT INLET MASS FLUX [KG/SEC]'
      READ  (*,*,ERR=102) C1
      R=(Y(1)-297.)/297.
      Y(2)=(33.*1800.*9.8*C1*R/(105.*12.207*12.207*1.17)+
     1  33.*9.8*C1*R*R/(12.207*1.17))**.3333333
      DEL=4.*(1.5+R)*30.*C1/(1.17*Y(2)*.5*12.207*9.)
      RHO=1.17*297./Y(1)
      WRITE (13,3)
      WRITE (13,5) X,Y(1),Y(2),RHO,DEL
      WRITE (*,3)
      WRITE (*,5) X,Y(1),Y(2),RHO,DEL
C     PROGRAM USES INTEGRAL METHOD OF PROFILE A(Y/D)(1-(Y/D))**4
C     WHERE A=12.207 AND D IS DEL(I)
C     FOR BOTH THE VELOCITY AND TEMPERATURE DIFFERENCE,VISCOUS
      B=0.5
      W=0.5
      EI=1300.*495.*297./(30.*C1*12.207*1010.)
    8 IF(X-XLIM)6,6,7
    6 CALL RUNGE (N,Y,F,X,H,M,K)
      GO TO (10,20),K
   10 R=(Y(1)-297.)/297.
      TF=(Y(1)+297.)/2.
      F(1)=-EI*R*Y(2)*W/(TF)**.73
      GO TO 6
```

```
   20 Y(2)=(33.*1800.*9.8*C1*R/(105.*12.207*12.207*1.17)+
     1  33.*9.8*C1*R*R/(12.207*1.17))**.3333333
      RHO=347.5/Y(1)
      DEL=30.*C1/(12.207*B*1.17*Y(2))
      DEL=(2./3.)*(1.5+R)*DEL/1.5
      WRITE (13,5) X,Y(1),Y(2),RHO,DEL
      WRITE (*,5) X,Y(1),Y(2),RHO,DEL
      GO TO 8
    7 STOP
      END



      SUBROUTINE RUNGE (N,Y,F,X,H,M,K)
C     THIS ROUTINE PERFORMS RUNGE-KUTTA CALCULATIONS
C     BY GILLS METHOD
      REAL*8 Y(5), F(5), Q(10)
      REAL*8 A,X,H
      M=M+1
      GO TO (1,4,5,3,7),M
    1 DO 2 I=1,N
    2 Q(I)=0
      A=.5
      GO TO 9
    3 A=1.7071067811865475244
    4 X=X+.5*H
    5 DO 6 I=1,N
      Y(I)=Y(I)+A*(F(I)*H-Q(I))
    6 Q(I)=2.*A*H*F(I)+(1.-3.*A)*Q(I)
      A=.29289321881345247 56
      GO TO 9
    7 DO 8 I=1,N
    8 Y(I)=Y(I)+H*F(I)/6.-Q(I)/3.
      M=0
      K=2
      GO TO 10
    9 K=1
   10 RETURN
      END
```

6. References

Almquist, C. (1973), "The Two-Dimensional Surface Spreading of a Buoyant Fluid into an Infinite Stagnation Environment," *Unpublished paper for ENV 112 course at the California Institute of Technology.*

Benjamin, T.B. (1968), "Gravity Currents and Related Phenomena," *J. Fluid Mech.*, **31**, 209-248.

Braucher, E.P. (1950), "Initial Characteristics of Density Current Flow," *S.M. Thesis, Massachusetts Institute of Technology.*

Cetegen, B.M., Zukoski, E.E., and Kubota, T. (1982), "Entrainment and Flame Geometry of Fire Plumes," *California Institute of Technology report.*

Chen, J.C. (1980), "Studies on Gravitational Spreading Currents," *Ph.D. thesis, California Institute of Technology.*

Davis, E.J. and Choi, C.K. (1977), "Cellular Convection with Liquid Film Flow," *J. Fluid Mech.*, **81**, 564-592.

Eckert, E.R.G. and Drake, R.M., (1972), Analysis of Heat and Mass Transfer, McGraw-Hill, New York.

Ellison, T.H. and Turner, J.S. (1959), "Turbulent Entrainment in Stratified Flows," *J. Fluid Mech.*, **6**, 423-447.

Georgeson, E.M.H. (1942), "The Free Streaming of Gases in Sloping Galleries," *Proceedings of the Royal Society of London, Series A*, **180**, 484-493.

Imberger, J. (1986), *Private communication.*

Ippen, A.T. and Harleman, D.R.F. (1952), "Steady-State Characteristics of Subsurface Flow," *Proceedings of the NBS Symposium on Gravity Waves, National Bureau of Standards Circ.*, **521**, 79-93.

Kármán, T. von (1940), "The Engineer Grapples with Nonlinear Problems," *Bulletin of the American Mathematical Society*, **46**, 615.

Keulegan, G.H. (1952), "Second Progress Report on Model Laws for Density Currents for Chief of Engineers, U.S. Army," August 6.

Keulegan, G.H. (1958), "The Motion of Saline Fronts in Still Water," *National Bureau of Standards report 5831.*

Koh, R.C.Y. (1971), "Two-Dimensional Surface Warm Jets," *J. Hydraul. Div. ASCE*, **97** (HY6), 819-836.

Kubota, T. (1986), *Private communication.*

Liepmann, H.W. and Roshko, A. (1957), Elements of Gasdynamics, Wiley, New York.

Luketina, D.A. and Imberger, J. (1986), "The Mean Dynamics of a Surface Buoyant Jet," *J. Geophysical Research*, to be published.

Schlichting, H. (1968), Boundary Layer Theory, McGraw-Hill, New York.

Schmidt, W. (1911), "Zur Mechanik der Böen," *Z. Meteorol.*, **28**, 355-362.

Schwarz, W.H. and Cosart, W.P. (1960), "Two-Dimensional Turbulent Wall Jet," *J. Fluid Mech.*, **10**, 481-495.

Simpson, J.E. (1969), "A Comparison between Laboratory and Atmospheric Density Currents," *Quart. J. Res. Meteorol. Soc.*, **95**, 758-765.

Simpson, J.E. (1972), "Effects of the Lower Boundary on the Head of a Gravity Current," *J. Fluid Mech.*, **53**, 759-768.

Simpson, J.E. (1982), "Gravity Currents in the Laboratory, Atmosphere, and Ocean," *Ann. Rev. Fluid Mech.*, **14**, 213-234.

Simpson, J.E. and Britter, R.E. (1979), "The Dynamics of the Head of a Gravity Current Advancing over a Horizontal Surface," *J. Fluid Mech.*, **94**, 477-495.

Turner, J.S. (1973), Buoyancy Effects in Fluids, Cambridge University Press, Cambridge.

White, F.M. (1974), Viscous Fluid Flow, McGraw-Hill, New York.

Wilke, C.R. (1950), "A Viscosity Equation for Gas Mixtures," *J. Chemical Physics*, **18**, 517-519.

Wilkinson, D.L. (1970), "Studies in Density-Stratified Flows," Report no. 118, Water Resource Laboratory, The University of New South Wales, Manly Vale, N.S.W. Australia.

Wilkinson, D.L. (1982), "Motion of Air Cavities in Long Horizontal Tubes," *J. Fluid Mech.*, **118**, 109-122.

Winant, C.D. and Bratkovich, A. (1977), "Structure and Mixing Within the Frontal Region of a Density Current," 6th Aust. Hydraul. and Fluid Mech. Conf., Adelaide, Australia, Dec. 1977, 9-12.

Wood, I.R. (1967), "Horizontal Two-Dimensional Density Current," *J. Hydraul. Div. ASCE*, **92** (HY2), 35-42.

Young, P.M. (1984), "The Spreading of Plane Salt Water Gravity Currents," *S.U.R.F. report, California Institute of Technology.*

Zukoski, E.E. (1966), "Influence of Viscosity, Surface Tension, and Inclination Angle on Motion of Long Bubbles in Closed Tubes," *J. Fluid Mech.*, **25**, 821-837.

Zukoski, E.E. and Kubota, T. (1984), "Experimental Study of Environment and Heat Transfer in a Room Fire," *California Institute of Technology report.*